Università
Campus Bio-Medico di Roma

Department of Engineering
Ph.D. course in Bioengineering, Applied Science and Intelligent System

---

Computational and Experimental Advances in Laser-Based Thermal Ablation

Supervisors

Prof. Emiliano Schena

Prof. Alessio Gizzi

Candidate

Federica Bianconi

Academic Year 2024/2025

Contents

List of Figures

List of Tables

List of abbreviations

3D – Three-dimensional

AF – Atrial Fibrillation

AuNPs – Gold Nanoparticles

BC(s) – Boundary Condition(s)

CAD – Computer-Aided Design

CT – Computed Tomography

D – Denatured state

DPL – Dual Phase Lag

ECG – Electrocardiogram

EDX – Energy-Dispersive X-ray Spectroscopy

FBG(s) – Fiber Bragg Grating(s)

FDM – Fused Deposition Modeling

FEM – Finite Element Method

GF – Generalized Fourier

HIFU – High-Intensity Focused Ultrasound

IRE – Irreversible Electroporation

LA – Laser Ablation

LITT – Laser-Induced Interstitial Thermotherapy

LSPR – Localized Surface Plasmon Resonance

MRI – Magnetic Resonance Imaging

MWA – Microwave Ablation

N – Native state

NC(s) – Nanocage(s)

NIR – Near Infrared

NP(s) – Nanoparticle(s)

NR(s) – Nanorod(s)

NTA – Nanoparticle Tracking Analysis

ODA – Optical Diffusion Approximation

PCE – Photothermal Conversion Efficiency

PFA – Pulsed Field Ablation

PLA – Polylactic Acid

PTA(s) – Photothermal Agent(s)

PTT – Photothermal Therapies

RF – Radiofrequency

RFA – Radiofrequency Ablation

SAR – Specific Absorption Rate

SLA – Stereolithography

SLS – Selective Laser Sintering

TA – Thermal Ablation

TAT(s) – Thermal Ablation Treatment(s)

TEM – Transmission Electron Microscopy

TID – Thermal Isoeffective Dose

U – Unfolded state

UV – Ultraviolet

UV–Vis–NIR – Ultraviolet Visible Near Infrared

VT – Ventricular Tachycardia

Preface

Thermal ablation (TA) has become a central tool in modern minimally invasive medicine, offering effective alternatives to conventional surgical procedures for both oncological applications and cardiac arrhythmia management. Despite its clinical relevance, predicting and controlling the outcome of energy delivery within living tissue remains a significant scientific and technological challenge. Biological heterogeneity, nonlinear heat-transfer mechanisms, and the need for precise real-time monitoring motivate the development of integrated approaches that combine advanced computational modeling, quantitative sensing, and experimental validation.

This doctoral thesis was conceived and developed within this interdisciplinary context. The work brings together mathematical modeling of laser–tissue interactions, *in vitro* and *ex vivo* experimental investigations, and the use of nanotechnologies and optical fiber sensors to improve the accuracy, selectivity, and predictability of thermal ablation. Two complementary clinical scenarios guide the research: laser ablation for cardiac arrhythmia treatment, approached primarily through computational models, and nanoparticle-mediated and sensor-monitored laser ablation in liver tissue, addressed through extensive laboratory experimentation. Although distinct in their physiological and therapeutic objectives, these lines of inquiry are united by a common scientific ambition: enhancing control over thermal energy deposition in biological media.

The thesis reflects an iterative process in which computational simulations inform the design and interpretation of experiments, while experimental evidence, in turn, reveals critical aspects that refine and validate the models. This synergy has been essential for addressing questions related to heat propagation, tissue damage dynamics, photothermal enhancement, and the limitations of traditional sensing and modeling strategies. The research work opens with a comprehensive background on thermal ablation, presenting the underlying physical principles, the clinical motivations, and the variety of available energy-delivery techniques. This introductory framework establishes the context for the subsequent experimental investigations, which explore nanoparticle-mediated laser ablation and the use of fiber Bragg grating sensors to achieve high-resolution, real-time thermal monitoring in both *in vitro* and *ex vivo* environments. Building on the insights gained from these experiments, the thesis then transitions to the computational component, where advanced thermal models and optical–thermal coupling formulations are developed to describe heat propagation, tissue response, and lesion formation with greater accuracy and generality. The final chapters integrate the experimental and computational findings, offering a unified interpretation of the results and discussing the broader implications for precision thermal therapies. These concluding sections highlight open challenges, emerging opportunities, and promising

directions for future research, particularly within the framework of ongoing interdisciplinary projects aimed at advancing minimally invasive ablation technologies.

Background and Motivation

1

Ablation

Over the past two decades, the clinical community has progressively shifted from large-scale resections toward focal energy–based therapies that destroy unwanted tissue in situ. Thermal ablation treatments (TATs) achieve local cytotoxic temperatures and therefore avoid wide excisions, long hospital stays, and the morbidity that traditionally accompanied oncologic or cardiac surgery [1]. Contemporary literature consistently reports shorter recovery times, lower complication rates and cost containment when TATs are offered to otherwise inoperable patients or to those with significant comorbidities [1].

Conventional resection can be precluded by cardiopulmonary risk, multifocal disease or proximity to eloquent structures; it also carries infection, bleeding and cosmetic drawbacks [2]. Ablation overcomes these barriers by leveraging image guidance, local anaesthesia and percutaneous access, and it does not preclude future surgery, transplant or systemic therapy if required.

Ablation Techniques.
The spectrum of ablative modalities is broad, encompassing Radiofrequency (RFA), Microwave (MWA), Laser (LA), cryogenic, Ultrasound (HIFU), and more recently Pulsed-Field (PFA) ablation, each relying on distinct mechanisms of energy delivery and associated biological responses. These procedures are classified as minimally invasive therapies, as they are typically performed percutaneously or endovascularly under imaging guidance, thus avoiding the morbidity associated with open surgery. Their minimally invasive nature allows precise targeting of pathological tissue while preserving surrounding structures, resulting in shorter hospitalization, reduced postoperative pain, and faster recovery times [1]. While their therapeutic target is common, e.g. induction of irreversible cellular injury, the pathways through which this is achieved differ substantially, ranging from resistive heating to dielectric excitation, optical absorption, tissue freezing, or electroporation. Such heterogeneity translates into specific advantages and limitations for each modality, influencing lesion size, selectivity, safety profile, and applicability to different anatomical contexts. Collectively, these techniques represent a shift from open surgical resection to image-guided, technology-driven treatments that are repeatable, precise, and compatible with multimodal oncologic or electrophysiological strategies. Figure 1.1 classifies today's mainstream procedures into thermal and non-thermal energy technologies, hyperthermic and hypothermic branches [3, 4].

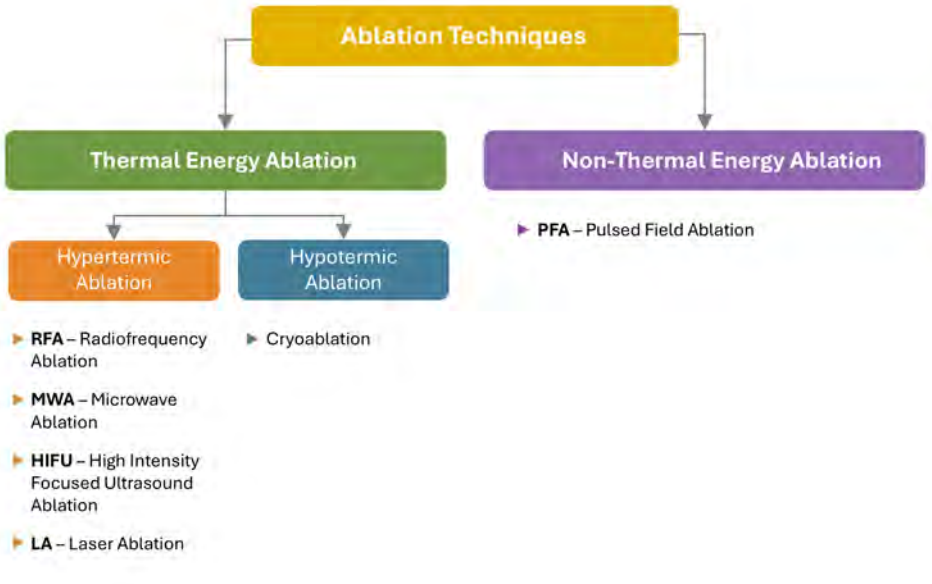

Figure 1.1: Schematic classification of ablation techniques. Thermal ablation methods are subdivided into hyperthermic approaches: RFA, MWA, LA, and HIFU, which induce tissue damage by heating tissues, and hypothermic approaches, represented by cryoablation, which exploit freezing-induced cell death. In parallel, the PFA, a non-thermal energy technique, achieves irreversible electroporation through high-voltage electrical pulses without significant thermal injury [3, 4].

Thermal ablation is a process that achieves tissue destruction through exposure to extreme temperatures, either by inducing hyperthermia (elevated tissue temperature) or hypothermia (deep cooling) [5]. Both thermal extremes are capable of causing cellular necrosis, although the underlying mechanisms differ between heating and freezing.

Human cells exhibit varying degrees of thermotolerance, and their susceptibility to thermal injury depends on the temperature reached, duration of exposure, and cumulative thermal dose experienced by each cell [5, 6]. Tissue damage produced by focal hyperthermia generally develops in two sequential stages. The first phase corresponds to direct heat-induced injury, primarily governed by the total amount of energy deposited within the tissue microenvironment [6]. The second phase involves indirect or delayed effects, where tissue destruction progresses over time due to microvascular impairment, ischemia–reperfusion phenomena, apoptosis activation, and inflammatory or immune-mediated responses, including Kupffer cell stimulation and cytokine modulation [6].

Figure 1.2 provides a summary of the relationship between temperature, exposure time, and resulting extent of cellular injury. As a general principle, complete cellular necrosis is achieved almost instantaneously when tissues are exposed to temperatures below $-40\,^{\circ}\mathrm{C}$ or above $60\,^{\circ}\mathrm{C}$, depending on the cell type and its intrinsic thermotolerance [5]. At temperatures lower than $-40\,^{\circ}\mathrm{C}$, cell death results primarily from direct freezing injury. Ice forms initially in the extracellular space, where water solidifies before intracellular freezing occurs, since the lipid

bilayer temporarily protects the cytoplasmic compartment [7]. This differential freezing creates a steep osmotic gradient, leading to water efflux, cellular dehydration, shrinkage, and membrane distortion. The process, known as solution-effect injury, is aggravated by intracellular ice crystal formation, which mechanically disrupts organelles and compromises membrane integrity. During the thawing phase, the rapid osmotic reversal causes cell swelling and rupture, completing the sequence of cryogenic injury [1]. In contrast, milder thermal exposures require longer durations to achieve irreversible damage. Temperatures maintained between 5 °C and 41 °C generally do not produce lasting therapeutic effects, as they are insufficient to trigger either coagulative necrosis or apoptosis [5].

Exposure to mild hyperthermia, with tissue temperatures up to 41 °C, induces vasodilation and increased blood perfusion, promoting heat dissipation and activating a cellular heat-shock response aimed at protecting proteins and repairing sublethal damage [8]. Such temperatures, even when sustained for several hours, generally have no lasting cytotoxic effect on viable tissue [5]. In the range of moderate hyperthermia (42 – 46 °C), irreversible cell injury can occur when exposure is prolonged, typically 30 ÷ 60 min, as sustained heating compromises membrane stability, enzyme function, and mitochondrial activity [1, 2, 8]. Shorter exposures ($\leq$ 60 min) may destroy a subset of cells, while surviving cells often develop thermotolerance, exhibiting increased resistance to subsequent heat stress [5]. When tissue temperature rises to 50 – 60 °C, the time required for lethal injury decreases markedly.

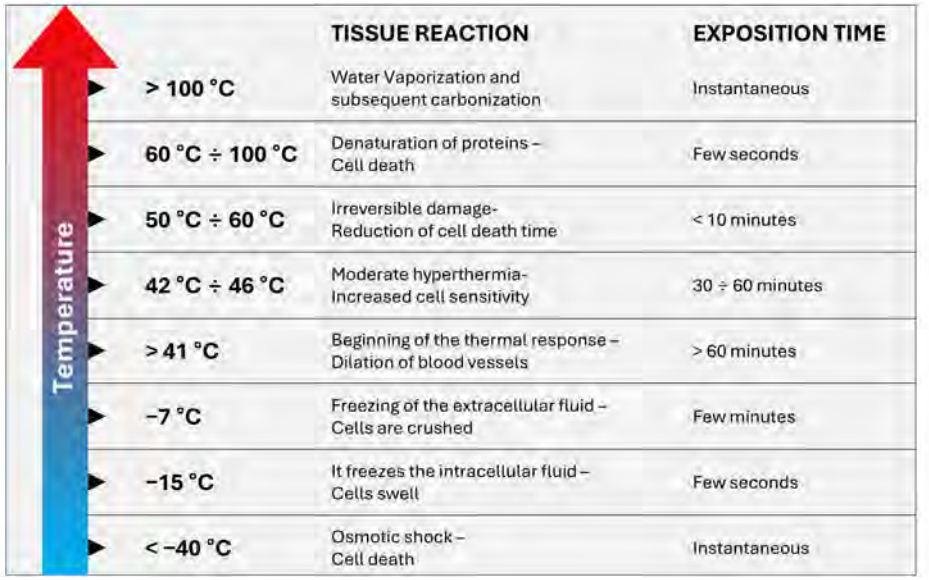

Figure 1.2: Summary of temperature-dependent biological effects in thermal ablation. The diagram illustrates the progressive sequence of tissue responses as temperature varies from extreme hypothermia to hyperthermia, highlighting the corresponding exposure times required to induce reversible or irreversible injury. Distinct thermal thresholds define transitions from cellular stress to coagulative necrosis and ultimately to vaporization and carbonization, delineating the operational temperature ranges relevant to different ablation modalities [5, 7, 8].

In this range, protein denaturation, coagulative necrosis, and microvascular thrombosis occur within minutes, leading to ischemia and hypoxia in the surrounding tissue. This cascade of vascular occlusion and nutrient deprivation perpetuates secondary, delayed necrosis beyond the directly heated region [5]. Temperatures in the range of $60 - 100\,^{\circ}\mathrm{C}$ produce coagulative necrosis within seconds, primarily due to rapid protein denaturation, enzymatic inactivation, and cell membrane disruption, which collectively lead to irreversible cell death [1, 8]. When the temperature exceeds $100\,^{\circ}\mathrm{C}$, water vaporization, gas formation, and tissue carbonization occur, creating an insulating layer that reduces the efficiency of heat transfer from the ablation device. The formation of charred tissue also causes a marked increase in local impedance, which in turn limits further current flow and heat generation in the surrounding tissue [1, 8, 9]. At even higher temperatures, significant alterations in the physical and electrical properties of tissue, including changes in conductivity, dielectric constant, and thermal diffusivity, further affect the propagation and delivery of energy during ablation procedures [5].

In light of the mechanisms underlying thermal injury in biological tissues, the following sections will provide a detailed overview of the main ablation techniques, emphasizing their physical principles, modes of energy delivery, and clinical applications. Regardless of the specific energy source employed, ablation refers to the use of a minimally invasive therapeutic approach designed to achieve controlled tissue destruction, increasingly adopted as a stand-alone treatment modality and, in some cases, as a viable alternative to conventional surgery.

1.1 Radiofrequency ablation

Radiofrequency ablation, introduced in the early 1990s [10], exploits high-frequency alternating current to induce controlled tissue destruction. It has emerged as the prototypical thermal ablation modality, primarily due to its relative simplicity, reproducibility, and cost-effectiveness [11]. Radiofrequency energy belongs to the electromagnetic spectrum and ranges from approximately 3 Hz to 300 GHz [11]. In the context of ablation, alternating current with frequencies between 300 and 500 kHz is most commonly employed [2, 11]. At these frequencies, energy delivery is sufficient to induce thermal agitation at the molecular level without eliciting neuromuscular stimulation or electrolysis. An RFA system typically consists of a generator, an active electrode (or probe), and grounding pad to complete the electrical circuit [12]. The active electrode is introduced into the target tissue, while dispersive pad, placed on the patient's skin, allow current return with minimal energy concentration [2, 11]. This design ensures that the heating effect remains localized to the tissue surrounding the electrode tip. The fundamental mechanism underlying RFA is resistive (ohmic) heating [2, 4, 13]. As alternating current passes through biological tissue, ions attempt to follow the rapid polarity changes, resulting in oscillatory motion. This ionic agitation generates frictional heat, which is concentrated in the immediate vicinity of the electrode. Heat then propagates centrifugally into surrounding tissue by thermal conduction. The extent of coagulative necrosis depends on the temperature reached and the duration of exposure [14]. Clinically, cooling mechanisms such as internally perfused electrodes have been developed to prevent charring and maintain efficient energy deposition [15]. RFA has been widely adopted for oncological applications, particularly for hepatic [16, 17], renal [18, 19], pulmonary [20], and osseous tumors [21], where it

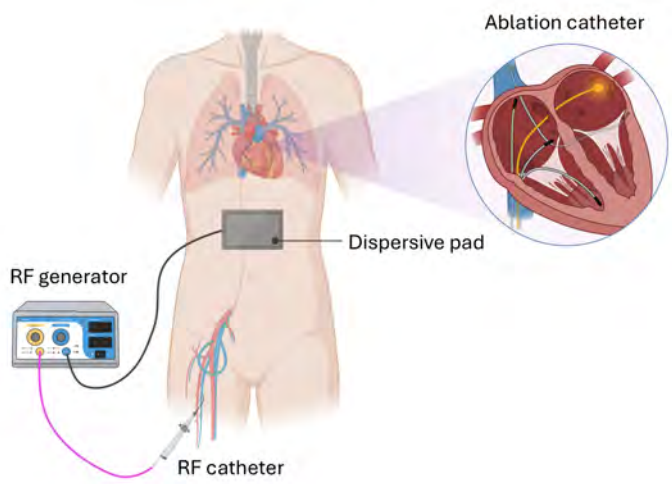

Figure 1.3: Schematic representation of cardiac RFA. A flexible ablation catheter is introduced, typically via the femoral vein, and advanced under fluoroscopic and electro-anatomical guidance to the endocardial surface. Radiofrequency current (300–500 kHz) delivered from the RF generator through the catheter tip induces resistive heating of myocardial tissue, producing localized coagulative necrosis and creating non-conductive lesions that interrupt arrhythmogenic circuits. A dispersive pad placed on the patient's skin completes the electrical circuit, ensuring current dispersion and procedural safety.

enables localized tumor destruction while sparing surrounding healthy tissue. The method produces well-demarcated zones of coagulative necrosis and has become an established alternative for patients who are not candidates for surgery due to comorbidities or tumor location. In hepatic applications, lesions up to 3 cm can typically be ablated with a single probe, while larger volumes require multi-tined electrodes or sequential overlapping ablations to ensure complete coverage [2].
Beyond oncology, RFA represents a cornerstone technique in cardiac electrophysiology, where it is used to eliminate arrhythmogenic foci responsible for disorders such as atrial fibrillation and ventricular tachycardia. In this context, radiofrequency energy delivered through catheter-based electrodes produces transmural thermal lesions that interrupt abnormal conduction pathways, restoring normal sinus rhythm. As illustrated in Figure 1.3, cardiac RFA is performed using a thin, flexible catheter, which is typically introduced through a femoral vein, under imaging and electro-anatomical guidance, into the heart chambers. Once positioned at the site of the arrhythmogenic focus or along the pathological conduction pathway, the catheter tip, equipped with a small electrode, delivers alternating current at 300–500 kHz directly to the myocardial tissue.

1.2 Microwave Ablation

Microwave ablation transmits electromagnetic energy at 915 MHz or 2.45 GHz through a coaxial antenna, which acts as a radiating element introduced percutaneously into the target tissue [2]. The basic MWA system consists of: MW generator, power distribution system and antennas, as shown in Figure 1.4.

The oscillating electromagnetic field induces dipolar rotation and ionic polar-

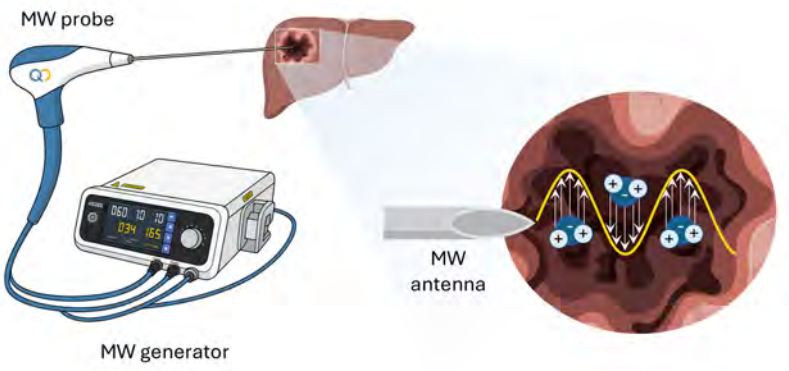

Figure 1.4: Schematic representation of the microwave ablation system. Electromagnetic energy generated by the MW generator is transmitted through a coaxial cable to the percutaneous antenna inserted into the target tissue. The oscillating microwave field (typically 915 MHz or 2.45 GHz) induces dipolar rotation of water molecules, generating rapid volumetric heating and coagulative necrosis within the target due to the dielectric hysteresis.

ization of water molecules, converting electromagnetic energy into heat through dielectric losses [2]. This mechanism produces a volumetric and homogeneous thermal field, rather than the localized resistive heating characteristic of RFA. As a result, MWA heating is independent of tissue impedance and remains effective even as tissues desiccate or carbonize, conditions that typically limit current flow in RFA [22]. Energy deposition in MWA is governed by the specific absorption rate (SAR), defined as the power absorbed per unit mass $\mathrm{W\,kg^{-1}}$, which depends on the local electric field intensity and on the dielectric properties of the medium. The frequency of operation determines the penetration depth and antenna geometry: lower frequencies (915 MHz) achieve deeper energy deposition with larger near fields, while higher frequencies (2.45 GHz) allow for more compact antennas and tighter control of the heating zone [23]. The rapid and continuous oscillation of polar molecules results in temperatures exceeding 100 °C within seconds, enabling the creation of coagulative necrosis volumes greater than 5 cm in diameter with a single insertion, depending on power and exposure time [22].

Because MWA systems operate in a monopolar radiative mode, they do not require a dispersive return electrode, thereby eliminating the risk of skin burns associated with RFA. To prevent undesired backward conduction of microwave energy along the applicator shaft, known as "back-diffusion", modern antennas incorporate choke structures and internal cooling systems (water or CO_2 circulation) that dissipate excess heat and maintain antenna efficiency [24]. These design innovations have markedly improved the power handling capability, shape regularity, and reproducibility of ablation zones.

Clinically, MWA has become an established therapeutic option for the treatment of primary and metastatic liver tumors, where it offers higher intratumoral temperatures, shorter ablation times, and reduced susceptibility to vascular heat-sink effects compared to RFA [2, 22]. Its use has progressively expanded to other anatomical sites, including the lung [25], kidney [26], and bone [27], demonstrating

promising results in terms of local tumor control and procedural safety. In recent years, MWA has also been investigated for thyroid nodules [28–30]. Beyond oncological and endocrine applications, microwave energy has also been investigated for cardiac tissue ablation, particularly in the treatment of atrial fibrillation and ventricular tachycardia [31–34]. In this context, microwave power enables the creation of deep and continuous transmural lesions by dielectric heating, overcoming some of the penetration and impedance limitations of conventional RFA. Experimental and early clinical studies using catheter-based microwave applicators have demonstrated the feasibility of achieving effective conduction block without surface charring, highlighting its potential as an alternative thermal modality for complex arrhythmic substrates.

1.3 High-intensity focused ultrasound

High-Intensity Focused Ultrasound is a non-invasive thermal ablation technique that exploits the ability of focused acoustic waves to concentrate mechanical energy deep within biological tissue without affecting intervening structures. As described by Kennedy & James [35], the HIFU system employs one or more large-aperture piezoelectric transducers operating typically between 0.8 and 3 MHz [35–37]. As shown in Figure 1.5, the emitted ultrasound beams are geometrically or electronically focused to a small focal region, usually a few millimeters in diameter, where the acoustic energy converges and the local intensity can exceed $10\,000\,\mathrm{W\,cm^{-2}}$ [37, 38]. Within this focal zone, tissue temperature rises rapidly above $70 - 100\,^{\circ}\mathrm{C}$ due to viscous absorption and nonlinear propagation effects, resulting in instantaneous coagulative necrosis of cells while surrounding and overlying tissues remain below the thermal damage threshold [35, 38, 39].

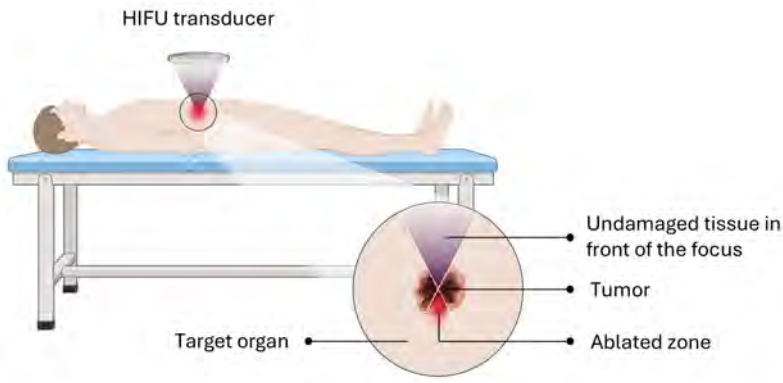

Figure 1.5: Schematic representation of the High-Intensity Focused Ultrasound principle. Acoustic waves generated by a large-aperture transducer are converged and focused within the target organ, where energy deposition raises the temperature above cytotoxic thresholds, producing a well-defined ablated zone that encompasses the tumor. The intervening tissue along the acoustic path remains undamaged, illustrating the high spatial selectivity and non-invasive nature of HIFU therapy.

The biophysical mechanism of HIFU relies on the conversion of acoustic energy into heat through frictional losses as oscillating pressure waves induce microscopic particle motion. In addition to purely thermal effects, very high acoustic amplitudes may induce acoustic cavitation, whereby microbubbles form and collapse, generating localized mechanical disruption [38]. Although this phenomenon can contribute to tissue damage, it is generally controlled, or deliberately minimized, in clinical applications to ensure consistent and reproducible lesion formation. Generally, the acoustic propagation and focusing are modeled by nonlinear formulations such as the Khokhlov–Zabolotskaya–Kuznetsov (KZK) equation, which accounts for attenuation, diffraction, and nonlinearity in soft tissues [40]. Modern implementations combine therapy and imaging within a single platform, leading to MRI[1]-guided (MRgHIFU) and Ultrasound-guided (USgHIFU) systems [42–44]. MR guidance provides submillimetric targeting and proton resonance frequency thermometry, allowing quantitative, real-time temperature monitoring and automatic feedback control during sonication. Ultrasound guidance, conversely, offers dynamic visualization of tissue interfaces and cavitation activity at lower cost, though with less precise temperature quantification. According to Ghanouni et al. [44], the integration of real-time imaging, beam steering, and electronic phase control enables accurate energy deposition in irregular targets and compensation for tissue motion.

Clinically, HIFU is approved for uterine fibroids [45], bone metastases [46], and localized prostate cancer [47], and it is under evaluation for pancreatic [39], hepatic, and intracranial lesions [38, 44]. The technique's primary advantages are its complete non-invasiveness, absence of ionizing radiation, and repeatability, which make it suitable for patients unfit for surgery or requiring organ preservation. Limitations include prolonged treatment durations for large volumes, acoustic reflection and attenuation by bone or gas, and pain or skin erythema from near-field heating [48]. Active research is addressing these issues through adaptive beam-forming algorithms, motion compensation, and the use of microbubbles or nanoparticles to enhance local absorption and shorten ablation times [4, 35, 44].

1.4 Cryoablation

Cryoablation is a thermal ablation modality that destroys tissue by freezing, in direct contrast to heat-based approaches. The technique relies on the Joule–Thomson expansion of compressed gases, most commonly argon for freezing and helium for thawing [49, 50]. As shown in Figure 1.6, when argon undergoes rapid decompression at the cryoprobe tip, local temperatures fall below $-40\,^{\circ}\mathrm{C}$, producing an "ice ball" that encompasses the target lesion [49–52]. During cryoablation, the extent and nature of tissue injury depend on the local temperature gradient within the ice ball. At $-40\,^{\circ}\mathrm{C}$ and below, cells undergo irreversible osmotic and mechanical injury: rapid extracellular and intracellular ice formation leads to dehydration, membrane rupture, and immediate necrosis. Around $-20\,^{\circ}\mathrm{C}$, mechanical disruption predominates, as intracellular ice crystals damage organelles and the cytoskeleton, while endothelial freezing causes vascular thrombosis and ischemic necrosis. Toward the periphery, near $0\,^{\circ}\mathrm{C}$, cooling is sublethal, producing reversible hypothermic stress or delayed apoptosis if exposure is prolonged or repeated.

[1] Magnetic Resonance Imaging (MRI) is a non-invasive medical imaging technique that uses strong magnetic fields and radiofrequency pulses to generate high-resolution images of internal anatomical structures, without exposing the patient to ionizing radiation [41].

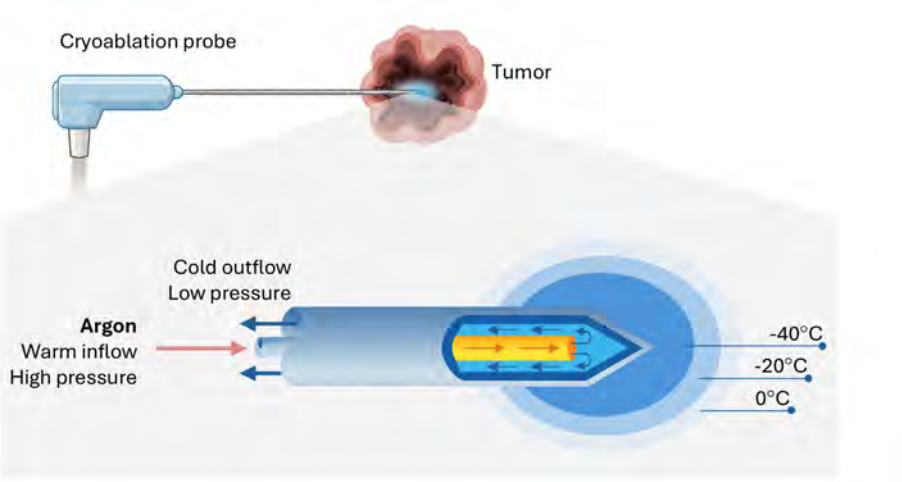

Figure 1.6: Schematic of the cryoablation probe. The cooling gas (argon) flows through the inner chamber at high pressure. Near the tip there is a rapid decompression that results in the supercooling of the gas (Joule-Thomson effect) and gradually of the probe and the surrounding tissues, forming the ice ball. The resulting ice ball forms concentric thermal zones, with cellular necrosis occurring near the probe tip at $-40\,^{\circ}\mathrm{C}$, mechanical and vascular injury around $-20\,^{\circ}\mathrm{C}$, and sublethal, reversible effects near the outer margin at $0\,^{\circ}\mathrm{C}$.

This thermal continuum, from necrosis at $-40\,^{\circ}\mathrm{C}$ to transient injury at $0\,^{\circ}\mathrm{C}$, defines the cryogenic treatment margin and underscores the need to reach sufficiently low and sustained temperatures for complete ablation [14, 49, 53].

A distinctive advantage of cryoablation is the possibility of real-time visualization. Ultrasound Computed Tomography[2] (CT), or MRI can delineate the ice ball with high accuracy, enabling the operator to estimate treatment margins intraprocedurally. This imaging feedback, together with the relative preservation of extracellular matrix, makes cryoablation particularly suitable for tumors in delicate anatomical sites. Clinical applications include renal cortical tumors, hepatic metastases, lung cancer, and painful bone metastases, where maintaining tissue integrity translates into improved functional outcomes [50]. Despite these advantages, cryoablation also has limitations. The procedure is typically longer than heat-based ablations, requires larger applicator diameters, and is less effective near major blood vessels due to the cold-sink effect, in which circulating warm blood counteracts ice propagation. A rare but serious complication is cryoshock, a systemic inflammatory response with thrombocytopenia and coagulopathy, although it is now exceedingly uncommon [14].

1.5 Pulsed Field Ablation

Pulsed Field Ablation is a recently developed non-thermal ablation modality that exploits the biophysical phenomenon of irreversible electroporation (IRE) to selec-

[2]Computed Tomography (CT) is an X-ray–based imaging technique that reconstructs cross-sectional anatomical images by acquiring multiple projections around the patient, providing high spatial resolution and rapid volumetric visualization [54].

tively destroy tissue [55]. Unlike thermal techniques that induce lesion formation through heating or freezing, PFA uses high-voltage ($\sim 2000\,\mathrm{V}$), ultra-short electrical pulses to transiently increase the cell transmembrane potential [55]. As depicted in Figure 1.7, when the electric field surpasses the tissue-specific electroporation threshold, the phospholipid bilayer becomes permeabilized and microscopic, irreversible nanopores form within the cell membrane. This loss of membrane integrity disrupts ionic homeostasis and intracellular balance, ultimately leading to apoptotic cell death rather than coagulative necrosis [3, 55].

A distinctive feature of PFA is its tissue selectivity. As highlighted in [3], different tissues exhibit different voltage thresholds for electroporation. Myocardial cells are highly susceptible, whereas adjacent non-cardiac structures, such as the esophagus, phrenic nerve, and pulmonary veins, require substantially higher electric fields to be injured. As a result, PFA can create effective transmural lesions while markedly reducing the risk of complications classically associated with thermal ablation, including atrio-esophageal fistula, pulmonary vein stenosis, or phrenic nerve palsy. Clinically, PFA has shown very high ablation efficiency and exceptionally rapid procedures. The procedure requests short procedural times (microseconds or nanoseconds), resulting in the electroporation of the cytomembrane [55]. Current applications focus primarily on atrial fibrillation, where PFA has demonstrated high acute success and promising mid-term outcomes [56, 57]. PFA offers instantaneous lesion formation, crisp lesion borders, and preserved atrial mechanical function, attributes particularly advantageous when treating the posterior left atrial wall, a region at high risk during thermal ablation. Looking ahead, ongoing device evolution aims to expand PFA toward linear lesion sets, non-pulmonary vein substrates, and ventricular arrhythmias, supported by improvements in catheter design, pulse dosing optimization, and integration with three-dimensional (3D) electro-anatomical mapping systems [58].

Although PFA eliminates the heat-related complications typical of conventional thermal ablation, specific risks might appear. A notable example is arcing, a phenomenon unique to electroporative energy delivery.

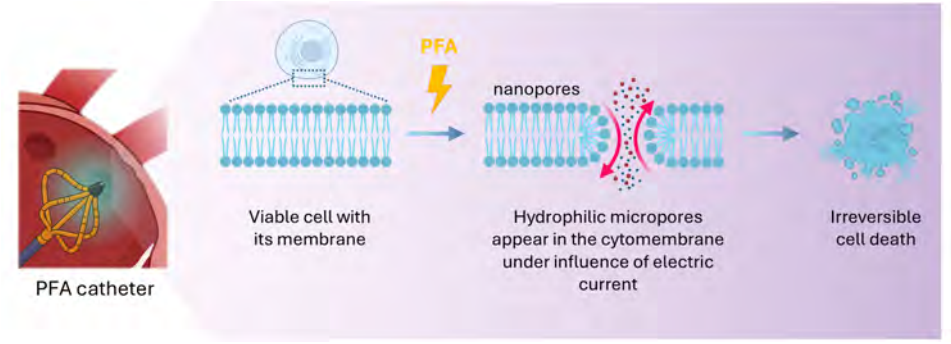

Figure 1.7: Schematic representation of the pulsed field ablation mechanism. High-voltage electrical pulses delivered through the PFA catheter induce irreversible electroporation of cells. When exposed to the electric field, the intact phospholipid bilayer develops hydrophilic nanopores, leading to loss of membrane integrity, disruption of ionic balance, and progression to irreversible cell death, while surrounding tissues remain largely unaffected. Unlike thermal ablation modalities, PFA does not rely on heat generation, thereby minimizing collateral thermal damage.

Arcing arises when very high current densities lead to gas accumulation at the electrode–tissue interface, causing a rapid rise in impedance and ultimately resulting in dielectric breakdown, which may injure the underlying myocardium [59]. Fortunately, this event can be effectively prevented by avoiding direct current waveforms and through appropriate optimization of catheter electrode design [60].

1.6 Laser Ablation

Laser Ablation, also known as Laser-Induced Thermal Therapy (LITT) or Laser Interstitial Thermotherapy, is a minimally invasive photothermal ablation technique that exploits the interaction between coherent light and biological tissue to induce localized hyperthermia and coagulative necrosis [61]. The principle underlying LA is the conversion of optical energy into thermal energy through absorption by tissue chromophores, primarily water, hemoglobin, and proteins, followed by heat diffusion to adjacent regions to produces sublethal injury and apoptosis [62–64].

In practice, laser energy is delivered via flexible quartz optical fibers of diameter from 300 – 600 µm introduced percutaneously or endoscopically into the target tissue [62, 65]. The distal fiber tip may be bare, spherically diffusing, or radially emitting, defining the geometry of the thermal field [62, 66]. Commercial systems are also available that allow the simultaneous use of up to four optical fibers to enlarge the ablation volume. However, this configuration requires high precision in fiber placement to ensure uniform energy distribution [62]. In clinical practice, the number of fibers employed is typically selected according to the size of the lesion, with single or dual fibers used for small nodules and multiple fibers arranged in specific geometries for larger targets, in order to achieve complete and homogeneous ablation. [24, 62]. The emitted photons propagate within the tissue and interact through absorption and scattering mechanisms [4].

For interstitial applications, near-infrared (NIR) wavelengths between 800 and 1064 nm are typically employed, since they achieve an optimal trade-off between penetration depth and energy absorption in a region often termed the therapeutic optical window (650 – 1300 nm) [62, 65, 67] (Figure 1.8). In this range, tissue absorption by water and hemoglobin is moderate, permitting penetration depths of 10 – 15 mm, while still enabling efficient conversion of photon energy into heat [62, 64]. The most widely used sources are diode lasers (800 – 980 nm) and Nd:YAG (Neodymium:Yttrium-Aluminium-Garnet) lasers, with a wavelenght of 1064 nm [62, 68]. Comparative studies have shown that shorter wavelengths (e.g., 980 nm) are more strongly absorbed by water, resulting in sharper temperature gradients and faster heating, whereas 1064 nm radiation penetrates deeper, producing broader but less intense heating profiles [62, 69]. The final lesion geometry depends on optical absorption, scattering, laser exposure time, and tissue perfusion, the latter introducing cooling effects that may reduce the effective ablation volume (heat-sink phenomenon) [62, 70]. Because uncontrolled heating near the fiber tip can lead to carbonization, which abruptly increases local absorption and blocks further light propagation. Thus, modern applicators employ internal cooling mechanisms, typically using saline or CO_2 flow around the optical fiber [61, 62]. Cooling stabilizes energy delivery, enlarges the thermal field and prevents equipment damage, ensuring reproducible lesion formation.

From the clinical perspective, laser ablation has demonstrated efficacy across several organ systems. In oncology, it is applied to hepatic [62], pulmonary [71],

thyroid [70], brain [64], and skin tumors [4], offering high spatial precision in regions where surgical access is difficult or conventional thermal techniques (RFA, MWA) are limited by heat-sink effects. In neuro-oncology, laser ablation is coupled with MRI thermometry for real-time control of temperature and damage estimation, enabling safe ablation of deep-seated lesions [64]. In cardiology, laser ablation has been employed to treat atrial fibrillation and ventricular tachyarrhythmias, where pulsed or continuous-wave laser energy delivered through endocardial catheters produces linear transmural lesions by photothermal conduction along myocardial fibers [72, 73]. Compared to radiofrequency ablation, laser energy offers the advantage of precise lesion geometry, minimal mechanical trauma, and potentially reduced thrombus formation, although procedural optimization and temperature control remain critical for safety and reproducibility.

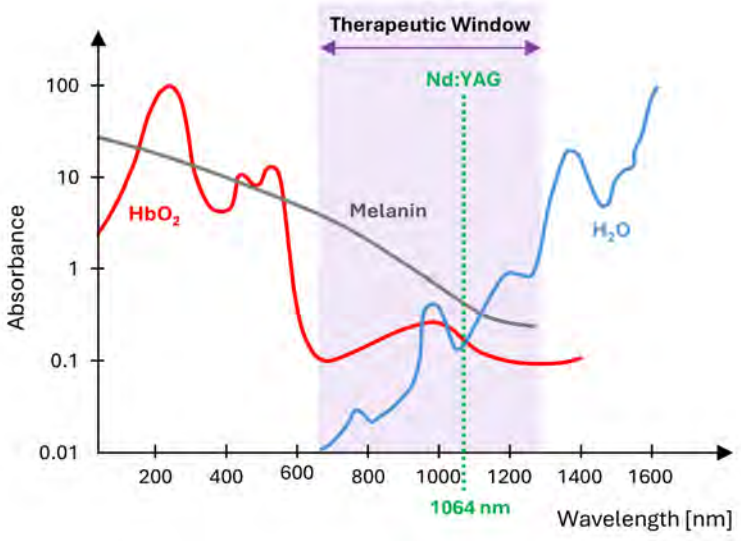

Figure 1.8: Absorption spectra of the main tissue chromophores: oxyhemoglobin (HbO_2), melanin, and water, across the optical wavelength range. The shaded region indicates the near-infrared therapeutic window (approximately 650 – 1300 nm), where absorption by hemoglobin and water is minimized, allowing deeper light penetration into tissue. Within this range, Nd:YAG lasers (1064 nm) are commonly used for interstitial laser ablation, providing an optimal balance between tissue penetration and controlled thermal energy deposition [67].

2

Thermal Ablation Applications

This chapter provides an overview of the main clinical applications of thermal ablation, focusing on cardiac arrhythmia treatment and tumor ablation. The first section addresses cardiac ablation, describing the biophysical principles and clinical use of different energy sources for the modification of arrhythmogenic substrates. The second section shifts to oncological applications, reviewing conventional thermal ablation techniques and their limitations in terms of spatial selectivity. Finally, nanoparticle-mediated photothermal therapies are introduced as an emerging strategy to enhance confinement of thermal damage within tumor tissue.

2.1 Cardiac Ablation

Cardiac ablation has progressively become one of the most important interventional strategies for arrhythmia management, especially atrial fibrillation and ventricular tachyarrhythmias, conditions that are associated with high morbidity and mortality when inadequately controlled [74]. Atrial fibrillation (AF) is characterized by chaotic and rapid electrical activation of the atria. This condition may lead to an irregular and often rapid ventricular response, impaired cardiac efficiency, and an increased risk of thromboembolic events such as stroke [75]. Ventricular tachycardia (VT), on the other hand, originates from abnormal electrical circuits within ventricles and can rapidly degenerate into ventricular fibrillation, a life-threatening condition responsible for sudden cardiac death [76]. The principle underlying the cardiac ablation procedure is the creation of controlled thermal lesions within cardiac tissue to interrupt abnormal electrical conduction pathways and prevent the perpetuation of re-entrant circuits or ectopic foci responsible for arrhythmia [74]. Figure 2.1 schematically illustrates the operating principle of cardiac ablation in the treatment of atrial fibrillation, showing how targeted lesions are created to block the propagation of aberrant atrial impulses.

In clinical practice, catheter ablation has become the standard interventional approach for atrial fibrillation, where the primary goal is the electrical isolation of the pulmonary veins to prevent ectopic triggers from sustaining the arrhythmia. Multiple randomized clinical trials have shown that this strategy, regardless of

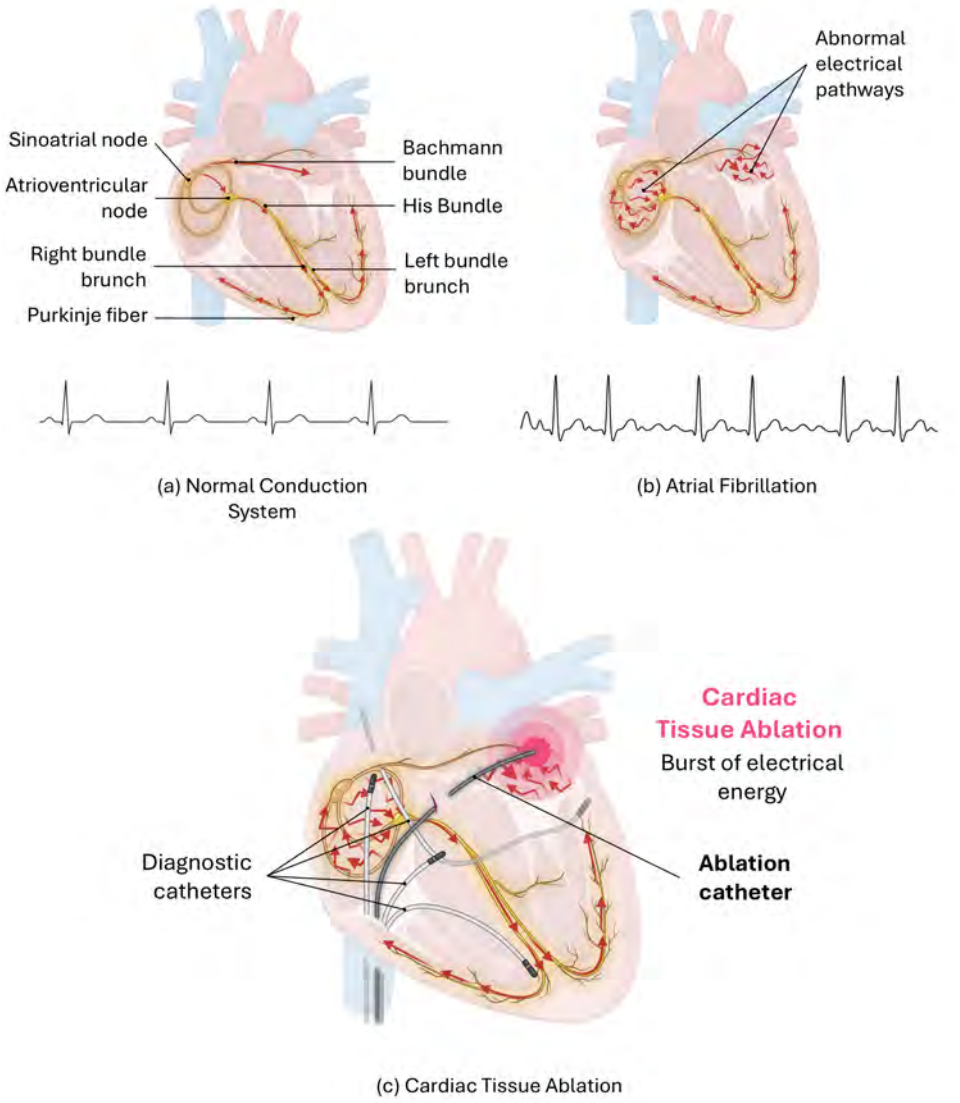

Figure 2.1: Schematic representation of cardiac ablation for atrial fibrillation. (a) The normal cardiac conduction system, including the sinoatrial node (natural heart pacemaker), atrioventricular node, His bundle, right and left bundle branches, and Purkinje fibers, ensures the orderly propagation of impulses that coordinate atrial and ventricular contraction. This is reflected in the electrocardiogram (ECG) trace below, showing the characteristic sequence of the P wave (atrial depolarization), QRS complex (ventricular depolarization), and T wave (ventricular repolarization), which correspond to the synchronized cardiac cycle. (b) In atrial fibrillation, abnormal electrical pathways and ectopic foci in the atria disrupt this physiological sequence, generating chaotic atrial activity and producing the irregular, rapid rhythm visible in the ECG trace. (c) Cardiac tissue ablation aims to restore sinus rhythm by selectively eliminating arrhythmogenic substrates. Diagnostic catheters map intracardiac electrical activity to identify abnormal conduction zones, while ablation catheters deliver targeted energy, producing controlled lesions that interrupt pathological circuits. This localized tissue modification isolates or removes the ectopic sources of excitation, facilitating the re-establishment of stable conduction and normal sinus rhythm.

the specific energy source employed, provides superior rhythm control, symptom relief, and quality-of-life improvement compared with antiarrhythmic drug therapy. It may also confer long-term benefits, including reduced stroke risk and slower progression of heart failure [77, 78].

The choice of energy source and procedural strategy is increasingly guided by considerations of safety, selectivity, and durability of lesions, with ongoing research into computational modeling, imaging integration, and novel catheter designs to optimize outcomes. Thus, cardiac ablation represents the convergence of electrophysiological insight, biophysical principles, and technological innovation, offering a minimally invasive and highly effective approach to modifying diseased cardiac tissue and transforming the management of rhythm disorders.

Among all the ablation techniques presented in Chapter 1, RFA has historically been the most widely adopted for the cardic ablation [79]. Despite its effectiveness, RFA carries thermal-related risks, including injury to adjacent structures such as the esophagus, phrenic nerve, and coronary arteries. Consequently, recent advancements have focused on improving lesion control and procedural safety through contact force–sensing catheters, lesion quality indices, and strategies to limit collateral damage [80]. Building on the same therapeutic principle but using different physical mechanisms, other alternative energy sources have been developed. Cryoablation achieves tissue destruction through extreme cooling, enabling stable catheter contact and reduced risk to surrounding structures. More recently, pulsed-field ablation, based on irreversible electroporation, has emerged as a promising alternative due to its myocardial selectivity and non-thermal mechanism.

Laser ablation relies on precise light-to-heat conversion for controlled lesion formation within the target volume. This high degree of spatial control makes the technique particularly appealing for cardiac applications, where selective energy delivery and minimal collateral damage are critical to preserve surrounding structures. Although the clinical use of laser ablation for cardiac arrhythmias remains limited compared to RFA or cryothermal techniques, several experimental studies have demonstrated its potential to create precise and controllable lesions in myocardial tissue [81]. Early investigations explored catheter-based laser delivery systems capable of producing both focal and linear lesions, reporting encouraging results in terms of lesion continuity and depth, particularly in animal models. More recent work has investigated novel catheter designs with side-firing fibers to enable circumferential or linear applications, suggesting that laser energy could represent a versatile alternative in substrate modification for atrial and ventricular arrhythmias [82].

Despite these promising findings, laser ablation has remained largely unexplored in the cardiac ablation arena, mainly due to the scarcity of systematic research, the lack of standardized protocols, and the competition from well-established modalities. For this reason, one of the main research directions of this thesis focuses on the development of advanced computational model of laser ablation in cardiac tissue, aimed at elucidating the underlying biothermal mechanisms and predicting lesion formation with high spatial and temporal accuracy (see Chapter 6). Such in silico investigations may help bridge the current knowledge gap and lay the foundation for future translational studies, with the ultimate goal of assessing whether laser ablation could become a clinically viable option in the treatment of cardiac arrhythmias.

2.2 NPs-mediated tumor ablation

Cancer continues to be a significant global health concern. However, the field of cancer treatment has seen advancements, and thermal therapy has emerged as a promising and less invasive alternative to traditional surgical procedures [1]. This approach offers unique advantages including enhanced selectivity, reduced hospitalization costs and lower morbidity rates [1]. Moreover, thermal therapy is particularly beneficial for patients who may not be eligible for conventional treatments due to various factors such as age, medical condition, or other limitations. Thermal ablation therapies encompass a range of techniques that utilize different energy sources to target and damage cancerous cells.

Among the different ablation modalities clinically adopted for tumor treatment, including RFA, MWA, cryogenic, and LA approaches, each has demonstrated efficacy in inducing local coagulative necrosis and improving survival outcomes in selected patients [24]. RFA, for example, has become a standard alternative for patients with small hepatocellular carcinomas who are not surgical candidates, while MWA is increasingly used for larger lesions due to its ability to generate more extensive ablation volumes with reduced sensitivity to perfusion effects [24]. LA has also shown encouraging results in treating hepatic and other solid tumors [9]. Despite these advances, a major limitation shared by all conventional thermal ablation techniques is their limited spatial confinement, since the heat-induced injury, although more localized than in conventional surgery, can still extend beyond the malignant tissue into adjacent healthy structures, thereby increasing the risk of complications and narrowing the therapeutic window.

For this reason, growing interest is now directed toward nanoparticle-mediated photothermal therapies (PTT), aiming to overcome the intrinsic non-selectivity of conventional thermal strategies [83]. The central rationale is to concentrate the thermal effect within the tumor mass through the use of photothermal agents (PTA), while sparing surrounding healthy tissue [83, 84]. Thus, PTT employs PTAs to absorb incident light, most commonly in the NIR, and convert it into heat, generating highly localized hyperthermia capable of inducing irreversible protein denaturation, membrane disruption, and subsequent cell death [84]. Once selectively accumulated in the tumor region these agents act as localized heat amplifiers and the resulting thermal effect is spatially and temporally confined to the malignant region [85]. In general, those PTAs have strong light absorption at the NIR wavelength, good photostability, biocompatibility without light-source activation, and enhanced photothermal conversion efficiency [86, 87]. Following the Figure 2.2, upon illumination, PTAs interact with light through both absorption and scattering, with the efficiency of these processes determined by their intrinsic physicochemical properties [88]. Only a portion of the absorbed photons is ultimately converted into heat: following photon absorption, electrons are promoted from the ground state to an excited singlet state, and as they relax back toward lower energy levels through non-radiative decay pathways, the excess energy is released in the form of heat. Among PTAs, Nanoparticles (NPs) are colloidal structures typically ranging from 1 to 1000 nm that display physicochemical behaviors markedly distinct from those of bulk materials [89]. Their nanoscale dimensions, large surface-area-to-volume ratio, and highly customizable surface chemistry have positioned them as versatile platforms in numerous biomedical applications, including photothermal therapy, diagnostic imaging, biosensing, and regenerative medicine [90, 91].

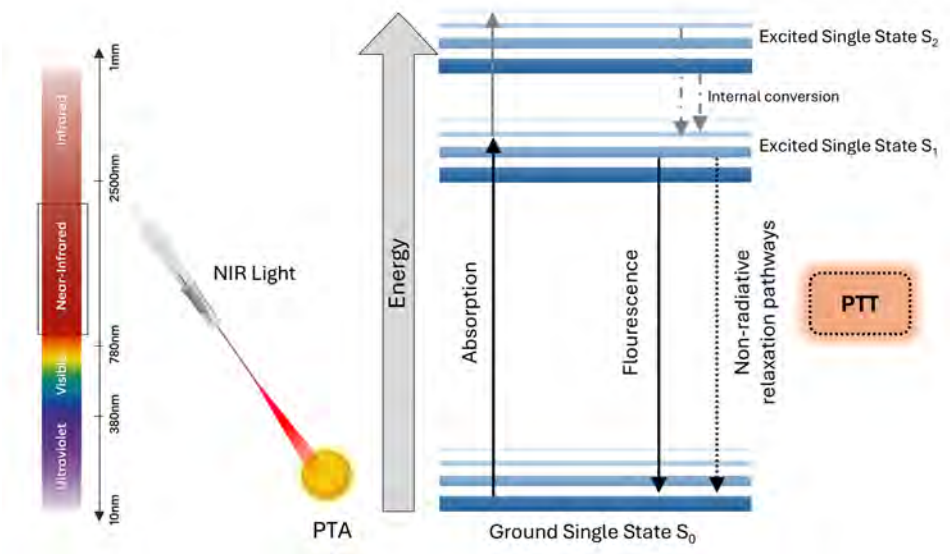

Figure 2.2: Photothermal conversion mechanism of a PTA. Upon irradiation with NIR light, the PTA absorbs photons and undergoes electronic excitation from the ground single state (S_0) to higher excited single states (S_1, S_2). While a fraction of this energy may be released as fluorescence, most of it relaxes back to lower energy levels through non-radiative decay pathways, including internal conversion. The dissipation of this excess energy as heat constitutes the basis of PTT, enabling localized hyperthermia within the target tissue [85].

The ability to precisely tailor their composition and morphology (e.g., nanorods, nanoshells, or nanocages) enables improved interactions with biological environments, providing innovative opportunities to enhance therapeutic performance and accuracy [89, 92].

In the context of laser ablation thermal therapy, gold-based nanoparticles (AuNPs) have gained substantial attention for tumor treatment for their unique tunable optical and biophysical properties and even more for their excellent biocompatibility [85, 93, 94]. AuNPs are excellent for PTT because they exhibit unique optical properties governed by the phenomenon of Localized Surface Plasmon Resonance (LSPR) (Figure 2.3). When the AuNPs are irradiated by an electromagnetic field, there is the excitation of the electrons in the conduction band and the collective oscillation of these conduction-band electrons. Thus, the interaction between incident light and AuNPs induces a collective oscillation of conduction electrons, known as a surface plasmon, in which the electron cloud moves coherently against the positively charged ionic lattice [95]. This oscillation occurs at a characteristic frequency which, when matched by the frequency of the incoming light, results in plasmonic resonance, enabling highly efficient transfer of electromagnetic energy to the electronic cloud of the nanoparticle. As a consequence, the particle exhibits greatly enhanced absorption and scattering efficiencies compared to bulk gold. When this resonant phenomenon is spatially confined to the nanoscale, i.e., at the level of an individual NP, it is termed localized surface plasmon resonance, making AuNPs act as powerful nanoscale optical antennas capable of concentrating incoming electromagnetic energy [95].

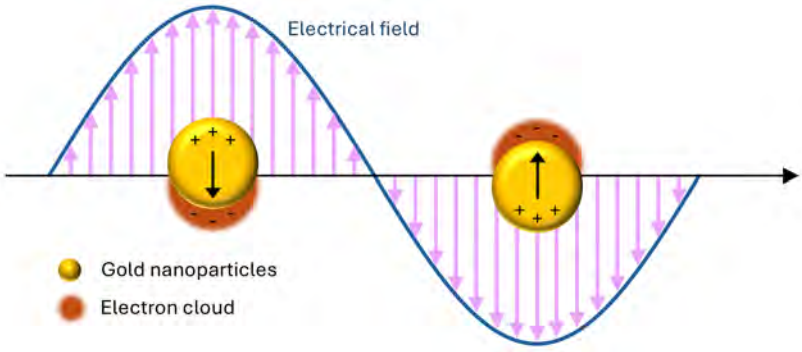

Figure 2.3: Schematic representation of localized surface plasmon resonance in a gold nanoparticle. The oscillating electromagnetic field of the incident light drives the collective motion of the conduction-band electrons, causing the electron cloud to shift coherently with respect to the positively charged ionic core. At the plasmon resonance frequency, this displacement is maximized, leading to strong local field enhancement and efficient absorption of optical energy, which underlies the photothermal behavior of AuNPs [85].

When AuNPs are excited at their LSPR wavelength, the absorbed optical energy is dissipated through non-radiative relaxation pathways, primarily via electron–phonon and phonon–phonon interactions [95]. These ultrafast processes, occurring over picoseconds, lead to rapid thermalization and the generation of intensely localized heat within the NP. This plasmonic photothermal conversion produces steep temperature gradients confined to the nanoscale, with heat subsequently diffusing into the surrounding medium over nanometer to micrometer distances. In this way, LSPR enhances optical absorption and allows precise control and confined thermal effects, enabling highly efficient photothermal heating and selective hyperthermia of target cells while minimizing collateral thermal injury [95].

The LSPR frequency, and consequently the optical response of the nanoparticle, depends sensitively on its size, shape, aspect ratio, and dielectric environment [96]. Spherical AuNPs typically exhibit resonance peaks around 520 nm in the visible range, while anisotropic geometries such as nanorods (NR), nanoshells, and nanocages (NC) shift the resonance into the NIR spectral window (650 – 1300 nm), where biological tissues exhibit minimal absorption and scattering, allowing deeper photon penetration [93, 94].

AuNPs can be engineered during synthesis by precisely controlling their morphology (e.g., nanorods, nanoshells, or nanocages), size, and composition, thereby enabling accurate tuning of their plasmonic resonance wavelength. This optimization allows the resonance peak to be spectrally matched to the emission wavelengths of clinically used laser systems (e.g., 808 nm, 980 nm, or 1064 nm), thus maximizing energy coupling efficiency and enhancing the overall photothermal conversion performance [95]. Additionally, the optical absorption cross-section of AuNPs under LSPR excitation is several orders of magnitude higher than that of endogenous chromophores such as hemoglobin or melanin, which significantly enhances the optical absorption coefficient of the nanoparticle-loaded tumor region. This effect improves light-to-heat conversion efficiency and compensates for photon attenuation in highly scattering biological media. The thermal response can be modulated

by controlling both NP concentration and laser fluence, achieving highly tunable temperature distributions suitable for minimally invasive ablation. This synergy between plasmonic nanostructures and laser irradiation forms the scientific basis for nanoparticle-mediated laser ablation, offering a pathway toward controlled, targeted, and minimally invasive oncological therapies.

Figure 2.4 shows a schematic representation of AuNPs-mediated laser abalation. Upon laser irradiation, AuNPs convert optical energy into heat with high efficiency, thereby producing localized hyperthermia sufficient to induce irreversible cell death within the tumor core while minimizing collateral damage [95].

Following this promising and innovative synergy between nanotechnology and laser-based thermal ablation for the treatment of solid tumors, the second major research direction of this thesis focuses on the experimental development of a dedicated setup to evaluate the effectiveness of AuNP-mediated laser ablation. This activity involves a progressive approach, beginning with controlled tests in synthetic tissue-mimicking phantoms and subsequently extending to an initial *ex vivo* exploration through experimental campaigns conducted on porcine liver tissue (see Experimental Activities).

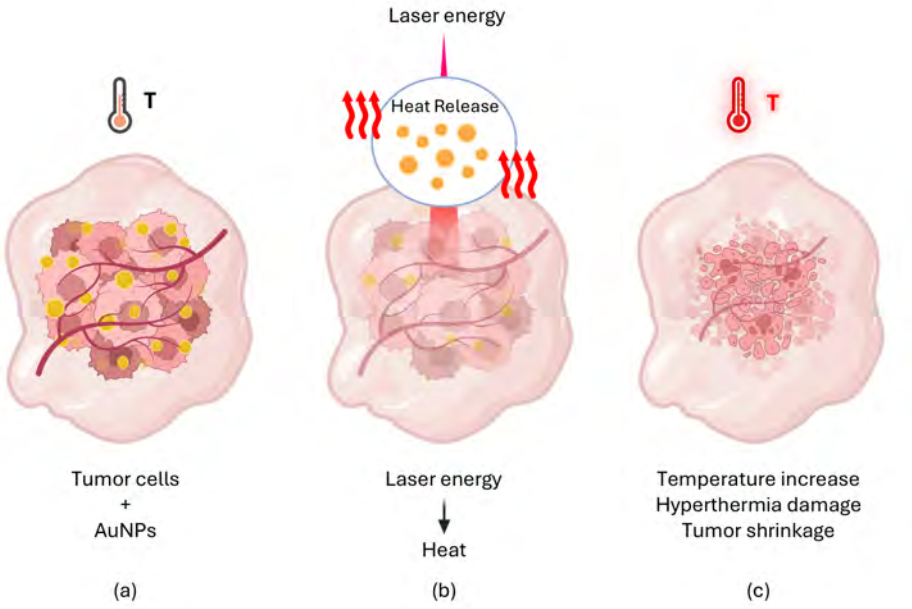

Figure 2.4: Schematic representation of nanoparticle-mediated laser thermal ablation. (a) Gold nanoparticles (AuNPs) accumulate within the tumor mass. (b) Upon application of an external laser source, the nanoparticles act as photothermal agents and efficiently convert the incoming light into localized heat, amplifying the thermal effect inside the tumor mass. (c) The consequent increase in temperature induces hyperthermia, leading to protein denaturation, irreversible cellular injury, and progressive shrinkage of the neoplastic lesion, while minimizing injury to the surrounding healthy tissue.

Experimental Activities

3

CAD Design and 3D Printing

Having outlined in the previous sections the clinical background (Chapter 1) and the therapeutic relevance of laser ablation (Chapter 2), ranging from arrhythmia management in cardiac tissue to tumor destruction, it becomes essential to bridge the gap between theory and clinical practice through a dedicated experimental investigation.

Computational studies alone, while powerful, require reliable validation against controlled measurements; similarly, the clinical potential of laser ablation can only be fully assessed once its fundamental thermal mechanisms are quantified under reproducible laboratory conditions. For this purpose, we developed a custom experimental apparatus that enables systematic exploration of laser–tissue interactions and provides accurate thermal feedback throughout ablation procedures. The rationale behind this platform is threefold: to reproduce laser energy delivery in a repeatable and controllable environment, to generate high-quality thermal datasets suitable for calibrating computational models, and to assess safety margins and lesion dynamics under conditions that mimic the clinical setting.

The apparatus combines additively manufactured structural components with fiber-optic sensing technology, ensuring both geometric reproducibility of applicator placement and metrological robustness in temperature acquisition. Thus, thermal ablation experiments demand a platform that tightly controls geometry and boundary conditions around the applicator, guaranteeing repeatable sensor placement with sub-millimetric tolerance. A dedicated setup that standardizes the applicator–tissue interface and embeds metrologically robust thermometry therefore becomes a prerequisite to design, compare, and tune ablation protocols in a reproducible way.

The experimental setup developed in this study consists of a custom 3D-printed holder designed to accommodate both the tissue sample and the synthetic phantom engineered to mimic the thermal and optical behavior of biological tissue, a set of optical fibers equipped with Fiber Bragg Grating (FBG) sensors for distributed temperature monitoring, and a laser generator responsible for delivering the optical energy required to induce the ablation process. Building a custom holder serves to enforce geometric repeatability of the applicator axis, laser applicator tip depth,

and standoff distances to sensing points through integrated guides and datum surfaces in the fixture. Moreover, it embeds channels and seats that protect optical fibers against strain and micro-bending. These design choices translate directly into higher-quality datasets for calibrating optical–thermal models and for testing algorithmic strategies. In the folling sections we will explore each components.

3.1 Custom Experimental Holder Design and Fabrication

To materialize the experimental platform, the first stage consisted in the development of a custom holder. The design process represented a crucial step where mechanical constraints, sensing requirements, and optical access were merged into a single integrated structure. Therefore, we proceeded with the Computer Aided Design (CAD) of the custom fixture, using a parametric modeling software (Autodesk Fusion). The virtual prototype was created to incorporate all the essential features: a central chamber to host the tissue sample/phantom, dedicated slots for optical fibers, and mechanical guides for the laser applicator. The parametric approach was particularly advantageous because it enabled the rapid modification of geometric dimensions and tolerances to adapt to different experimental conditions. Iterative CAD refinement ensured that the holder could be easily assembled, disassembled, and reconfigured, while guaranteeing robustness and repeatability in positioning. Figure 3.1 shows the holder CAD project and its specifications.

To ensure proper positioning of both the thermal sensors and the laser applicator, specific structural details were embedded in the CAD design. In particular, the holes in the base (A) were designed to host the optical fibers used for temperature measurements during the ablation experiments. Each hole has a diameter of 1 mm, which allows for the smooth insertion and stable positioning of the optical fibers without excessive clearance. The hat (C) is equipped with an extruded guiding channel specifically conceived for the insertion of the laser delivery fiber. Since the laser beam is highly collimated and extremely sensitive to angular deviations, this guidance feature ensures correct alignment and directionality. In turn, this design minimizes variations in energy deposition, prevents undesired beam scattering or “banding” effects in the laser fiber, and guarantees the reproducibility of the experiments across repeated trials.

Figure 3.2 shows the relative positioning of the optical sensing fibers and the laser fiber applicator in detail. We used 4 optical fibers (A, B, C, D) for the temperature monitoring. The holes for the optical fibers are spaced at 2 mm intervals from one another (Figure 3.2.(b)), thus providing a distributed temperature sampling with sub-millimeter resolution. Moreover, the distance between the laser fiber and the optical fibers A, C, and D is set to 2 mm along the z-axis. This controlled geometry allows for consistent mapping of thermal gradients and provides highly reliable experimental datasets.

The translation from the CAD model into a tangible prototype was achieved through 3D printing, a class of additive manufacturing techniques in which material is deposited layer by layer to construct complex geometries directly from digital models. Unlike subtractive manufacturing, which relies on the removal of material from a bulk block, additive processes allow for internal cavities, smooth channels, and fine details to be embedded within the structure without additional steps.

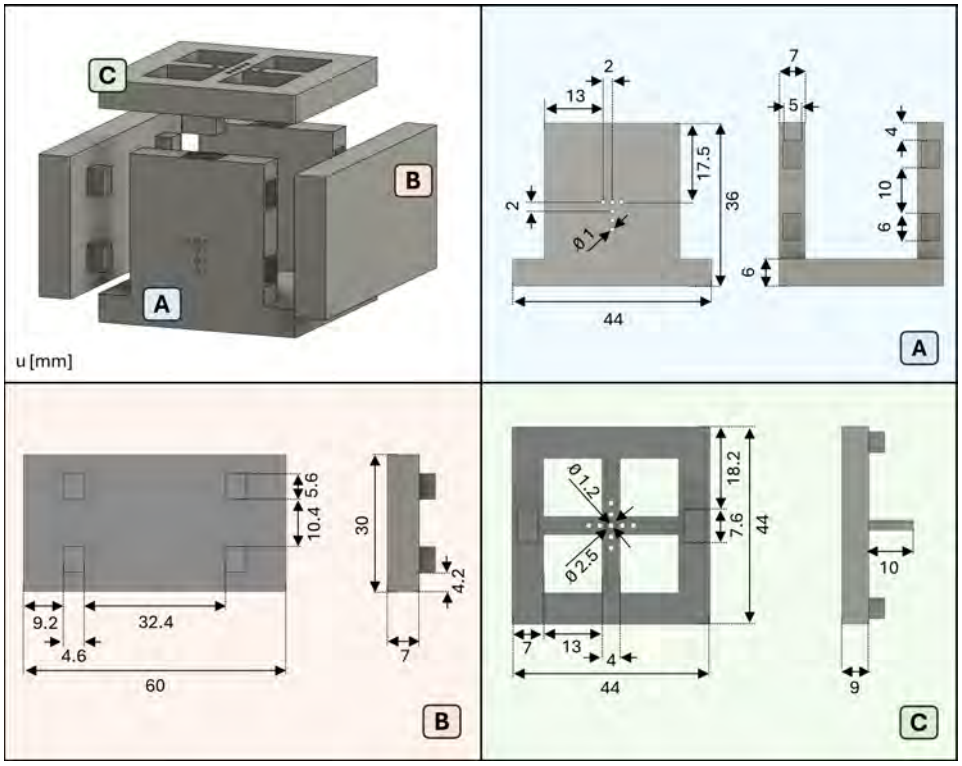

Figure 3.1: Custom holder design and composition. Three-dimensional CAD model and technical drawings of the custom holder developed for laser ablation experiments. The assembly consists of three main components: the base (A), designed with 1 mm holes to accommodate the optical fibers for temperature monitoring; the lateral wall (B), providing structural stability and mechanical coupling to the base; and the top hat (C), which incorporates an extruded guiding channel to precisely align the laser delivery fiber. The detailed dimensional views highlight the spatial arrangement of the components and the precise positioning tolerances (± 0.1 mm) that ensure reproducibility in the relative placement of the FBG sensors and the laser applicator during experimental tests.

Among the various additive manufacturing techniques available for prototyping and biomedical applications, the most established ones include Stereolithography (SLA), Selective Laser Sintering (SLS), and Fused Deposition Modeling (FDM), each characterized by distinct material compatibilities, resolutions, and mechanical outcomes [97]. These technologies are schematically compared in Figure 3.3.

SLA is a photopolymerization-based technique that builds 3D structures by selectively curing liquid resin using a focused ultraviolet (UV) laser or digital light projector [98]. The laser scans the resin surface following the cross-sectional pattern of the CAD model, solidifying one thin layer at a time. Once each layer is cured, the printing platform moves vertically to allow the next layer to be exposed and polymerized. SLA can achieve extremely high spatial resolutions ($< 10\,\mu m$) and smooth surface finishes, making it ideal for microscale biomedical components, optical housings, and molds for soft materials. However, it is generally limited to photopolymeric materials, which may exhibit restricted biocompatibility and lower thermal stability compared to engineering thermoplastics [98]. SLS, in contrast,

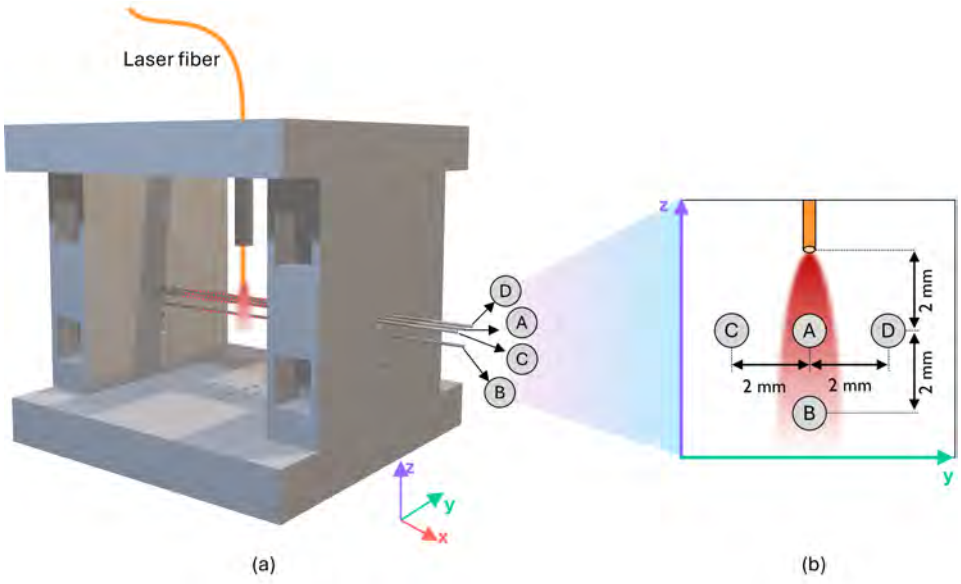

Figure 3.2: Geometric arrangement of the four fiber optic sensing fibers (A, B, C, D) with respect to the laser delivery fiber inside the custom holder. Panel (a) shows the integration of the fibers within the structure, while panel (b) provides a magnified view of their relative spacing. The sensing fibers are positioned in dedicated holder channels separated by 2 mm, and the laser fiber is placed at a fixed 2 mm distance from fibers A, C, and D along the z-axis.

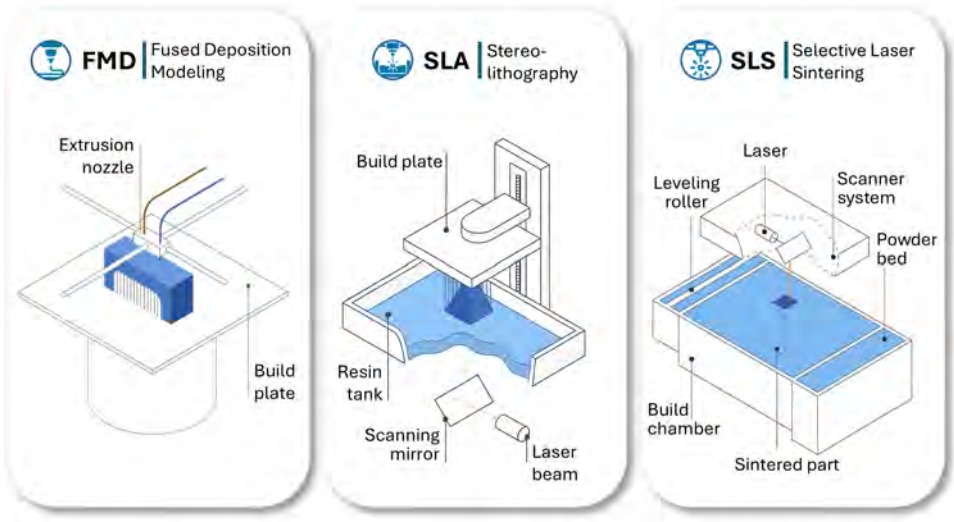

Figure 3.3: Schematic representation of the three main additive manufacturing techniques: Fused Deposition Modeling, where a thermoplastic filament is extruded through a heated nozzle layer by layer; Stereolithography, which uses a laser to selectively cure liquid resin in a tank; and Selective Laser Sintering, where a laser fuses powdered material to build solid parts. Each process is illustrated with its key components.

employs a high-power infrared or CO_2 laser to selectively fuse, layer by layer, powdered material, commonly nylon, polyamide, or metal powders [99].

The unsintered powder acts as a natural support for overhanging structures, eliminating the need for external supports. SLS produces mechanically robust parts and is widely used for functional prototypes and load-bearing components, but the process is typically more expensive and requires post-processing steps (such as depowdering or surface finishing) to achieve the desired smoothness and dimensional accuracy [99].

For this work, we adopted the FDM method. This technique operates by extruding a thermoplastic filament, heated above its glass transition temperature, through a nozzle that deposits successive layers according to the digital slicing of the CAD model [100]. Each layer fuses with the previous one, progressively constructing the three-dimensional object. The choice of FDM was dictated by several advantages: accessibility and low cost, mechanical robustness of the printed parts, and the possibility of readily producing large components with integrated features. Moreover, FDM offers a wide selection of printable polymers, among which polylactic acid (PLA) was selected for our prototypes. PLA combines ease of processing, dimensional stability, and sufficient mechanical strength for fixture applications. Its relatively low thermal conductivity ($\sim 0.13\,\mathrm{W\,mK^{-1}}$) is advantageous, as it minimizes undesired heat transfer from the ablation region to the surrounding support, preserving the accuracy of the thermal measurements. Additionally, PLA is biocompatible in non-implantable contexts and widely used in biomedical prototyping, further justifying its selection [101]. The resolution and precision of FDM depend on a number of process parameters, such as nozzle diameter, layer height, infill density, raster orientation, and printing temperature [100]. For our design, a nozzle of 0.4 mm and a layer height of 0.1 – 0.2 mm were used, yielding a good compromise between print speed and geometric accuracy. Hexagonal infill patterns with densities of 40 – 60 % were selected to balance mechanical stability with reduced material usage and weight. Careful control of cooling rates and printing speed was also required to avoid warping, especially in elongated structures such as sensor channels. A further advantage of FDM is the ability to perform rapid prototyping, i.e., producing multiple iterations of the fixture in a short time frame to optimize functionality. Several versions of the holder were fabricated and tested, each iteration improving aspects such as the rigidity of the walls, the accessibility for sensor insertion, and the ease of cleaning and reuse. This flexibility is crucial in experimental biomedical research, where design requirements evolve as protocols are refined. For the FDM technique, the 3D printer Creality Ender-3 V2 (Creality, Shenzhen, China) [102] was used in this research work. Figure 3.4 highlights its principal components. For the detailed description of all parts, please refer to [102]. Starting from the CAD model, the geometry was exported in the STL[1] format and processed using the slicing software Sovol 3D Cura to build the G-code[2] file with the printing parameters such as layer height, infill density, and nozzle temperature, optimized for PLA. The sliced code was then transferred to the printer, which produced the physical prototype. As illustrated in Figure 3.5, the workflow proceeds from the initial CAD model (1) to the printing of the individual parts (2).

[1] STL file (Stereolithography file) is a standard 3D model format used to represent the geometry of an object through a tessellated mesh of triangular facets, commonly employed in computer-aided design and additive manufacturing.

[2] G-code file is a machine-readable instruction set generated by a slicing software, specifying the nozzle trajectory, extrusion rate, temperatures, and layer-by-layer movements required for the 3D printer to fabricate the object.

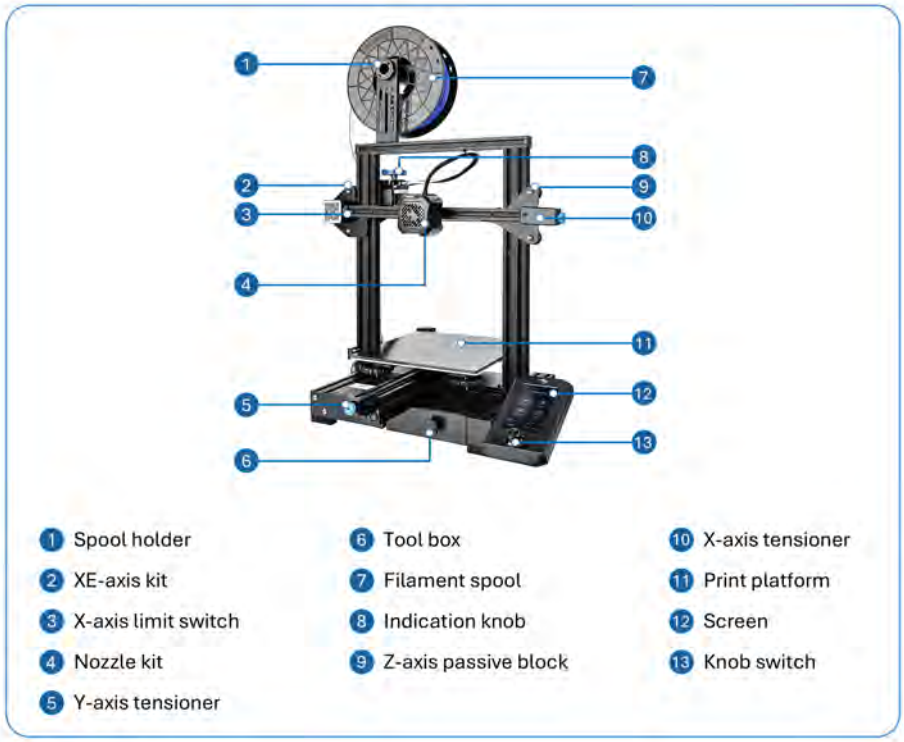

Figure 3.4: Creality Ender-3 V2 printer used for the fabrication of the custom PLA holder employed in the laser ablation experiments. The system operates through controlled extrusion of a thermoplastic filament (PLA) along motorized X-, Y-, and Z-axes, depositing successive layers via a heated nozzle onto the build platform. Each layer fuses with the previous one as it cools, enabling the construction of complex geometries with high dimensional accuracy. The printer integrates the standard mechanical and electronic modules identified in the illustration as the print platform, the filament and holder spool, passive Z-axis block and screen. All the components contribute to precise positioning, stable motion control, and reliable deposition during fabrication. Moreover, the Creality Ender-3 V2 combines mechanical stability, ease of calibration, and open-source firmware control, making it suitable for precise and repeatable fabrication of experimental components and laboratory fixtures.

Once printed the base, lateral walls, and top hat (3), these components were assembled to form the custom PLA holder (4), designed to host the optical fibers and the laser applicator with precise and reproducible alignment. This integrated process ensured both design flexibility and dimensional consistency, key aspects for achieving reliable thermal measurements during the ablation experiments.

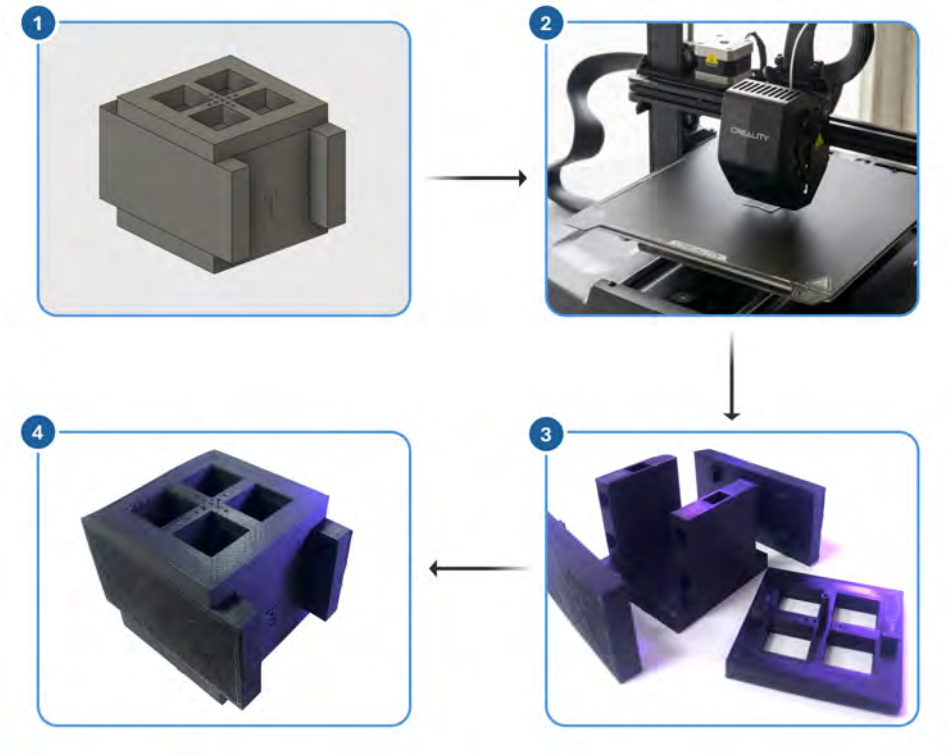

Figure 3.5: Printing workflow of the custom PLA holder used in the experimental setup. The sequence illustrates the transition from the CAD design to the final assembled component. Step (1) shows the 3D model developed; step (2) depicts the printing process on the Creality Ender-3 V2 system; step (3) presents the individually printed parts: base, side walls, and top hat, each produced with high dimensional accuracy; and step (4) shows the final assembly of the modular holder.

3.2 Temperature Measuring

The core element of the experimental apparatus is the thermal monitoring system, based on fiber optic sensors. Specifically, we employed Fiber Bragg Grating sensors. The choice of this technology is motivated by the need for accurate, spatially resolved, and real-time temperature measurements during laser ablation experiments, under conditions where traditional metallic thermocouples or thermistors may introduce artifacts [103]. They are susceptible to electromagnetic interference, slow response time, or thermal conduction along the probe body, all of which compromise measurement accuracy [103, 104]. FBGs, being fully dielectric and minimally invasive, provide a metrologically robust solution that can be integrated seamlessly into the custom-printed holder described above. Moreover, the FBG technology has high sensitivity, multi-parameter sensing capability, and serial multiplexability, allowing multipoint sensing with a single fiber increasing the sensor capacity to collect temperature mapping in a single experiment.

Conventional FBGs are typically inscribed using a UV laser and a phase mask, which induces permanent refractive index changes in photosensitive fibers [105]. More recently, femtosecond laser inscription has become increasingly relevant, as

it allows the fabrication of gratings in non-photosensitive fibers, producing devices with excellent thermal stability (up to 1000 °C for silica) [106]. This robustness is particularly valuable for applications in thermal ablation, where temperatures may transiently exceed 100 °C in proximity to the ablation zone.

Working Principle. The FBG is created by introducing a periodic modulation of refractive index within the core of an optical fiber, typically a single-mode fiber. This modulation, created through laser inscription techniques, acts as a distributed Bragg reflector that reflects a narrow band of wavelengths while transmitting all others. As shown in Figure 3.6, the FBG behaves as an optical band pass filter.

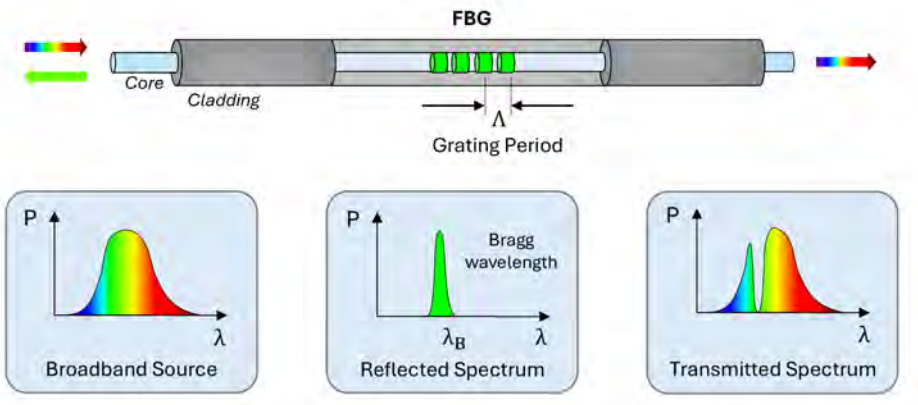

Figure 3.6: Schematic representation of the operating principle of a Fiber Bragg Grating (FBG). A periodic modulation of refractive index is inscribed in the fiber core. When illuminated by a broadband optical source, the FBG reflects a narrow spectral band centered at its nominal Bragg wavelength λ_B, defined by the grating period and effective refractive index, while the remaining wavelengths are transmitted through the fiber.

The reflected wavelength, known as the Bragg wavelength (λ_B) is given by the fundamental relation:

$$\lambda_B = 2n_{\text{eff}}\Lambda \tag{3.1}$$

where n_{eff} is the effective fiber core refractive index and Λ is the grating period, e.g. the distance between two regions with high refractive index values.

Multiple temperature measurements along a single fiber, e.g. FBG array, can be achieved by embedding different gratings with distinct nominal λ_B, in the fiber itself [107, 108]. Figure 3.7 shows an example of an array with 3 FBGs. This configuration enables quasi-distributed sensing.

Any external perturbation that modifies either the effective refractive index of the fiber core (n_{eff}) or the grating period (Λ) induces a shift of the Bragg wavelength ($\Delta\lambda_B$). These perturbations typically arise from two main sources: axial mechanical strain, which stretches or compresses the grating and thus changes Λ, and temperature variations, which simultaneously affect the thermo-optic coefficient of silica (altering n_{eff}) and cause thermal expansion (altering Λ). The combined effect is a shift of the reflected wavelength peak $\lambda_{B,f}$, which can be directly related to the applied strain or temperature change (Figure 3.8).

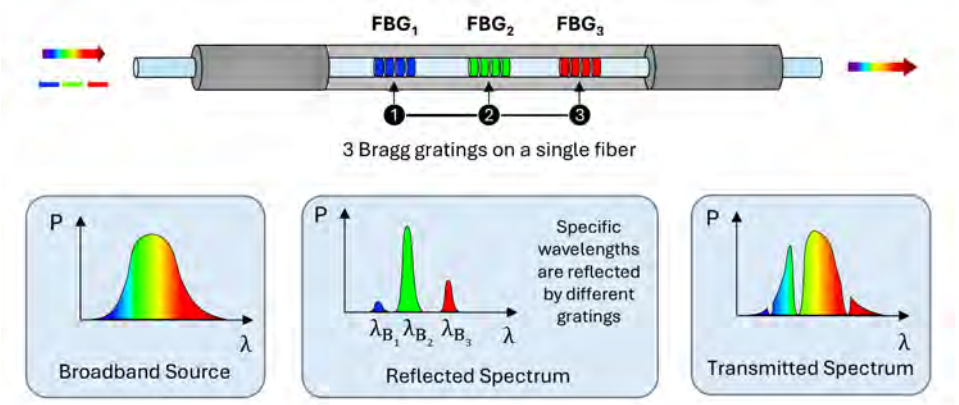

Figure 3.7: FBG array: multiple Fiber Bragg Gratings inscribed along a single optical fiber. Each grating reflects a narrow spectral band centered at its characteristic Bragg wavelength ($\lambda_{B_1}, \lambda_{B_2}\lambda_{B_3}$), while transmitting the remaining spectral components. When the fiber is illuminated by a broadband optical source, the reflected spectrum consists of discrete peaks corresponding to the individual gratings, and the transmitted spectrum shows complementary notches at those wavelengths. This principle enables multi-point sensing with a single interrogation channel.

This spectral shift constitutes the fundamental transduction mechanism of FBG sensors and underpins their application in structural health monitoring, biomedical thermometry, and other fields where precise, real-time sensing is required. Under small perturbations, the total wavelength shift caused by strain and temperature disturbances, can be written as:

$$\Delta\lambda_{\mathrm{B}} = \lambda_{\mathrm{B}}[(1 - P_e\varepsilon + (\alpha + \xi)\Delta\mathrm{T}] \tag{3.2}$$

where ε is axial strain applied to the fiber, ΔT temperature change, P_e the effective phopto-elastic coefficient of the fiber core material, α the axial thermal expansion of silica, and ξ the thermo-optic coefficient. For a silica fiber, the axial thermal expansion is $5 \cdot 10^{-7}\,\mathrm{K}^{-1}$ and the thermo-optic coefficient is $7 \cdot 10^{-6}\,\mathrm{K}^{-1}$. The strain term can be expanded through the stress-optic tensor:

$$P_e = \frac{n_{\mathrm{eff}}^2}{2}[\mathrm{P}_{12} - \nu(\mathrm{P}_{11} + \mathrm{P}_{12})] \tag{3.3}$$

with ν the core Poisson's ratio. For silica core fiber, n_{eff} is approximately 1.46, $\mathrm{P}_{11} = 0.113$, $\mathrm{P}_{12} = 0.252$, which gives the value of $P_e = 0.22$ [109]. These standard relations underlie both cross-sensitivity treatment and calibration procedures. Typical sensitivities around 1550 nm are $\sim 1.2\mathrm{pm}/\mu\varepsilon$ and $\sim 10 - 13\mathrm{pm}/^{\circ}\mathrm{C}$. Thus, the Bragg wavelenght change gives a direct measure of strain and/or temperature.

In our esperimental exploration, 2 arrays of 7 FBGs (Technica) and 2 arrays of 10 FBGs (AtGrating) were adopted. These arrays have a grating length of 1 mm and edge-to-edge distance between gratings of 2 mm, for a total sensing length of 19 mm and 28 mm, respectively (Figure 3.9(a)). All the arrays were fabricated by femtosecond point-by-point writing technology, in single mode optical fibers having an acrylate coating and an outer diameter of 250 µm.

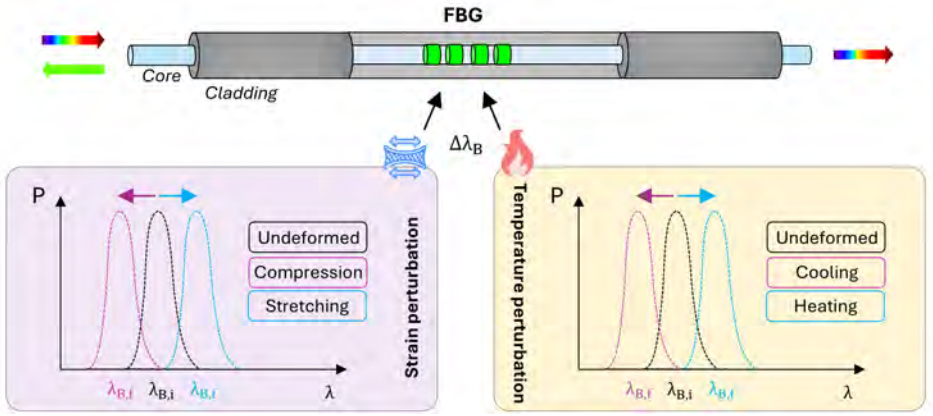

Figure 3.8: Schematic representation of the effect of external perturbations on the Bragg wavelength of a Fiber Bragg Grating. Mechanical strain (left) alters the grating period by stretching or compressing the fiber, while thermal perturbations (right) modify both the grating period and the effective refractive index of the core. In both cases, these changes result in measurable shifts of the Bragg wavelength, illustrated by the displacement of the corresponding reflection spectra.

Figure 3.9(b) shows the real FBG sensors employed. In the framework of thermal ablation experiments, the objective was to exploit FBG exclusively as temperature sensors, avoiding cross-sensitivity to strain. Since the Bragg wavelength shift intrinsically depends on both temperature and mechanical deformation, it was necessary to adopt a configuration that effectively decoupled the strain contribution. To this end, the sensing fibers were mounted using magnetic disk holders, which ensured that the gratings remained in a strain-free configuration throughout the experiments (see Section 3.3). In this way, the spectral shift of the reflected peak could be directly interpreted as a reliable indicator of local temperature variations, free from artifacts induced by residual mechanical stress or bending of the fiber.

Interrogation of FBGs in our experiments was carried out using a dedicated optical interrogator, the si255 Hyperion Platform, using a sample frequency of 1000 Hz, which scans the reflected spectrum through a broadband light source analyzed by an optical spectrometer. The peak wavelength of the reflection band is continuously tracked, providing real-time information about the local thermal state of the tissue sample.

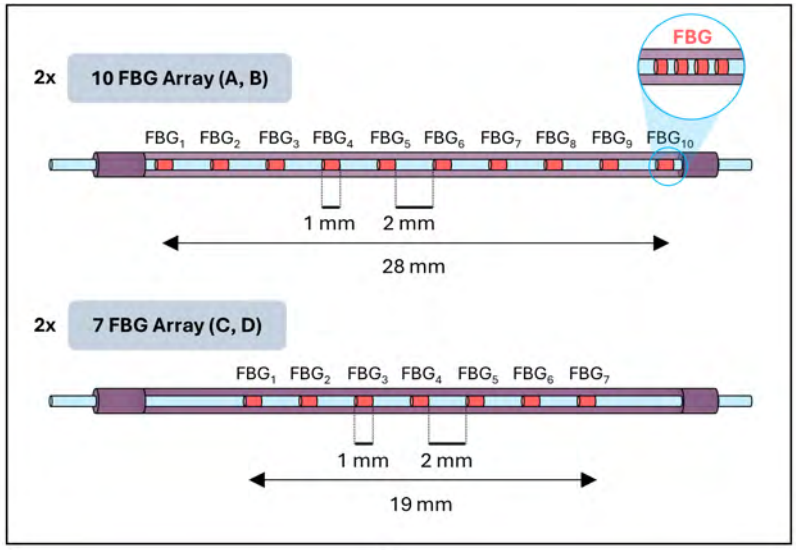

(a)

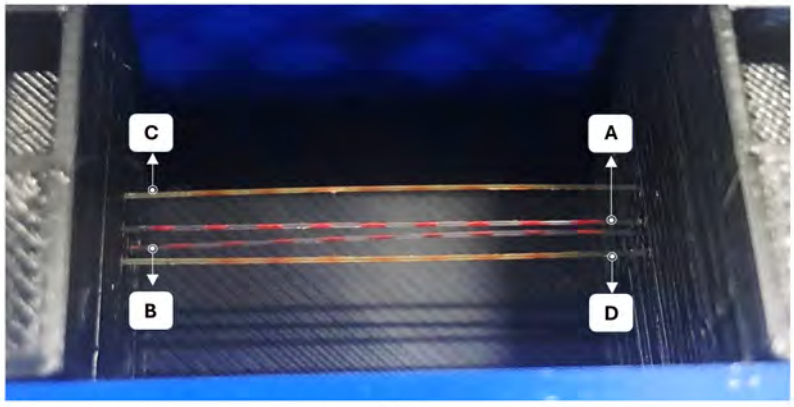

(b)

Figure 3.9: (a) Schematic layout of the two types of FBG arrays used in the experiments: two arrays composed of 10 FBGs (AtGrating) and two arrays composed of 7 FBGs (Technica). (b) Picture of the actual FBG arrays positioned inside the custom PLA holder, showing the placement of the four sensing lines (A, B, C, D) used for temperature monitoring during laser ablation experiments.

3.3 Integrated Experimental Setup

The final configuration of the experimental apparatus combines all the aforementioned components into a single, integrated system. The custom 3D-printed holder, realized via FDM technology in PLA, provided the mechanical frame for both the optical sensors and the laser applicator, ensuring precise and repeatable alignment. To guarantee stable positioning of the sensing fibers inside the holder and to achieve a strain-free configuration, small magnetic disks were employed to gently secure each FBG array without inducing axial tension or unwanted deformation. Within this structure, four FBG arrays were embedded, each composed of multiplexed gratings inscribed at distinct Bragg wavelengths, enabling simultaneous and spatially distributed temperature monitoring during laser irradiation. The FBGs were connected to a dedicated optical interrogator (si255 Hyperion Platform), which scans the reflected spectrum using a broadband light source and an integrated optical spectrometer, operating at a sampling frequency of 1000 Hz. The sensor outputs were transmitted to a personal computer running the ENLIGHT software suite, where the spectral data were displayed and recorded in real time. The ENLIGHT software provided continuous tracking of the reflected spectra, automatic peak detection, and data logging for subsequent processing. Inside the holder, tissue-mimicking phantoms were prepared and positioned to test the laser ablation mechanism under controlled conditions. The preparation of these phantoms and the detailed experimental protocols employed in both *in vitro* and *ex vivo* campaigns are presented in Chapter 4. Energy delivery was provided by a Nd:YAG laser generator (Smart DEKA, Florence, Italy), operating at a wavelength of 1064 nm in continuous-wave (CW) mode. The optical delivery fiber was a bare quartz fiber (Asclepion Laser Technologies) with a numerical aperture of 0.22 and a core diameter of 300 µm. The irradiation protocol consisted of a laser power of 3 W and a delivery time of 2 min for each experiment, parameters selected to produce measurable thermal gradients while avoiding excessive carbonization of the phantom material. All laser operations were conducted in compliance with safety regulations. Operators wore appropriate personal protective equipment, including certified laser-safety goggles, to prevent ocular exposure to near-infrared radiation.

To sum up, the complete setup, in Figure 3.10, comprises: the laser generator, optical delivery system, custom holder with integrated FBGs, interrogator platform, acquisition computer, and software suite. This setup constitutes a versatile and reproducible platform for investigating the thermal dynamics of laser ablation.

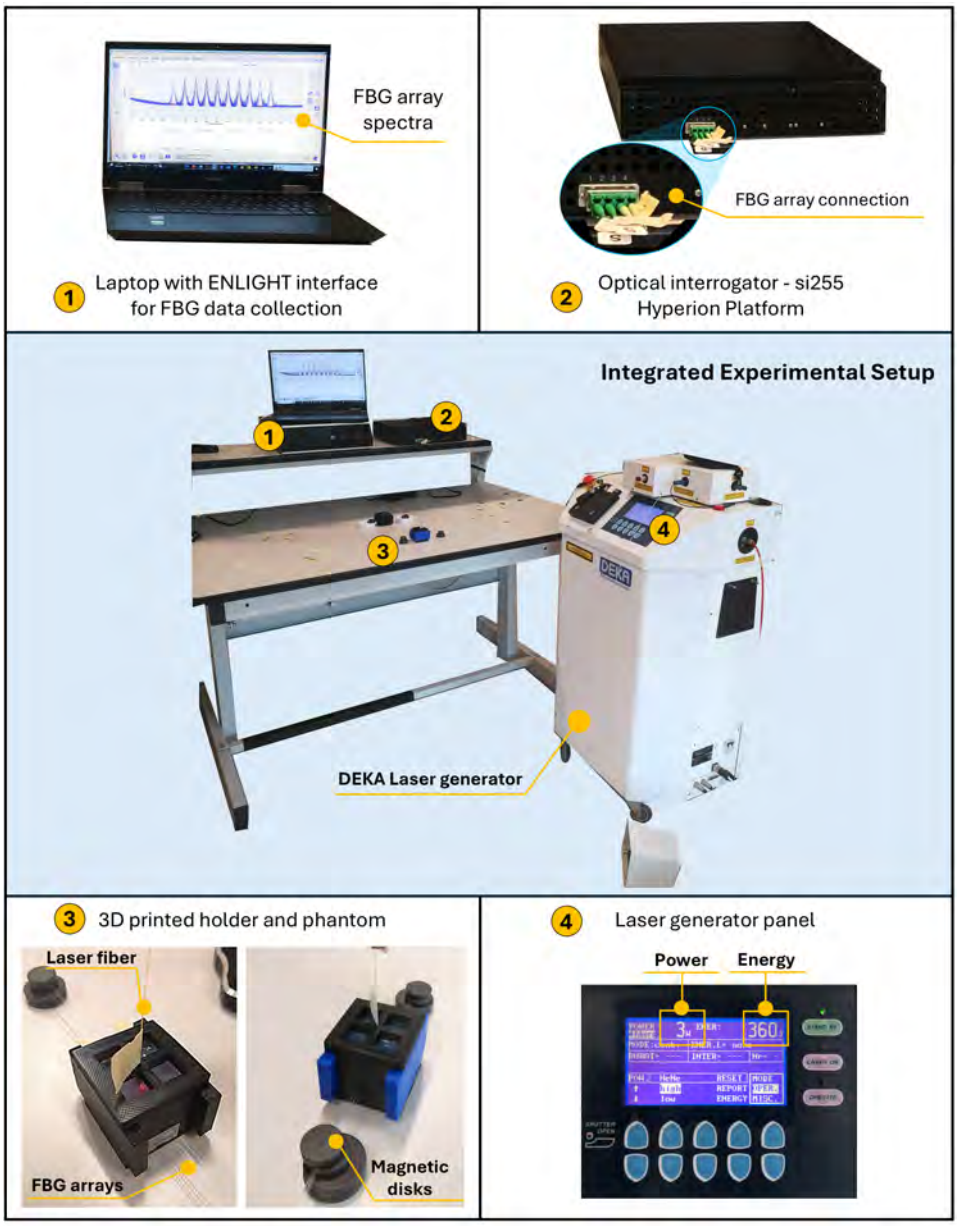

Figure 3.10: Integrated experimental setup used for the laser ablation investigations. The system comprises: (1) a laptop running the ENLIGHT software suite for real-time visualization and recording of the reflected FBG spectra; (2) the si255 Hyperion optical interrogator connected to the four multiplexed FBG arrays; (3) the custom FDM-printed PLA holder housing the tissue-mimicking phantom, the laser applicator, and the strain-free mounted FBG sensors secured using magnetic disks; and (4) Nd:YAG Smart DEKA laser generator with the associated optical delivery fiber and laser generator panel. Together, these components form a fully integrated and reproducible platform that enables precise laser energy delivery (3 W, 2 min CW protocol) and high-resolution temperature mapping during *in vitro* and *ex vivo* ablation experiments.

4

In vitro - Ex vivo Laser Ablation Experiments

Building on the clinical background and the experimental platform detailed in Chapter 3, this section focuses on the *in vitro* campaign designed to isolate and quantify the fundamental photothermal mechanisms of laser ablation under tightly controlled conditions, including both baseline (blank) experiments and NP-mediated ablation tests using gold nanoparticles, before progressing toward *ex vivo* experiments in animal liver. Thus, we started from tissue-mimicking phantoms to remove confounders present in biological tissue, e.g., perfusion, heterogeneous optics, anisotropy etc, ensure high repeatability and precise co-registration of the laser applicator with dense FBG thermometry, and establish a benchmark dataset for calibrating the coupled optical–thermal models.

4.1 *In vitro* Experiments

For the *in vitro* experiments, a tissue-mimicking phantom based on agarose gel was selected as the most suitable medium. Agarose is a natural polysaccharide derived from red algae, composed of alternating units of agarobiose, a disaccharide formed by D-galactose and 3,6-anhydro-L-galactose. When dissolved in hot water and subsequently cooled, agarose forms a semi-solid hydrogel through a reversible gelation process driven by hydrogen bonding. The resulting matrix consists of an interconnected network of polymeric chains that trap water molecules, giving the material optical and thermal properties closely resembling those of soft biological tissues. This structural similarity makes agarose an ideal choice for phantom fabrication in photothermal and laser-tissue interaction studies. Its optical scattering coefficient, refractive index ($\sim$ 1.33 – 1.34), and high water content enable realistic modeling of light transport and absorption in the NIR region, particularly around 1064 nm, the wavelength commonly employed in medical laser ablation. Moreover, agarose gels are chemically inert, inexpensive, easy to mold, and reproducible, which allows creating homogeneous samples of controlled geometry and composition. In the context of this work, agarose served as the base matrix for the development of tissue phantoms used to investigate the laser-induced thermal response under well-defined conditions. The fabrication process was designed to

achieve a homogeneous, optically stable, and mechanically consistent gel, suitable for accommodating both the laser delivery fiber and the FBG temperature sensors in the predefined positions within the 3D-printed holder.

The phantoms were prepared by dissolving agarose powder (ZellBio GmbH)(Sigma-Aldrich, analytical grade, gel strength $> 1200\,\mathrm{g\,cm^{-2}}$) in deionized water to achieve a concentration of 4 % by weight. The agarose-water mixture was gently heated on a magnetic stirrer hotplate up to approximately 250 °C for 30 min, under stirring at 400 rpm to ensure complete dissolution and prevent bubble formation. Once the homogeneous solution was obtained, the mixture was allowed to cool down to around 85 °C, reaching a viscosity suitable for casting while still avoiding premature gelation. At this stage, the solution was poured into the central chamber of the PLA holder where FBG sensors are already positioned in their respective channels and secured by the magnetic disks, as described in Section 3.3. The entire assembly was kept stationary during the gelation process to prevent any movement of the FBG fibers, which could otherwise alter their distance or induce strain in the gratings. Gelation occurred upon cooling to room temperature ($\sim$ 22 – 25 °C), resulting in transparent, mechanically stable hydrogels with uniform optical properties. The process typically required 1 h, after which the phantoms were fully solidified and ready for laser irradiation. The full agarose phantom formation protocol, as outlined above, is depicted in Figure 4.1.

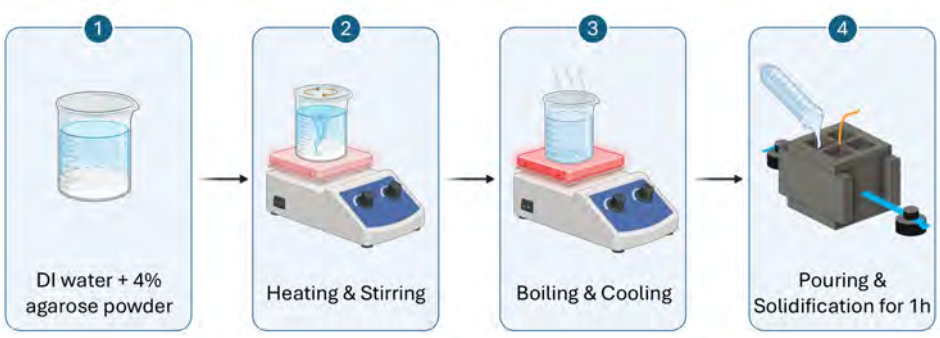

Figure 4.1: Illustration of the main steps involved in the preparation of agarose-based tissue-mimicking phantoms for *in vitro* laser ablation experiments. (1) The process begins with the dispersion of agarose powder in deionized water, (2) followed by gradual heating and magnetic stirring to obtain a clear and homogeneous solution. (3) Once complete dissolution is achieved, the solution is briefly boiled and then cooled to a casting temperature that preserves its fluidity. (4) The warm solution is subsequently poured into the custom 3D-printed PLA holder, previously equipped with the four FBGs arrays in the strain-free configuration thanks to the magnetic disks, where it solidifies into a stable hydrogel. This procedure ensures uniform optical properties, reproducible geometry, and consistent sensor positioning across all fabricated samples.

Each prepared phantom could be used for multiple irradiation cycles, provided that the laser exposure did not exceed the thermal damage threshold of the material, as prolonged heating above 80 °C can induce dehydration or local turbidity changes due to polymer network contraction. This preparation protocol ensured that each agarose phantom maintained consistent geometry and composition, allowing direct comparison among different experiments and ensuring high reproducibility of the thermal profiles recorded by the FBG sensors.

The agarose-only phantoms described above were fabricated to serve as blank models, providing a reliable reference baseline for subsequent experiments. These control samples, free of any absorbing or scattering additives, were used to evaluate the intrinsic photothermal response of the agarose matrix under identical irradiation conditions. Establishing such blank reference models is essential to isolate the thermal contribution solely due to the laser–medium interaction, enabling a direct and quantitative comparison with the temperature maps further obtained from nanoparticle-enriched phantoms. This approach ensures that any enhancement in thermal distribution or heating rate can be unambiguously attributed to the nanoparticle presence. In addition, the pure agarose phantoms were also employed to evaluate the reproducibility and accuracy of the temperature measurements under different experiments. Specifically, this preliminary phase aimed to verify the necessity of using the custom 3D-printed PLA holder to ensure consistent positioning of both the FBG sensors and the laser fiber during irradiation. To this end, identical ablation tests were carried out on multiple phantoms to assess its impact on measurement stability [110]. Figure 4.2 reports the maximum temperature variations measured by the main significant FBGs measured with the PLA holder (solid box) and without the PLA holder (dotted box).

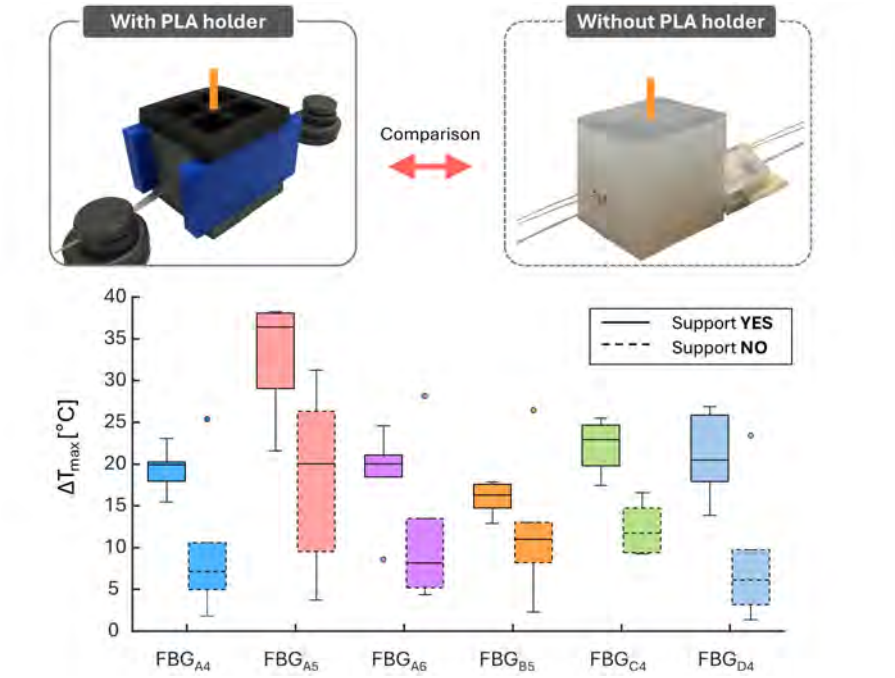

Figure 4.2: Comparison between laser ablation experiments performed with and without the custom PLA holder. The upper panels show the experimental configurations: (left) setup with the 3D-printed PLA holder ensuring fixed alignment of the laser fiber and FBG sensors; (right) setup without mechanical support. The lower panel reports the boxplot of the maximum temperature variations (ΔT_{max}) recorded by FBG_{A4}, FBG_{A5}, FBG_{A6}, FBG_{B5}, FBG_{C4}, and FBG_{D4} under both conditions, with PLA support (solid boxes) and without PLA support (dotted boxes). In each box, the central line represents the median, the lower and upper edges indicate the 25^{th} and 75^{th} percentiles, and the whiskers extend from the minimum to the maximum values, excluding outliers.

Overall, the data clearly show that the temperatures reached at the end of the laser ablation process are systematically higher and more consistent when the PLA holder is used. In all cases, the interquartile ranges (IQRs) obtained without the holder are significantly wider than those measured with the holder, indicating greater variability in temperature readings due to misalignment of the sensing fibers. For instance, for FBG_{A5}, the IQR decreases from without the support (9.5 – 26.3 °C) to with the support (29.0 – 38.1 °C), demonstrating a marked improvement in repeatability. The results, in terms of median values and IQRs for each FBG considered, are summarized in Table 4.1.

The experiments conducted without the PLA fixture revealed the inherent limitations of manual sensor placement in agarose gels. Due to the gelatinous and deformable nature of the medium, the insertion of the optical fibers using carbon needles did not guarantee precise or repeatable positioning; their locations varied across samples, introducing measurement uncertainty that was also operator-dependent. Conversely, the adoption of the custom PLA holder ensured stable alignment and fixed geometry between the FBG arrays and the laser applicator, significantly improving both accuracy and reproducibility. Thus, these results highlight higher temperature consistency and reduced variability when the PLA holder is used, confirming its crucial role in achieving reproducible sensor positioning and reliable thermal measurements.

Considering these preliminary outcomes, all subsequent experimental campaigns, both *in vitro* and *ex vivo*, were conducted using the custom PLA support, which proved essential for obtaining reliable thermal data and minimizing positioning-induced errors in the FBG temperature readings.

	Median [°C]	IQR [°C]	Median [°C]	IQR [°C]
FBG_{A4}	20.0	18.0-20.0	7.1	5.0-10.6
FBG_{A5}	36.4	29.0-38.1	20.0	9.5-26.3
FBG_{A6}	20.1	18.5-21.1	8.1	5.2-13.5
FBG_{B5}	16.3	14.8-17.6	11.0	8.2-13.0
FBG_{C4}	23.0	19.8-24.7	11.7	9.4-14.7
FBG_{D4}	20.5	17.9-25.9	6.1	3.2-9.8

Table 4.1: Median temperature values and associated interquartile ranges for FBG_{A4}, FBG_{A5}, FBG_{A6}, FBG_{B5}, FBG_{C4}, and FBG_{D4} sensors, reported for both experimental conditions: measurements performed with the PLA holder (light-pink columns) and those obtained without the holder (light-green columns).

4.1.1 Nanoparticle-mediated laser ablation

Following the preliminary experiments performed on pure agarose phantoms, a subsequent set of *in vitro* tests was conducted to investigate the influence of gold nanoparticles on the photothermal efficiency of laser ablation within the NIR window. The objective was to assess how embedding gold-based nanostructures within the agarose matrix could locally enhance optical absorption and energy-to-heat conversion, thereby increasing the selectivity and controllability of the ablation process.

These *in vitro* nanoparticle-mediated investigations also serve as a foundational step for the tumor ablation research line (see Section 2.2), providing quantitative insight into how nanostructure–light interactions can be exploited to improve the therapeutic precision and efficacy of nanoparticle-assisted laser treatments.

Previous studies have shown that anisotropic gold-based nanostructures exhibit superior photothermal performance compared to spherical counterparts, due to the excitation of localized surface plasmon resonances that can be spectrally tuned to the laser emission wavelength [85, 111].

In this work, two main classes of nanoparticles were employed: gold nanocages (NC_1, NC_2, NC_3) and gold nanorods (NR). The nanocages were synthesized via galvanic replacement[1] of silver nanocubes (edge $\simeq 35 \pm 6$ nm), resulting in hollow, porous architectures with tunable wall thickness and plasmonic properties dependent on the degree of gold substitution. Increasing the $HAuCl_4$ concentration during synthesis led to progressive pore enlargement and a red-shift in the LSPR peak, enabling resonance tuning across the NIR spectrum. Gold nanorods were synthesized using a seed-mediated growth method involving CTAB-stabilized gold seeds and a controlled growth solution containing Au, Ag, and reductant precursors [113].

After synthesis, the nanoparticles were subsequently characterized using Transmission Electron Microscopy[2] (TEM), Nanoparticle Tracking Analysis[3] (NTA), and Ultraviolet–Visible–Near-Infrared[4] (UV–Vis–NIR) spectroscopy.

Specifically, NC_1, NC_2, NC_3 and NR exhibit peak absorption wavelength at 709.5, 816.9, 1140 and 1105 nm, respectively. This systematic variation allowed the investigation of how the optical response affects photothermal conversion efficiency under 1064 nm laser irradiation, chosen to match the operating wavelength of the ablation source.

In detail:

- NC_1 exhibited a hydrodynamic diameter of 85.3 ± 1.0 nm and an average edge length of 46.4 ± 4.8 nm, with an LSPR centered at 709.5 nm and a molar extinction coefficient of $1.9 \cdot 10^9\ \mathrm{mol}^{-1}\,\mathrm{cm}^{-1}$ at 1064 nm.

- NC_2 showed a narrower size distribution, with a hydrodynamic diameter of 77.2 ± 0.7 nm and an edge of 44.9 ± 5.3 nm. Their main plasmon resonance, centered at 816.9 nm, yielded an extinction coefficient of $2.26 \cdot 10^9\ \mathrm{mol}^{-1}\,\mathrm{cm}^{-1}$ at 1064 nm.

- NC_3, characterized by smaller cavities (hydrodynamic diameter 72.9 ± 2.9 nm; edge 42.5 ± 6.6 nm), displayed a red-shifted resonance at 1140 nm and a molar extinction coefficient of $3.24 \cdot 10^9\ \mathrm{mol}^{-1}\,\mathrm{cm}^{-1}$ at 1064 nm, with a secondary visible peak around 514 nm attributed to residual metallic fragments.

[1] Galvanic replacement is a redox-driven synthesis process in which a less noble metal template is partially dissolved and replaced by a more noble metal ion in solution, leading to the formation of hollow or porous nanostructures [112]

[2] Transmission Electron Microscopy (TEM) provides high-resolution imaging of nanoparticles by transmitting an electron beam through the sample, allowing visualization of size, shape, and morphology [114]

[3] Nanoparticle Tracking Analysis (NTA) enables the determination of the sample concentration, expressed as NPs/mL, and provides the size distribution of the nanoparticles. [115].

[4] Ultraviolet–Visible–Near-Infrared (UV–Vis–NIR) spectroscopy measures the optical absorption of nanoparticles across a broad wavelength range, enabling analysis of their plasmonic properties and concentration [116].

- NR with a hydrodynamic diameter of 62.2 ± 5.5 nm, exhibit an average length of 63.3 ± 8.5 nm, a width of 9.9 ± 0.8 nm, and an aspect ratio of 6.4 ± 0.7. Their longitudinal plasmon resonance is centered at 1105 nm, close to the laser wavelength, with a molar extinction coefficient of $4.09 \cdot 10^9\ \mathrm{mol}^{-1}\,\mathrm{cm}^{-1}$ at 1064 nm.

Figure 4.3 provides a combined visualization of these properties, reporting for each nanoparticle type the hydrodynamic size distribution obtained via NTA alongside the corresponding TEM images, which confirm morphology, uniformity, and overall structural integrity.

The photothermal conversion efficiency (PCE) η, quantifies the capability of plasmonic nanoparticles to convert absorbed optical energy into heat under laser irradiation. In this study, the PCE was determined following the classical formulation reported in the literature [117]:

$$\eta = \frac{hS(\Delta \mathrm{T}_{\mathrm{max,NPs}} - Q_s)}{\mathrm{P}(1 - 10^{-A_\lambda})} \tag{4.1}$$

where, h is the heat transfer coefficient, S is the surface area of the sensing volume, P is the incident laser power, A_λ is the optical absorbance of the nanoparticle colloid at the laser wavelength λ, Q_s is the heat dissipated by the agarose medium, and $\Delta \mathrm{T}_{\mathrm{max,NPs}}$ is the maximum temperature rise measured by the FBG sensor during irradiation (refers to Figure 4.9). The photothermal conversion efficiency was quantified from the nanoparticle heating curves shown in Figure 4.4. All the details about the PCE calculation are provided in Appendix. Moreover, the Vis–NIR characterizations displayed in the left panels of Figure 4.4 highlight the LSPR peaks of each nanoparticle type, providing direct insight into their wavelength-dependent optical absorption.

As summarized in Table 4.2, NC_2 demonstrated the highest η, confirming it as the most effective photothermal agent among the tested formulations. Interestingly, both NC_3 and NR exhibited lower efficiencies despite presenting stronger optical absorption at 1064 nm. For NC_3, this reduced performance is likely associated with structural fragility, as partial collapse or incomplete galvanic replacement can impair the ability of the nanocages to sustain efficient heat generation (refers to the TEM picture of Figure 4.3.(c)). In contrast, although the nanorods showed a lower η than NC_2, they produced the largest temperature rise overall, indicating substantial heat output. This behavior suggests that, for NR, the enhanced absorption at the excitation wavelength does not directly translate into correspondingly higher conversion efficiency.

This collection of nanostructures enabled a comparative investigation of how morphology and plasmonic resonance tuning influence thermal conversion under identical irradiation conditions. For completeness, all methodological details concerning the synthesis, physicochemical characterization, morphological characterization and stability analysis are reported in Appendix.

Returning to the experiments, for each nanoparticles, NPs concentration of $3 \cdot 10^{10}$ NP/mL was homogeneously mixed into the agarose solution during the cooling phase, prior to gelation, to guarantee uniform nanoparticle distribution within the phantom volume.

The mixture was gently agitated to promote uniform dispersion without introducing air bubbles or inducing nanoparticle aggregation. The warm agarose-NPs

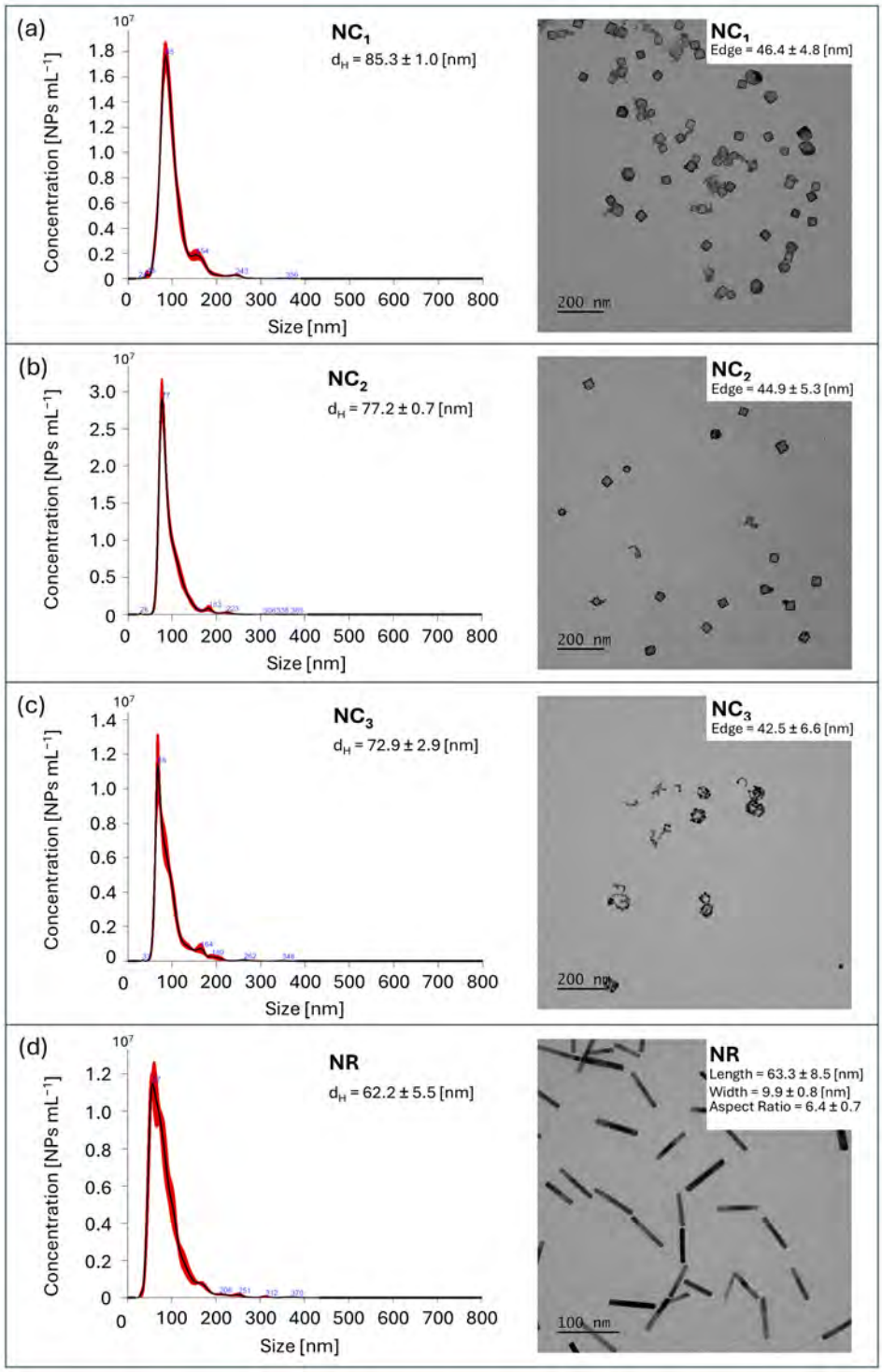

Figure 4.3: Nanoparticle morphology and size distribution for NC_1 (a), NC_2 (b), NC_3 (c) and NR (d). For each sample, the NTA-derived size distribution (left) is shown alongside the corresponding TEM images (right). d_h is the hydrodynamic diameter.

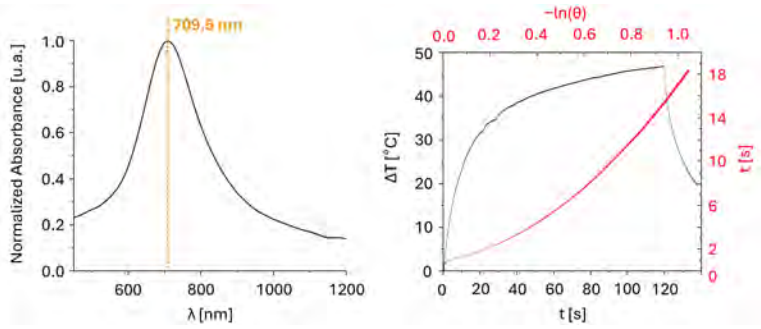

(a) NC_1

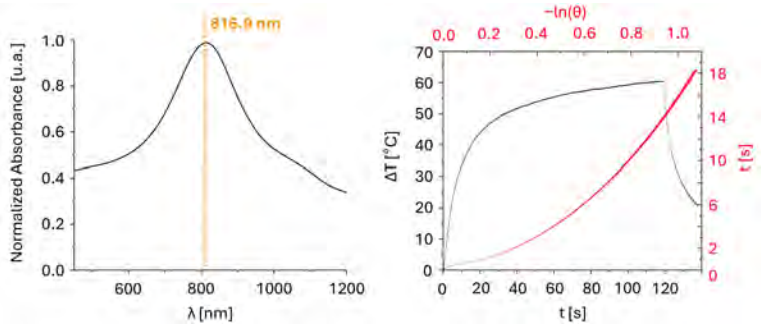

(b) NC_2

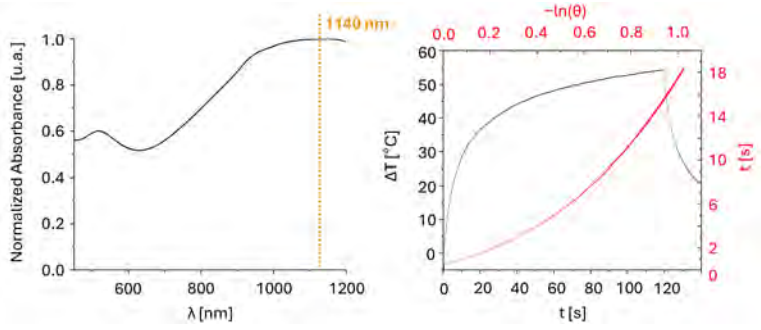

(c) NC_3

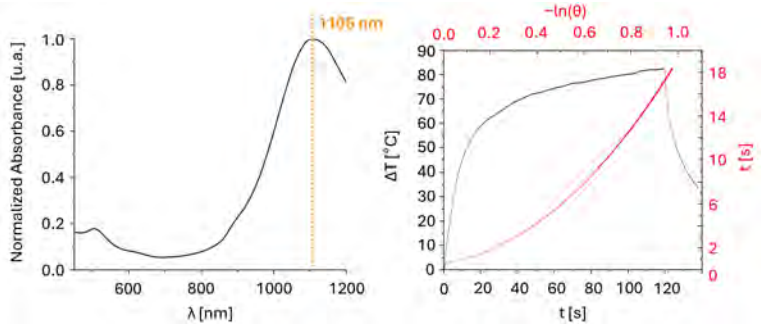

(d) NR

Figure 4.4: Vis-NIR characterization and PCE calculation of NC_1 (a), NC_2 (b), NC_3 (c), NR (d).

NPs	λ_{max}[nm]	ΔT_{max} [°C]	η [%]
NC_1	709.5	46.8	22.4
NC_2	816.9	60.4	35.0
NC_3	1140	54.4	18.7
NR	1105	82.6	31.5

Table 4.2: Photothermal performance of the four nanoparticle formulations investigated in this study. The table reports the wavelength of maximum optical absorption λ_{max}[nm], corresponding to the localized surface plasmon resonance of each structure, together with the calculated PCE η and the maximum temperature rise ΔT_{max} [°C] recorded during laser irradiation at 1064 nm. These metrics collectively highlight the distinct photothermal behaviors of the nanocages and nanorods, emphasizing the superior efficiency of NC_2 and the notably high temperature elevation achieved by NR.

solution was then poured into the custom PLA holder following the same procedure described for pure agarose phantoms. The agarose-NPs phantom formation protocol is schematically illustrated in Figure 4.5.

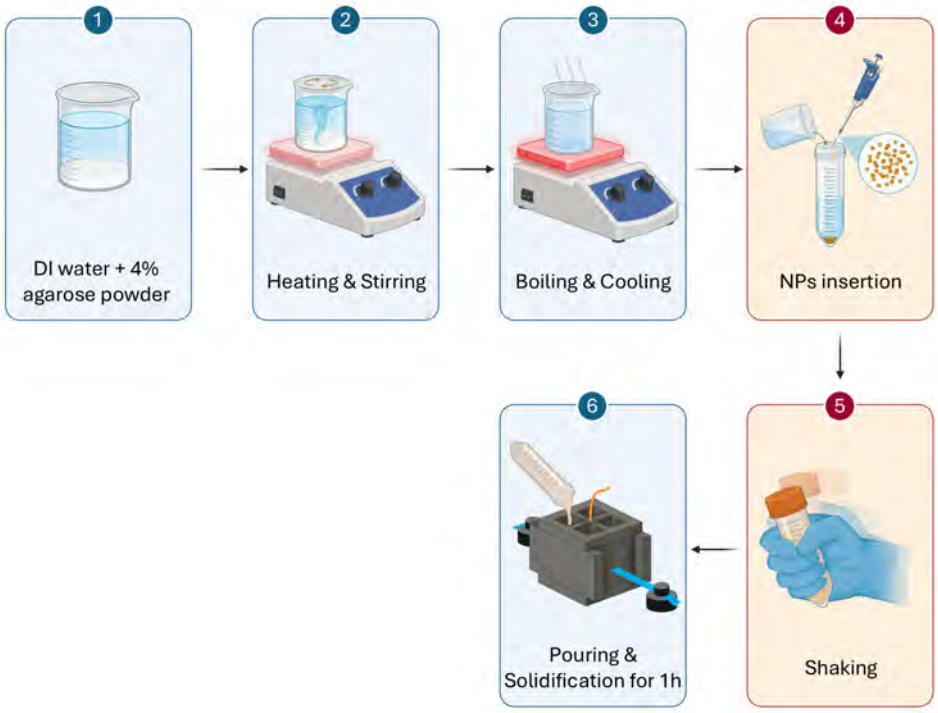

Figure 4.5: Schematic workflow for the preparation of agarose-based phantoms incorporating gold nanoparticles (AuNPs). (1) Agarose powder is dissolved in deionized water to obtain a 4 % w/v suspension. (2) The mixture is heated under magnetic stirring until complete dissolution and (3) subsequently cooled to 80 °C to reach a suitable viscosity for mixing. (4) At this stage, the nanoparticle suspension, previously synthesized and characterized, is introduced into the warm agarose solution. (5) Gentle manual shaking ensures homogeneous dispersion of the nanoparticles within the matrix without inducing aggregation or bubble formation. (6) The resulting agarose-nanoparticle mixture is poured into the custom 3D-printed PLA holder containing the FBG sensors and the laser applicator, where it solidifies at room temperature within approximately one hour, forming a uniform tissue-mimicking phantom with AuNPs.

4.1.2 Results

Part of the experimental results discussed in this section have been previously reported in [118].

Before presenting the experimental results, a reference schematic of the sensing configuration is provided in Figure 4.6 to clarify the spatial arrangement of the FBG arrays and the corresponding color code adopted throughout this section. Four multiplexed FBG arrays A, B, C, and D were inserted into dedicated grooves of the holder and positioned within the sample at a controlled inter-array separation of 2 mm. The right-hand panel of Figure 4.6 provides the final embedding configuration within the phantom volume, showing the relative depth and orientation of each array with respect to the laser fiber. The lower panel reports the complete color legend used to identify each FBG along the arrays. This standardized color coding is consistently applied across all temperature–time plots, and ablation profiles presented in the following sections, ensuring an accurate and intuitive identification of the spatial origin of every plotted temperature trace.

The experimental campaigns were carried out under five distinct conditions: a reference configuration without nanoparticles (NO NP) and four NP-mediated configurations, involving NC_1, NC_2, NC_3, and NR. Across all tests, the operating parameters of the laser system were kept constant, with the output power set to 3 W and the irradiation time fixed at 2 min. For each configuration, multiple repetitions were performed on agarose-based phantoms, yielding 11 independent trials for each NP type. To provide an overview of the typical thermal response captured by the sensing system, Figure 4.7 reports representative ΔT profiles recorded on an agarose-only phantom. When the laser is activated at t = 0 s, all FBGs experience a rapid temperature increase, with the steepest rise occurring within the first few seconds of irradiation. This marks the beginning of the *heating phase*, during which the temperature continues to increase gradually as the medium absorbs laser energy. The peak temperature is reached near the end of the irradiation period, at t = 120 s. Therefore, the laser is switched off following the predefined energy protocol, initiating the *cooling phase*. In this stage, the recorded temperature decreases progressively as heat dissipates within the surrounding material. Data acquisition was extended beyond laser switch-off to adequately capture the thermal decay and characterize the full cooling dynamics. This general behavior: rapid early heating, progressive temperature rise during continuous irradiation, and a subsequent cooling trend, is consistently observed across all configurations and forms the reference pattern against which the NP-mediated experiments are compared in the following sections.

Given the large amount of collected data, the temperature variations (ΔT) with respect to the environmental temperature are presented as average temporal profiles computed for each individual FBG by averaging its output across all trials performed under identical NP conditions. These averaged ΔT trends are summarized in Figure 4.8, arranged in a matrix-like structure. In this representation, columns correspond to the four FBG arrays (A, B, C, D), while rows correspond to the five investigated configurations (NO NP, NC_1, NC_2, NC_3, and NR). Each cell of the matrix contains a set of ΔT curves, one for each FBG belonging to the corresponding array. The traces are plotted using the same color code defined in Figure 4.6, which enables an immediate visual correspondence between each curve and its sensing location. As expected, the highest temperature increments were consistently measured by array A, which was positioned closest to the laser tip.

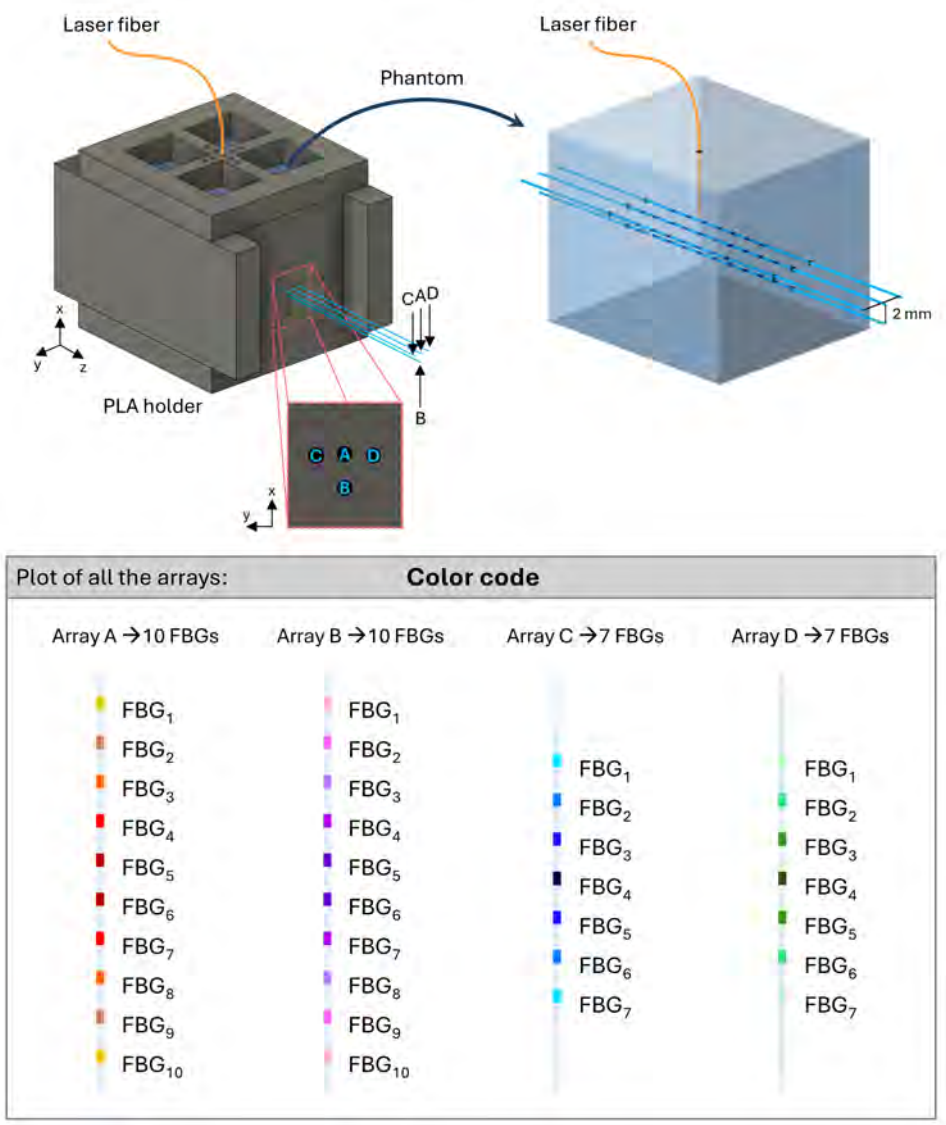

Figure 4.6: Schematic representation of the experimental sensing configuration. Top left: 3D-printed PLA holder with dedicated channels for hosting the FBG arrays and the laser fiber. Top right: reconstruction of the FBG array positioning within the sample, with 2 mm spacing between adjacent arrays. Bottom: Color code for all FBGs belonging to arrays A–D, used consistently across all subsequent plots to identify individual sensing points.

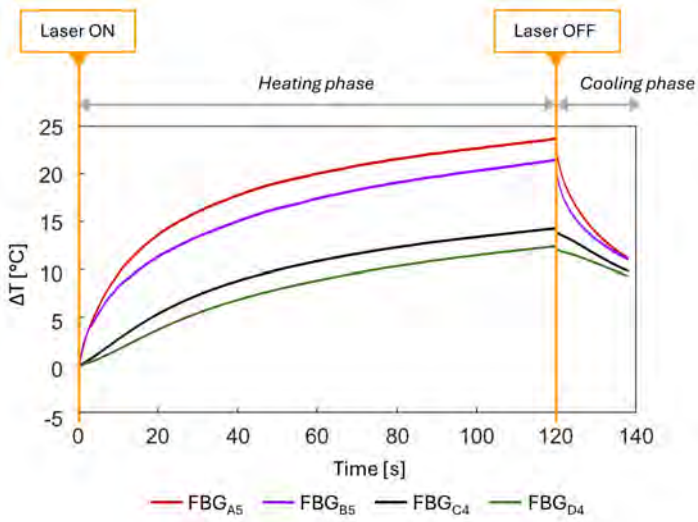

Figure 4.7: Representative ΔT profiles acquired on an agarose-only phantom of FBG_{A5}, FBG_{B5}, FBG_{C4}, FBG_{D4}. The curves illustrate the typical thermal response measured by the FBGs during laser irradiation. When the laser is switched on at t = 0 s, a rapid temperature increase is observed, followed by a gradual rise throughout the heating phase. At t = 120 s, the laser is turned off, marking the beginning of the cooling phase, during which the recorded temperature decreases as heat dissipates within the medium. These trends exemplify the characteristic behavior consistently observed across all experiments.

Within this array, the FBG_{A5}, located nearest to the applicator recorded the largest ΔT values. A clear enhancement of the thermal response was observed in all NP-mediated configurations. In the absence of NPs, the maximum temperature ΔT_{max} rise recorded by array A is 23.7 °C, whereas the introduction of NPs resulted in ΔT_{max} values spanning from 46.9 °C to 82.6 °C, depending on the NP type. A progressive increase in ΔT was observed when comparing NC_1, NC_2, and NC_3. This trend reflects the different optical absorption spectra of the nanocages: although they share the same structural class, their absorption maxima progressively shift toward the laser wavelength when moving from NC_1 to NC_3. The improved spectral overlap results in more efficient photon absorption and, consequently, enhanced photothermal conversion.

Despite NC_3 exhibiting an absorption peak closer to 1064 nm, its broader and less pronounced spectral profile likely limits the net photothermal gain, explaining why ΔT values for NC_2 and NC_3 remain comparable. The most significant temperature increases were obtained using NR. In this configuration, the measured ΔT_{max} values reached 82.6 °C, 69.9 °C, 41.0 °C, and 48.5 °C for arrays A, B, C, and D, respectively, substantially higher than those recorded for all other NP types. This behavior aligns with the strong and narrow absorption peak of NR, which is well aligned with the 1064 nm laser emission, resulting in particularly efficient photothermal conversion. To provide a clearer comparison of the photothermal performance of the different nanoparticle formulations, a specific focus was placed on the maximum temperature increases recorded at the sensing point closest to the laser source. Figure 4.9 summarizes the ΔT_{max} temporal trends for the four NP-configurations and for the reference condition without NP.

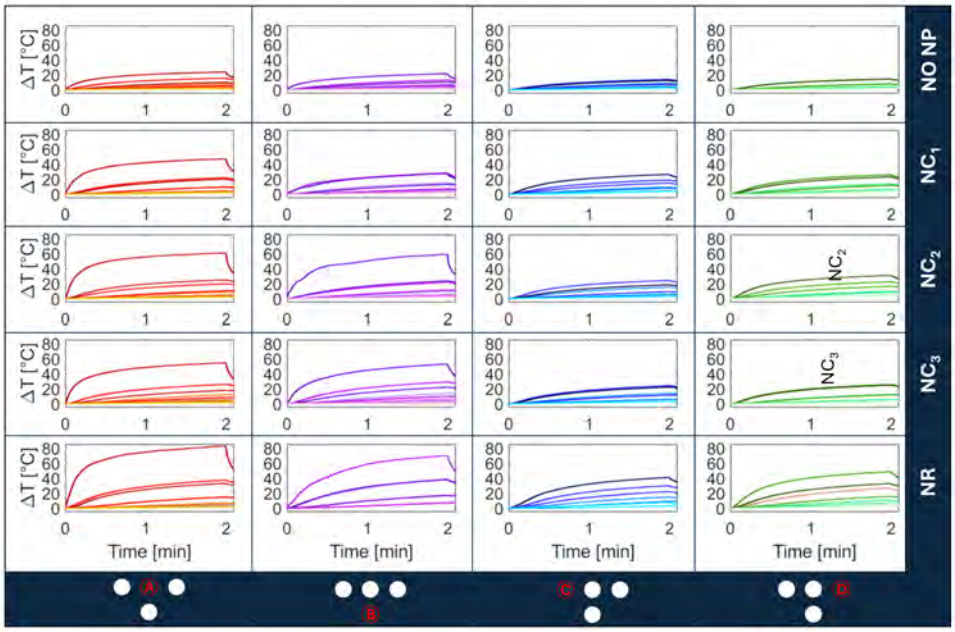

Figure 4.8: Matrix representation of the averaged temperature increments (ΔT) with respect to the environmental temperature recorded during laser ablation (2 min) across the five investigated configurations. Rows correspond to the tested conditions: reference configuration without nanoparticles (NO NP) and phantom with NPs: NC_1, NC_2, NC_3 and NR. Columns refer to the four FBG arrays (A–D). Each cell contains the average ΔT temporal profiles measured by the individual FBGs of the corresponding array, computed by averaging their signals across all repeated tests performed under identical experimental conditions.

All ΔT_{max} values shown in the figure correspond to FBG_{A5}, the element of array A located nearest to the laser applicator and therefore most representative of the peak thermal effect generated during irradiation. As expected, NR produced the largest temperature rise at this position, reaching ΔT_{max} of 82.6 °C. However, analysis of the photothermal conversion efficiency PCE η indicates that NC_2 exhibit the highest conversion efficiency, surpassing NR. This result can be understood by considering the PCE definition, which evaluates the heat released normalized to the absorbed optical energy. Although NR generated the largest absolute temperature increase, NC_2 produced more heat per unit of absorbed energy, thus achieving the highest PCE among all tested samples. Interestingly, NC_3, despite their stronger absorption at 1064 nm, did not exceed NC_2 in terms of heat generation at FBG_{A5}. As aforementioned, this reduced performance is likely related to the presence of damaged or partially collapsed NC_3 in the sample, as visible in the corresponding TEM image, which can compromise photothermal conversion efficiency by limiting the effective transformation of absorbed photons into heat (refers to TEM picture of Figure 4.3(c)). Finally, the nanocages NC_1 exhibited an intermediate PCE value. Although their absorption at 1064 nm is lower, they still produced a notable thermal rise at FBG_{A5}, indicating a non-negligible heat release relative to their absorption characteristics.

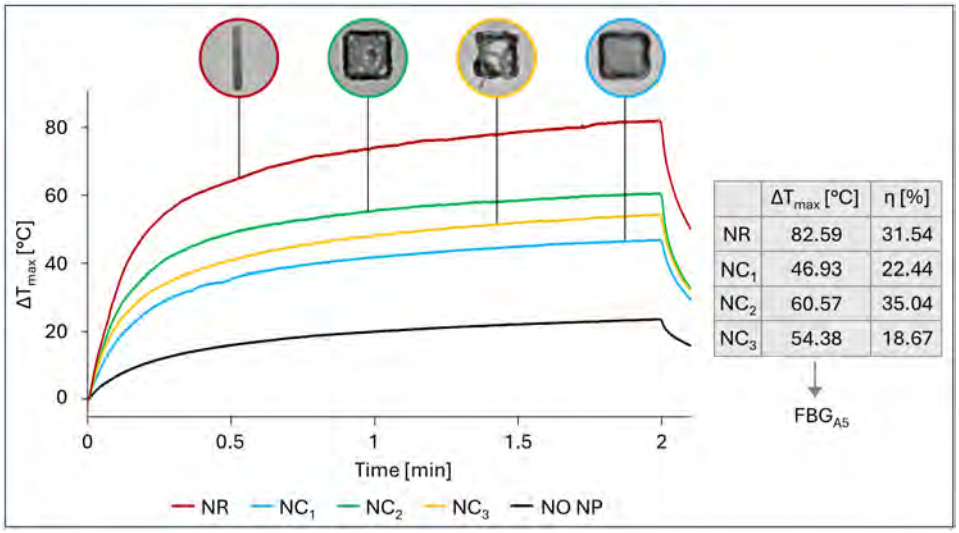

Figure 4.9: Comparison of maximum temperature variations ΔT_{max} recorded at FBG_{A5} for all nanoparticle configurations. Temporal trends of FBG_{A5} measured at the sensing point closest to the laser applicator FBG_{A5} for the four NP-mediated conditions (NR, NC_1, NC_2, NC_3) and the reference configuration without nanoparticles (NO NP). The curves highlight the markedly different photothermal responses induced by each NP formulation. The insets report representative TEM images of the corresponding nanoparticles, while the table summarizes ΔT_{max} values and the associated photothermal conversion efficiencies η.

4.2 *Ex vivo* Experiments

After the *in vitro* experimental campaigns on agarose-based phantoms, the next phase of this work focused on an *ex vivo* stage aimed at reproducing more realistic thermal and optical conditions of biological tissues. This step represents a natural progression of the study, bridging the controlled, reproducible environment of synthetic models with the structural and compositional complexity of real biological samples.

The experiments were conducted on porcine liver specimens. Unlike agarose phantoms, which provide homogeneous and optically stable conditions, *ex vivo* liver tissue exhibits intrinsic heterogeneity in optical absorption, scattering, and water content, as well as anisotropic heat conduction due to the vascular microarchitecture. These characteristics make the *ex vivo* model an essential intermediate step toward *in vivo* animal experimentation, allowing the assessment of the feasibility, precision and safety of laser ablation under conditions more representative of the clinical scenario. The outcomes of this campaign provided crucial insight into the translation of laser ablation protocols from simplified synthetic models to realistic biological substrates.

In this section, the application of the laser ablation setup, previously optimized *in vitro*, is extended to fresh *ex vivo* liver samples. An illustrative scheme of this preparation procedure is reported in Figure 4.10, documenting the sequence from whole-organ sectioning to final placement within the holder. Fresh porcine livers were procured and immediately processed by sectioning them into cubic portions

compatible with the dimensions of the custom 3D-printed PLA holder. The liver tissue block was manually positioned inside the central compartment of the holder, replacing the agarose phantom used in the *in vitro* configuration.

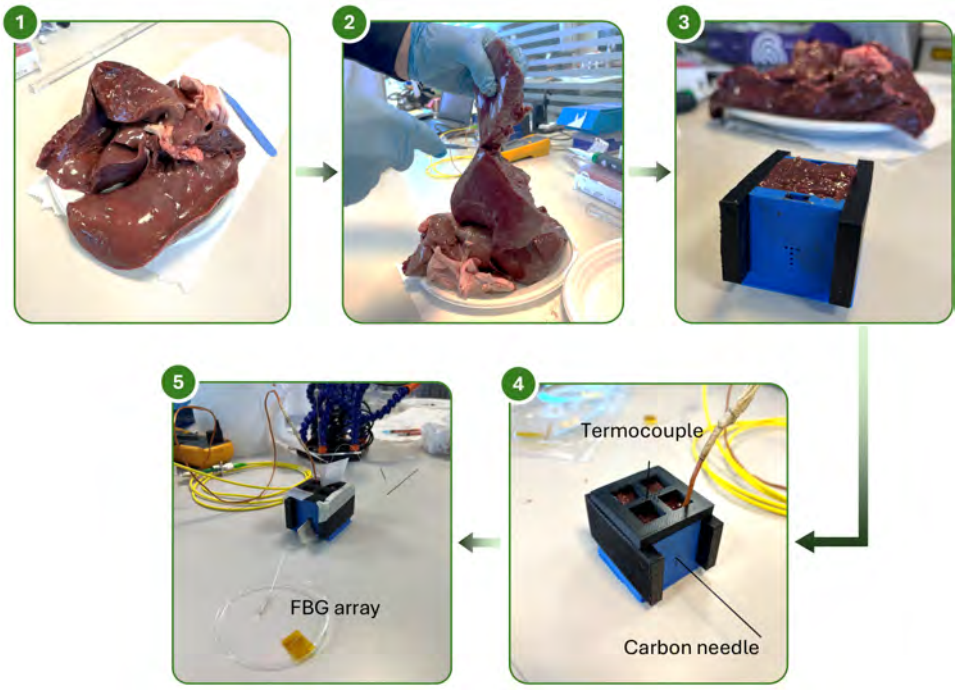

Figure 4.10: Step-by-step workflow for the preparation of the *ex vivo* porcine liver samples used in the laser ablation experiments. (1) Fresh porcine liver was procured and inspected prior to sectioning. (2) The organ was manually cut into cubic portions compatible with the PLA holder. (3) Each liver block was positioned inside the central compartment of the 3D-printed holder. (4) Carbon-fiber needles were inserted through the dedicated access channels to create guided paths within the tissue, allowing subsequent placement of the fragile FBG sensing fibers in a strain-free configuration. (5) The FBG arrays were then slid into place following the carbon-needle tracks, completing the sensor integration before laser irradiation.

A critical difference between *in vitro* and *ex vivo* configurations concerns the integration of the FBG sensors. In agarose-based phantoms, the FBG arrays could be pre-aligned in a strain-free configuration and embedded directly during gel solidification, ensuring both mechanical stability and temperature-only sensitivity. Conversely, in solid liver tissue this embedding strategy is no longer feasible, as the sensing fibers cannot be inserted before phantom formation and cannot be immobilized by gelation. Moreover, FBG fibers are thin, flexible, and inherently fragile, and cannot penetrate biological tissue when inserted directly through the 1 mm access channels located at the base of the PLA holder. To overcome this limitation, carbon-fiber insertion needles (outer diameter 300 µm) were employed as mechanical guides. The procedure consisted of inserting each needle into the tissue following the access holes of the holder, sliding the optical fiber through the lumen, and subsequently withdrawing the needle while leaving the FBG array in position. This operation was performed carefully to avoid bending, induced strain

or micro damage to the gratings. For these reasons, we decided to simplify the sensing layout and employ only two FBG arrays instead of the four used in the *in vitro* configuration. Specifically, a first array (Array A) was positioned in the central channel, immediately below the laser delivery fiber, to capture the axial temperature rise in the region of maximum energy deposition. A second array (Array B) was inserted along a channel parallel to the laser applicator, enabling measurement of lateral heat diffusion and providing a cross-sectional thermal profile of the ablation zone (see Figure 4.11). This reduced configuration ensured stable and reproducible sensor placement while minimizing the mechanical stress associated with penetrating solid liver tissue.

After positioning the two sensing arrays (A, B), the upper PLA hat containing the guiding channel for the laser fiber was mounted on the holder. The laser applicator was inserted vertically through the central guide, ensuring a fixed and reproducible spatial relationship between the irradiation axis and the sensing fibers, consistent with the geometry adopted in the *in vitro* experiments. A fixed energy protocol was applied for all *ex vivo* experiments, consisting of laser power of 3 W for 2 min of irradiation.

Beyond the experiments conducted on liver tissue, an additional series of *ex vivo* tests was performed to investigate the feasibility of AuNPs in liver laser ablation. In this exploratory phase, two classes of AuNPs, NC_2 and NR, were selected based on their strong absorption in NIR and their promising photothermal performance demonstrated during the *in vitro* agarose-based investigations. Once the FBG arrays and the laser applicator were fully positioned inside the liver block, the nanoparticle colloids were locally injected into the tissue using a microsyringe, ensuring deposition close to the ablation axis. This approach allowed the assessment of nanoparticle-assisted heat generation directly within heterogeneous biological matrices, providing qualitative and quantitative comparison between conventional and NP-enhanced laser ablation in real tissue.

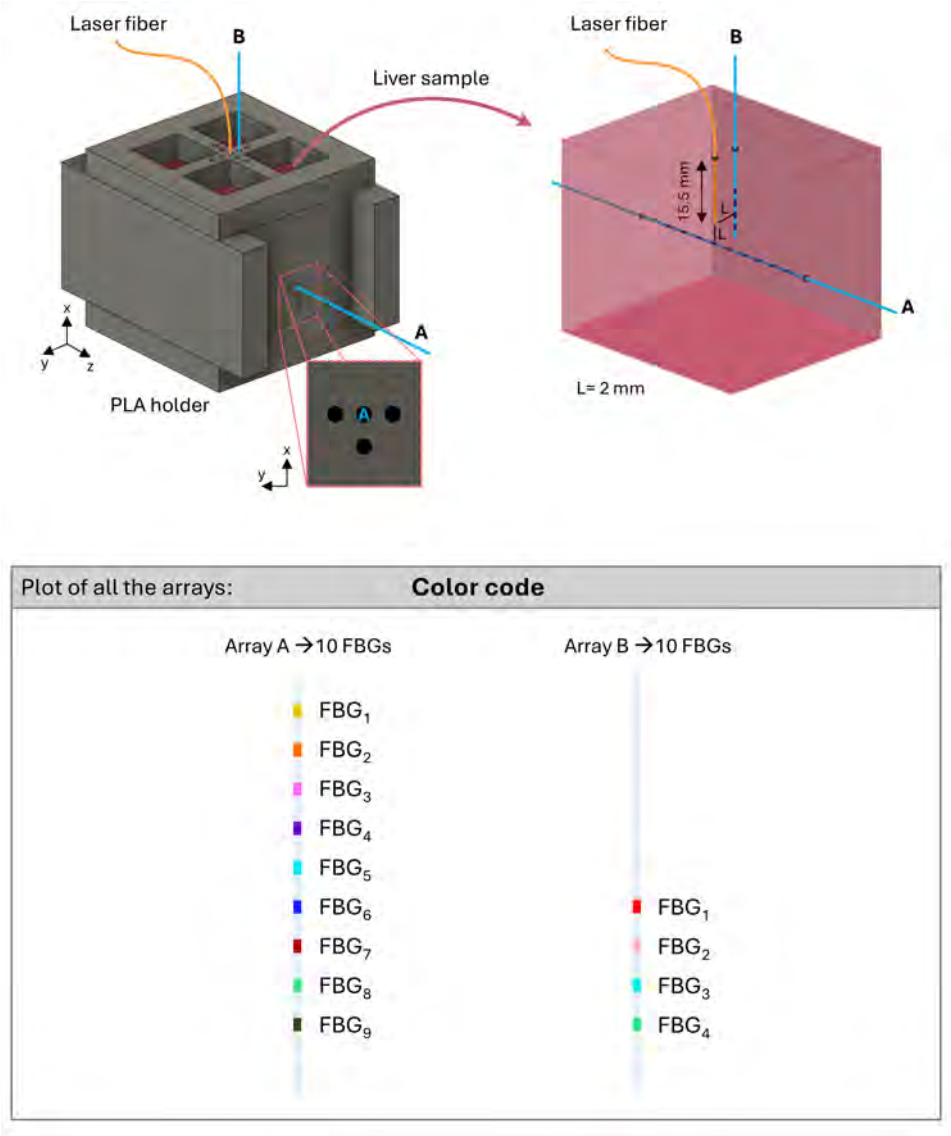

Figure 4.11: Geometric configuration adopted for the *ex vivo* experiments. The left panel shows the PLA holder containing the porcine liver sample, with the two sensing arrays (A and B) inserted through the dedicated access channels with carbon needles. Array A is positioned in the central hole, aligned just below the laser delivery fiber, while Array B is placed in the lateral channel parallel to the irradiation axis.The right panel depicts the schematic representation of the spatial arrangement inside the tissue block, showing the relative depth of the laser applicator and the 2 mm spacing between the sensing paths. This simplified two-array configuration ensures reproducible sensor placement in solid tissue and enables simultaneous measurement of axial and lateral thermal diffusion during laser ablation. In the bottom panel the color code for the FBG arrays A and B, are provided.

4.2.1 Results

Figure 4.12, Figure 4.13, Figure 4.14 report the temperature–time profiles acquired *ex vivo* in porcine liver for three representative configurations: without nanoparticles, with locally injected NC_2, and NR, respectively. In each case, the upper panels show the thermal traces recorded by the FBG arrays, while the lower panels display post-procedural photographs of the tissue, with the thermally coagulated region highlighted. At the bottom of Figure 4.11, the configuration of the two sensing arrays (A and B) is shown together with the corresponding color code assigned to each individual FBG, which will be used consistently in the result figures presented in the following sections. When compared with the *in vitro* results obtained in agarose phantoms, the *ex vivo* temperature traces appear considerably more irregular. This is expected, as biological tissue introduces substantial complexity: structural heterogeneity, variable optical absorption, anisotropic heat diffusion, and the lack of the uniform embedding conditions guaranteed in gel-based phantoms. Furthermore, in contrast to the *in vitro* setup, where the fibers were embedded during phantom formation, the FBGs were inserted retrospectively into solid liver using carbon-fiber needles. This unavoidably introduces variability both in their final positioning and in their mechanical interaction with the surrounding tissue, contributing to less uniform and more "noisy" temperature responses.

In the absence of nanoparticles (Figure 4.12), the temperature rise is moderate and spatially distributed, with array A (closer to the laser fiber) showing consistently higher ΔT than array B. The recorded thermal lesion (bottom panel) appears relatively compact and symmetric around the irradiation site.

When NC_2 were injected near the ablation axis (Figure 4.13), the temperature curves exhibit a visibly steeper rise, confirming the enhanced photothermal conversion expected from NC_2, consistent with the *in vitro* characterization. The lesion morphology also shows a slightly enlarged and more defined coagulated region compared to the blank case. However, the variability and dispersion among FBG readings remain significant due to tissue heterogeneity and imperfect nanoparticles distribution.

The NR-mediated experiment produced the highest temperature increase among the three conditions (Figure 4.14), in agreement with the strong photothermal behavior observed *in vitro*. Notably, the temperature trace of FBG_{A4} exhibits a sudden interruption followed by resumption shortly thereafter. This phenomenon likely reflects a rapid, localized thermal spike exceeding the sensor's tracking capability, temporarily pushing the reflected Bragg wavelength outside the interrogator's detection window before re-entering it once the temperature dropped. The resulting tissue damage appears more pronounced and spatially extended, indicating a more aggressive ablation profile associated with the NR-induced heating.

Although these preliminary *ex vivo* experiments provide valuable insight, they represent single experimental realizations for each condition. As such, they lack the statistical robustness and reproducibility achieved in the *in vitro* agarose studies. Additional sources of uncertainty such as variability in NP dispersion within the tissue, nonuniform fiber–tissue contact, and the intrinsic heterogeneity of biological matrices further complicate interpretation.

To obtain results comparable in reliability to the *in vitro* campaigns, future work must include larger experimental cohorts, improved control over NP injection and distribution, and refined methods for accurate positioning and stabilization of

sensing fibers. Such advances are essential before transitioning to more complex models, including tumor tissues, where differences in vascularization, stiffness, and optical properties will further influence the ablation dynamics.

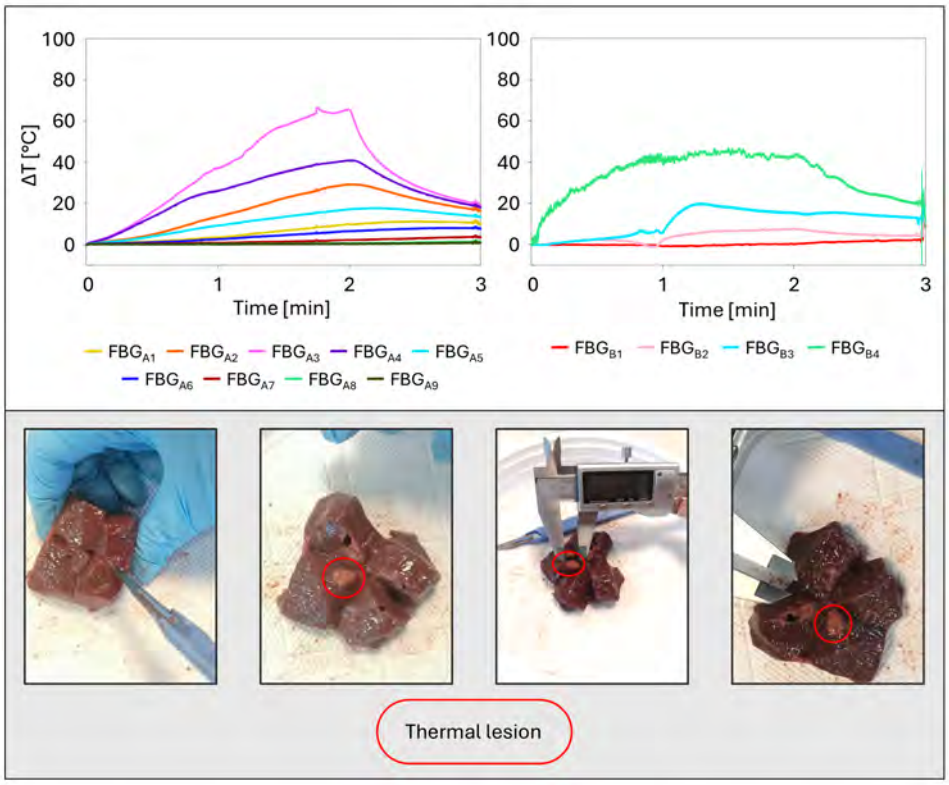

Figure 4.12: Temperature–time evolution acquired during *ex vivo* laser ablation in porcine liver without nanoparticles. The upper panels report the thermal traces measured by arrays A and B, revealing moderate and spatially distributed heating, with array A, positioned beneath the laser fiber, exhibiting higher ΔT values. The lower panels show post-ablation photographs of the sample, where the thermally coagulated region (circled) appears compact and symmetric around the irradiation site.

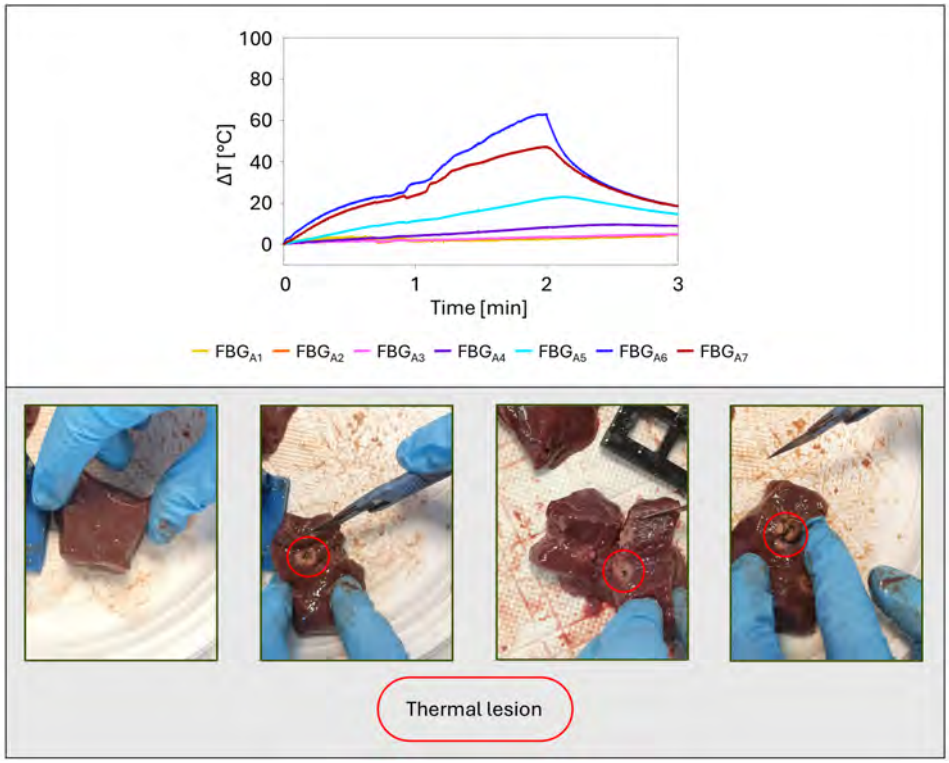

Figure 4.13: Temperature–time profiles recorded during *ex vivo* ablation after local injection of NC_2. In this specific case, a single array A comprising 7 gratings was adopted. The thermal traces (upper panel) display a steeper temperature rise compared with the blank tissue, confirming the enhanced photothermal response expected from. Post-procedural images (lower panels) reveal a more pronounced and well-defined coagulated region.

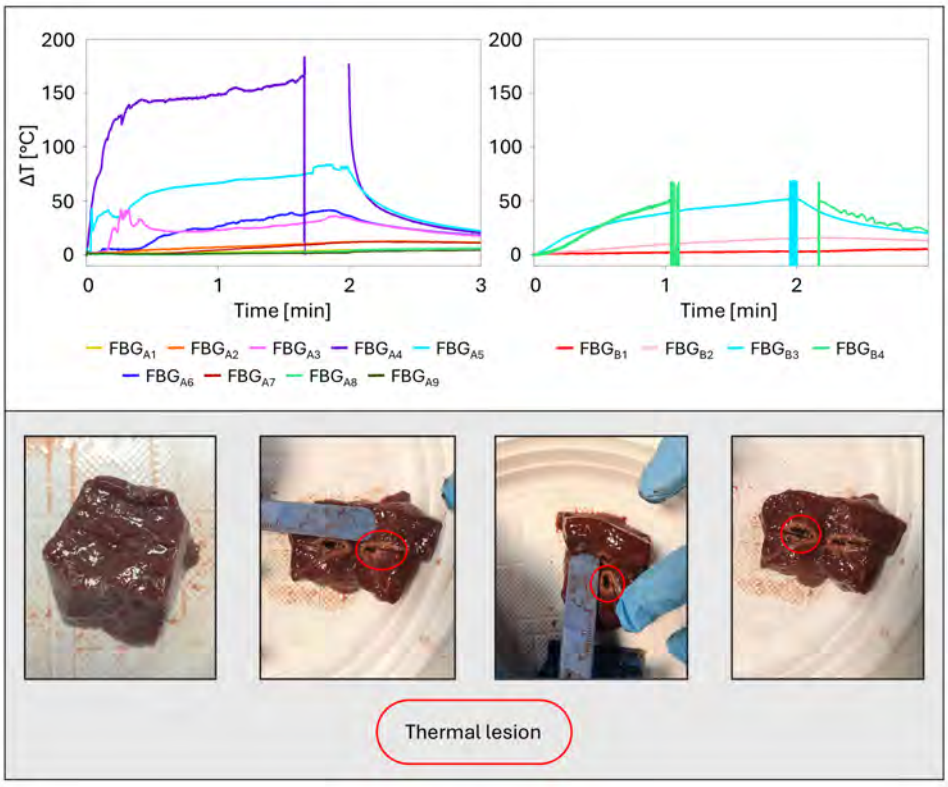

Figure 4.14: *Ex vivo* temperature measurements in porcine liver following the injection of gold NR. The upper panels show a strong and rapid temperature increase, with the signal of FBG_{A4} exhibiting a temporary interruption consistent with a transient thermal spike exceeding the interrogator's detection range. The resulting lesion (lower panels) appears more extended and elongated, consistent with the markedly higher temperatures reached during ablation. The peak temperature, approaching 200 °C, is in line with the visibly carbonized region observed in the tissue.

Computational Modeling of Laser Ablation

5

Mathematical Modeling of Laser Ablation

In recent decades, mathematical and computational modeling has emerged as an essential tool to enhance the accuracy and effectiveness of thermal ablation therapies. By providing predictive insight into the spatiotemporal evolution of heat deposition and tissue injury, these models are progressively moving towards integration within clinical workflows, where they may support *a priori* estimates of treatment outcomes and guide patient-specific planning [15, 119–122]. Numerical simulations now represent a consolidated framework for evaluating tissue response under thermal stress, particularly in laser-based approaches where energy delivery is strongly influenced by optical and thermal properties of the medium. At the core of such analyses lie three fundamental mathematical formulations: optical model to study the light propagation whitin the biological tissue, bioheat transfer models, which describe the propagation of thermal energy in tissue, and tissue damage models, which quantify the onset and progression of thermal necrosis.

In the following, the discussion will first address the mathematical formulations used to describe light transport within biological tissues, which determine the spatial distribution of absorbed laser energy. Subsequently, the focus will shift to heat transfer models, where the deposited optical energy is translated into thermal elevation and conduction through tissue. Together, these frameworks lay the groundwork for analyzing the thermal procedure in the context of cardiac ablation and for advancing computational approaches to investigate laser ablation mediated by nanoparticles, both *in vitro* and *ex vivo* experimental settings.

5.1 Optical Modeling

Optical diffusion approximation (ODA) modeling is widely used in biomedical optics to recover the mechanisms underlying light propagation within a biological medium [123]. In this context, the ODA derives from the more comprehensive Boltzmann radiative transport equation (RTE) [123, 124] describing the transport of radiative energy through a medium, accounting for absorption, scattering and emission processes [125]. The RTE represents the most complete mathematical description of photon migration, expressing the variation of the specific intensity as a

function of spatial position, propagation direction, and time. However, its integro-differential nature and high dimensionality make it computationally expensive and often impractical for biological tissues, where light undergoes multiple scattering events and the intensity field tends toward isotropy.

Under these conditions, the ODA provides a simplified but accurate approximation, obtained by assuming that scattering predominates over absorption, i.e., $\mu_s \gg \mu_a$, where μ_a and μ_s are the absorption and scattering coefficients of the medium, respectively, and that the radiance distribution can be considered nearly isotropic after several scattering events [126]. This simplification reduces the RTE to a diffusion-type equation for the light fluence rate, significantly lowering the computational burden while preserving the essential physics of optical transport. In biological tissue, especially in NIR, this condition is typically satisfied, being $\mu_s \sim 10^2 - 10^3$ times greater than μ_a, justifying the use of ODA [124].

Such an approach has been extensively validated in the literature for modeling photon migration in turbid media, including soft tissues and organs [125, 127]. In particular, Jia et al. [126] demonstrated that the diffusion approximation reliably reproduces the RTE solution beyond the ballistic and quasi-ballistic regimes, while Tricoli et al. [123] optimized the model for biological systems by introducing boundary corrections that improve accuracy near tissue interfaces.

Due to its favorable trade-off between accuracy and computational efficiency, the ODA has become the standard optical model in thermal ablation studies, providing a robust framework for estimating spatial energy deposition from laser irradiation in biological tissues. The resulting fluence rate field directly determines the volumetric heat source term in the subsequent thermal modeling phase, thereby establishing a critical link between light transport and tissue heating mechanisms.

In this context, optical properties play a crucial role influencing the distribution of laser energy within the tissue thus small variations can lead to substantial differences in the predicted thermal behavior.

The ODA equation is defined as follows:

$$-D\nabla \cdot (\nabla\varphi(x,y,z)) + \mu_a\varphi(x,y,z) = s(x,y,z) \tag{5.1}$$

where $\varphi(x,y,z)$ [$\mathrm{W\,m^{-2}}$] is the light fluence rate, μ_a the absorption coefficient and $s(x,y,z)$ [$\mathrm{W\,m^{-3}}$] the light source term. The tissue diffusion coefficient $D = 1/3(\mu_s' + \mu_a)$ [m] is derived from the material optical properties, where $\mu_s' = (1 - g)\mu_s$ [$\mathrm{m^{-1}}$] is the reduced scattering coefficient and g the tissue anisotropy factor. The latter takes into account the effects of scattering on the light beam directions; it ranges from 0.8 to 1 for biological tissues [124].

In the optical modeling, a pivotal assumption concerns the characterization of the laser source term, which is considered to be oriented along the z-axis. This choice reflects the physical nature of the laser beam, which is modeled as a highly collimated and directional light source, consistent with the emission profile of optical fibers typically used in interstitial laser ablation. Under this assumption, the photon flux is predominantly forward-directed. Such an approach simplifies the source representation in the diffusion equation while preserving the essential features of the axial energy deposition that governs the subsequent thermal response of the tissue.

With this assumption, the (5.1) reads:

$$-D\frac{\partial^2\varphi(z)}{\partial z^2} + \mu_a\varphi(z) = s(z) \tag{5.2}$$

where, the laser lateral spread is approximated by a Gaussian distribution. Accordingly, a custom bidimensional Gaussian shape is applied to the laser applicator surface:

$$I = \frac{\mathrm{P}}{2\pi\sigma^2} e^{-\frac{x^2+y^2}{2\sigma^2}} \tag{5.3}$$

with, P [W] the output laser power, $\sigma = r_f/3$ the standard deviation, and r_f the laser applicator radius.

5.2 Thermal Modeling

In this section, three distinct heat transfer models are examined to describe the spatiotemporal thermal dynamics occurring during the laser ablation process. The analysis begins with the classical Fourier-based bioheat equation, which represents the foundational framework for modeling heat conduction in biological tissues. Despite its widespread adoption and analytical simplicity, the Fourier formulation assumes instantaneous thermal propagation, neglecting the finite speed at which heat waves travel through biological matter.

To address these limitations, we next consider the Generalized Fourier (GF) model, which introduces a first-order temporal correction to account for the thermal relaxation time, a parameter that controls the lag between the temperature gradient and the resulting heat flux. This model provides an intermediate level of complexity, offering a bridge between the conventional Fourier approach and more advanced non-Fourier formulations.

Finally, our investigation extends to the Dual Phase Lag (DPL) model, a higher-order framework capable of capturing the microscale transient phenomena governing energy transport within living tissue. By incorporating two distinct phase-lag parameters, one associated with the heat flux and the other with the temperature gradient, the DPL model provides a more physically realistic representation of thermal inertia and finite-speed heat propagation. This allows for a refined description of non-equilibrium effects and delayed thermal responses, which become particularly relevant under rapid and localized heating conditions such as those induced by laser ablation.

5.2.1 Fourier-based Bioheat Model

The Pennes' bioheat transfer equation, based on the Fourier law [128], represents the cornerstone of thermal modeling in biological tissues and remains one of the most extensively adopted formulations for simulating energy transport in thermotherapeutic applications. Originally proposed by Pennes in 1948 [129], the model provides a macroscopic description of heat transfer that accounts for the combined effects of thermal conduction, metabolic heat generation, and blood perfusion. Despite its phenomenological nature, the Pennes' model continues to serve as the reference framework in computational bioheat studies due to its simplicity, robustness, and capability to capture the dominant mechanisms of temperature evolution in perfused tissues [120, 130, 131].

The Pennes' formulation assumes that the tissue behaves as a continuum medium, characterized by effective thermophysical parameters that homogenize the microscopic processes of energy exchange between blood and parenchyma. The perfusion term plays a central role in this formulation, acting as a volumetric

heat sink (or source) that regulates temperature through convective exchange with blood vessels. Although the model neglects directional flow and spatial heterogeneity of the vascular network, it has been proven to yield accurate predictions in several hyperthermia and thermal ablation applications, including radiofrequency, microwave, and laser-based treatments [132].

Accordingly, the governing equation for the Pennes' bioheat model can be expressed as:

$$\rho \mathrm{c}(\mathrm{T}) \frac{\partial \mathrm{T}}{\partial t} = \nabla \cdot (\mathrm{k}(\mathrm{T}) \nabla \mathrm{T}) + \mathrm{Q_b} + \mathrm{Q_m} + \mathrm{Q_s} \tag{5.4}$$

where, T [K] is the tissue temperature, ρ [$\mathrm{kg\,m^{-3}}$] the density, c(T) [$\mathrm{J\,kg^{-1}\,K^{-1}}$] the heat capacity, k(T) [$\mathrm{J\,kg^{-1}\,K^{-1}}$] the thermal conductivity, $\mathrm{Q_b} = -\rho_\mathrm{b} \mathrm{c_b} \omega_\mathrm{b} (\mathrm{T} - \mathrm{T_b})$, $\mathrm{Q_m}$, $\mathrm{Q_s} = \mu_a \varphi$ [$\mathrm{W\,m^{-3}}$] the blood perfusion, metabolic heat and laser heating source contributions, respectively.

5.2.2 Generalized Fourier model

The Fourier model assumes an instantaneous response to thermal energy input, meaning that any temperature change is immediately reflected throughout the medium. This assumption simplifies the analysis but may not always capture the transient nature of heat transfer, especially in biological tissue where the response can be delayed. Indeed, classical Fourier-based models struggle to accurately represent the finite speed of thermal propagation, primarily due to biological tissue complexity and its heterogeneous microstructure. This limitation becomes particularly evident in hyperthermal treatments, where rapid temperature rises occur within short time frames and are driven by steep temperature gradients [133]. Such dynamic and localized thermal behavior demands a more advanced approach to fully capture the underlying physics.

Different theories have been proposed to account for non-Fourier behavior, including hyperbolic heat equations and relativistic heat transfer. The scientific literature indicates that thermal behavior in non-homogeneous media requires a relaxation time to accumulate enough energy before transferring it to the nearest element [133]. In this work, we first introduce a generalization of the Fourier-based model by incorporating a pseudo-convective term in (5.4), governed by the time constant τ_t.

The GF equation is expressed as follows:

$$\rho \mathrm{c}(\mathrm{T}) \frac{\partial \mathrm{T}}{\partial t} = \nabla \cdot (\mathrm{k}(\mathrm{T}) \nabla \mathrm{T}) + \tau_t \nabla \cdot \left(\mathrm{k}(\mathrm{T}) \frac{\partial \nabla \mathrm{T}}{\partial t} \right) + \mathrm{Q_b} + \mathrm{Q_m} + \mathrm{Q_s} \tag{5.5}$$

where, τ_t is the phase lag of the temperature gradient. Notably, if $\tau_t = 0$, the equation reduces to the classical bioheat heat conduction equation (5.4), effectively removing the pseudo-convective term.

5.2.3 Dual Phase Lag Model

Among the theoretical frameworks developed to describe non-Fourier heat conduction, Tzou [134] introduced a hyperbolic heat equation that incorporates finite-speed thermal propagation by accounting for time delays in both the heat flux and the temperature gradient. This formulation, known as the Dual Phase Lag model,

extends the concept of thermal relaxation by recognizing that the establishment of a temperature gradient and the resulting heat flux do not occur instantaneously but rather exhibit distinct temporal lags.

Originally conceived for solid materials, particularly metals subjected to rapid heating or pulsed laser irradiation, the DPL model has been successfully adapted to biological systems, where transient heating phenomena and structural heterogeneity play a crucial role in determining thermal response [135, 136]. In living tissues, the propagation of thermal energy is influenced by multi-scale interactions, including cellular water content, microvascular perfusion, and anisotropic conduction through fibrous structures. These factors make the assumption of instantaneous thermal diffusion inadequate, especially under short-duration and localized heating such as in laser ablation.

Accordingly, the DPL theory introduces two independent phase lag times: τ_q, representing the delay between the heat flux and the temperature gradient, and τ_t, corresponding to the lag in the establishment of the temperature gradient within the conductive medium [134]. The inclusion of these parameters allows the model to capture non-equilibrium thermal effects and reproduce the finite-speed propagation of thermal waves observed experimentally in biological tissues.

In the context of laser ablation, the DPL formulation is particularly relevant as it accurately describes the initial transient temperature rise that precedes the establishment of steady heat conduction. This early-stage behavior has a critical influence on tissue damage evolution, since the rate and extent of the initial thermal spike govern the onset of protein denaturation and irreversible cell injury [137].

Mathematically, the DPL equation can be expressed as a second-order generalization of the GF model (5.5) and is expressed as:

$$\tau_{\mathrm{q}}\rho\mathrm{c}(\mathrm{T})\frac{\partial^2\mathrm{T}}{\partial\mathrm{t}^2}+\rho\mathrm{c}(\mathrm{T})\frac{\partial\mathrm{T}}{\partial t}=\nabla\cdot(\mathrm{k}(\mathrm{T})\nabla\mathrm{T})+\tau_t\nabla\cdot\left(\mathrm{k}(\mathrm{T})\frac{\partial\nabla\mathrm{T}}{\partial t}\right)+\mathrm{Q_b}+\mathrm{Q_m}+\mathrm{Q_s} \quad (5.6)$$

5.3 Thermal Damage Modeling

Accurately quantifying thermal damage is a crucial step in the computational modeling of ablation therapies, as it determines the extent of irreversible tissue necrosis and ultimately defines the therapeutic outcome. Several methods have been proposed in the literature to estimate the ablated volume during simulation studies, including isothermal contouring, thermal isoeffective dose (TID), and Arrhenius-based models [15]. These approaches differ in their underlying physical assumptions, computational complexity, and ability to account for time-dependent and tissue-specific effects. A comprehensive comparative analysis and critical review of the mathematical frameworks used to predict cell death during thermal ablation is provided by Pearce [138], who outlined their respective strengths and limitations in different thermotherapeutic contexts.

The most straightforward approach is the isothermal contour method, which defines the ablated region by a chosen temperature threshold, typically the 50 °C isotherm, beyond which irreversible damage is assumed to occur [13, 139–141]. Although simple and computationally efficient, this technique relies on a static criterion that correlates tissue necrosis solely with local temperature. It thus neglects critical parameters such as exposure duration, thermal history, and cellular heterogeneity, which can significantly influence the onset of denaturation and apoptosis.

To refine this approach, higher threshold isotherms (e.g., 55 °C and 59 °C) have been employed in more recent studies to better align with experimental findings across different tissue types [15]. Nevertheless, all isothermal criteria share the same inherent limitation: they implicitly assume that cell death is an instantaneous process determined exclusively by temperature, overlooking the cumulative and time-dependent nature of thermal injury. To overcome these shortcomings, more sophisticated kinetic-based models have been introduced, most notably, the TID model and the Arrhenius integral formulations [15, 139]. These models couple temperature evolution with the exposure time, enabling a dynamic quantification of cellular injury that captures the progressive accumulation of thermal effects. In particular, the Arrhenius framework interprets tissue damage as a first-order chemical reaction, relating the rate of cell death to the temperature-dependent denaturation kinetics of biological macromolecules.

The TID model provides a standardized framework to quantify thermal damage by converting different combinations of temperature and exposure time into a single equivalent metric. This approach expresses the total thermal effect as the Cumulative Equivalent Minutes at 43 °C (CEM_{43}), effectively normalizing diverse heating protocols to a common reference temperature. In doing so, the TID model enables direct comparison between different thermal histories that produce equivalent biological effects [142, 143]. The underlying rationale is that tissue damage is governed not only by the peak temperature reached but also by the duration of exposure, as both jointly determine the extent of protein denaturation and cell death. Hence, the TID metric integrates the entire thermal history of the process, attributing greater weight to higher temperatures and shorter times that induce comparable injury to longer, milder heating regimes.

Mathematically, the CEM_{43} is computed as:

$$\mathrm{CEM}_{43} = \int_0^t \mathrm{R}^{(43-\mathrm{T})} dt \quad (\mathrm{min}) \tag{5.7}$$

where, T [°C] denotes the constant tissue temperature, t [min] is the exposure time, and R is a temperature correction factor that compensates for the change in biological reaction rate associated with each 1 °C variation in temperature. Typically, R = 0.5 is adopted for T > 43 °C, indicating that the equivalent time doubles for every degree increase, whereas R = 0.25 is used for T < 43 °C, corresponding to a fourfold reduction in equivalent time per degree decrease [144]. Empirically, critical thermal doses of $CEM_{43} = 120 - 240$ min have been identified as thresholds for complete and irreversible tissue necrosis. While this model has proven to be a reliable and standardized indicator for mild hyperthermia treatments, typically within the 40 °C – 45 °C range, it becomes less suitable for high-temperature ablation procedures (T > 50 °C). In such regimes, tissue injury progresses through rapid protein denaturation and structural collapse, phenomena that are not adequately represented by the TID's cumulative-time framework [15, 138, 145]. Consequently, while the TID model remains valuable for treatment normalization and comparison, it is often replaced in thermal ablation modeling by kinetic formulations, such as the Arrhenius damage model, which more accurately capture the temperature-dependent rate of irreversible cell death.

The Arrhenius damage model provides a simple yet robust framework for predicting the extent of tissue injury in thermal ablation simulations and remains one of the most widely employed approaches in computational bioheat analysis [15,

139]. The model assumes that thermal damage arises from irreversible protein denaturation, which can be described as a first-order chemical reaction governed by temperature-dependent kinetics:

$$\Omega(t) = \int_0^t \mathrm{A} \cdot \exp^{-\mathrm{E_a}/\mathrm{RT}} \tag{5.8}$$

where, $\Omega(t)$ is the damage integral, quantifying the cumulative degree of thermal injury, A [s^{-1}] is the frequency factor, E_a [$J\,mol^{-1}$] is the activation energy, R is the universal gas constant ($8.314\,J\,mol^{-1}\,K^{-1}$), and T [K] is the tissue temperature at time t. The parameters A and E_a are tissue-specific and on the molecular composition and structural organization of the biological matrix, reflecting how different tissues respond to heat-induced protein denaturation and cell death. In terms of interpretation, $\Omega(t) = 1$ corresponds to approximately a 63 % probability of cell death, while $\Omega(t) = 4.6$ represents about 99 % cell death, values commonly used to define the threshold for irreversible thermal injury [15]. As such, the Arrhenius integral provides a quantitative and continuous measure of tissue damage, linking microscopic biochemical reactions to macroscopic lesion formation.

Over the past decades, the Arrhenius framework has become the benchmark model for assessing and comparing alternative damage formulations [138, 145–147]. Nonetheless, its simplifying assumptions impose certain limitations. Specifically, it treats the biological tissue as a homogeneous system undergoing a single irreversible transformation, thereby reducing the complex, multi-step nature of cell injury to a binary state, either viable or non viable. In reality, cell death during thermal ablation is governed by a continuum of biochemical and structural alterations, including protein unfolding, membrane disruption, apoptosis, and necrosis, many of which exhibit reversibility or delayed onset.

To overcome these constraints, more advanced models have been developed that incorporate multiple state variables or reaction pathways, such as multi-rate Arrhenius formulations and the three-state cell death model, which explicitly distinguish between reversible and irreversible phases of thermal injury [138]. These approaches provide a more physiologically consistent description of the progressive nature of thermal damage, particularly under non-equilibrium heating conditions such as those encountered in laser ablation.

The three-state cell death model, first introduced by O'Neill et al. [146], extends the classical Arrhenius formulation by introducing an intermediate, thermally vulnerable state that accounts for partial and potentially reversible cellular injury. Unlike traditional two-state models, which classify cells as either alive or dead, this framework captures the transient recovery mechanisms that may occur following moderate thermal stress, such as protein refolding and repair of sub-lethal membrane damage. The model distinguishes three distinct cellular populations: native (N), unfolded (U), and denatured (D) states. Cells in the native state represent healthy, fully functional tissue; cells in the unfolded state have suffered structural damage but retain the potential to revert to their original condition; and cells in the denatured state are irreversibly damaged, corresponding to cell death. Transitions between these states are governed by temperature-dependent reaction rates $\alpha_i(\mathrm{T})$, as illustrated below:

$$\mathrm{N} \underset{\alpha_3(\mathrm{T})}{\overset{\alpha_1(\mathrm{T})}{\rightleftharpoons}} \mathrm{U} \xrightarrow{\alpha_2(\mathrm{T})} \mathrm{D} \tag{5.9}$$

here, α_1, α_3 describe the forward and backward transitions between the native and unfolded states, while α_3 represents the irreversible transition from the unfolded to the denatured state. This structure enables the model to reproduce both reversible recovery dynamics and irreversible injury progression, depending on the local temperature and exposure time.

The transition rates governing the three-state dynamics follow first-order Arrhenius kinetics, which describe the temperature dependence of each reaction pathway:

$$\alpha_i(\mathrm{T}) = \mathrm{A}_i e^{-\Delta \mathrm{E}_i/(\mathrm{RT})} \tag{5.10}$$

here, A_i [s^{-1}] and $\Delta \mathrm{E}_i$ [$\mathrm{J\,mol}^{-1}$] denote, respectively, the frequency factor and activation energy associated with each transition i, while R represents the universal gas constant, and T [K] is the local tissue temperature, obtained from the bioheat model solution. Each rate constant thus encapsulates the thermal sensitivity of the molecular processes driving the transformation between the cellular states.

Given that the characteristic time scale of ablation (on the order of seconds to minutes) is vastly shorter than the biological proliferation or regeneration time (typically weeks to months), cell proliferation effects are neglected. As a consequence, the model assumes conservation of the total cellular population, such that at any time the sum of the three state fractions remains constant: $\mathrm{N} + \mathrm{U} + \mathrm{D} = 1$ [148]. The resulting system of coupled ordinary differential equations describes the temporal evolution of the three state variables:

$$\begin{cases} \dfrac{d\mathrm{N}}{dt} = -\alpha_1(\mathrm{T})\mathrm{N} + \alpha_3(\mathrm{T})\mathrm{U} \\ \dfrac{d\mathrm{U}}{dt} = \quad \alpha_1(\mathrm{T})\mathrm{N} - (\alpha_2(\mathrm{T}) + \alpha_3(\mathrm{T}))\,\mathrm{U} \\ \dfrac{d\mathrm{D}}{dt} = \quad \alpha_2(\mathrm{T})\mathrm{U} \end{cases} \tag{5.11}$$

The system is initialized by assuming that all cells are initially in the native state, i.e., $\mathrm{N} = 1$, $\mathrm{U} = 0$, and $\mathrm{D} = 0$. This initial condition reflects the physiological baseline before the onset of laser heating, from which the transition dynamics evolve according to the local temperature field.

Originally developed for generic biological tissues, the three-state model has since been applied and refined in several computational studies of thermal ablation, demonstrating its capability to simulate the spatiotemporal evolution of tissue viability under different heating conditions [131, 139, 149, 150]. Its flexibility makes it particularly suitable for modeling laser-induced hyperthermia, where temperature gradients and exposure times can produce a wide spectrum of cellular responses ranging from reversible stress to complete necrosis.

6

Cardiac Ablation Modeling

Building upon the mathematical foundations established in Chapter 5, this section translates the previously developed optical–thermal frameworks into their specific application to cardiac tissue. While the earlier chapter focused on the formulation and characterization of the governing models, covering light propagation and heat transfer, the present chapter applies these models to simulate laser ablation in the myocardium. In this context, the biothermal problem becomes more complex due to the intrinsic anisotropy of cardiac tissue, which stems from the organized arrangement of myocardial fibers and their depth-dependent orientation across the ventricular wall. Such anisotropy significantly affects the local heat diffusion and lesion morphology, and it is therefore explicitly incorporated into the thermal model through a direction-dependent conductivity tensor.

A comparative analysis among three heat-transfer formulations, namely the Fourier bioheat model, the Generalized Fourier model, and the Dual Phase Lag model, is conducted to evaluate their predictive capabilities under the same boundary and source conditions. This comparison allows assessing how non-Fourier effects influence the spatiotemporal temperature distribution and, consequently, the extent of thermal injury.

Furthermore, the chapter introduces a dedicated three-state cell death model, specifically adapted and calibrated for cardiomyocytes, to describe the dynamic progression of thermal damage under hyperthermic exposure. By integrating this bio-damage kinetics with the anisotropic thermal response, the model enables a more physiologically consistent representation of lesion development during cardiac laser ablation. Altogether, these implementations lay the groundwork for exploring the feasibility of laser-based ablation as a controlled therapeutic option for arrhythmogenic substrates in cardiac tissue.

6.1 Cardiac LA computational modeling

The computational model of cardiac laser ablation was implemented using an in-house Python code developed on top of the open-source FEniCSx finite element library [151–153]. This framework allows for the efficient numerical solution of coupled optical–thermal problems in complex, anisotropic geometries, while offering full control over mesh refinement, temporal discretization, and boundary condition

definition. The simulated energy delivery protocol reproduces a standard ablation sequence, consisting of a 30 s laser-on phase at a power of 3 W, followed by a 270 s cooling or relaxation period, during which no additional energy is supplied and the tissue undergoes passive heat diffusion and convective dissipation.

The optical field within the cardiac tissue is modeled through the ODA formulation, which describes the photon propagation and energy absorption according to the local optical properties of the myocardium. The optical coefficients considered in this study are reported in Table 6.1 [154].

Heat transfer in the myocardium is simulated using the three distinct formulations: the classical Fourier-based bioheat model, GF and DPL models. This comparative approach enables evaluation of the impact of higher-order thermal transport effects on temperature evolution and lesion geometry under identical irradiation conditions.

Compared to the general formulations presented in Section 5.2, the present model introduces anisotropic heat conduction, an essential feature to account for the directional dependence of myocardial thermal diffusivity imposed by its fibrous architecture. This modification is implemented through the thermal conductivity tensor $\mathbf{k}(\mathrm{T})$, which reflects the distinct heat transfer rates along and across the cardiac fibers. $\mathbf{k}(\mathrm{T})$ is defined as a symmetric, positive-definite tensor accounting for the local fiber orientation, in particular:

$$\mathbf{k}(\mathrm{T}) = \mathbf{R} \begin{bmatrix} \mathrm{k_f}(\mathrm{T}) & 0 & 0 \\ 0 & \mathrm{k_t}(\mathrm{T}) & 0 \\ 0 & 0 & \mathrm{k_n}(\mathrm{T}) \end{bmatrix} \mathbf{R^T} \tag{6.1}$$

where, $\mathrm{k}_i(\mathrm{T})$, with $i = \mathrm{f}, \mathrm{t}, \mathrm{n}$, represent the temperature-dependent thermal conductivities in the fiber, transverse and normal directions, respectively, following a linear decreasing dependency:

$$\mathrm{k}_i(\mathrm{T}) = \mathrm{k}_0(1 + \mathrm{k}_1(\mathrm{T} - \mathrm{T_{myo}})) \tag{6.2}$$

with k_0 the thermal conductivity at body temperature, k_1 a non-dimensional constant gain and $\mathrm{T_{myo}} = 37\,^{\circ}\mathrm{C}$ is the reference myocardium temperature. Additionally, in the analysis we assume transversal conductivities equal and proportional to $\mathrm{k_f}$. Specifically, $\mathrm{k_t} = \mathrm{k_n} = \mathrm{k_f}/\mathrm{k_{ratio}}$, whereby $\mathrm{k_{ratio}}$ is the anisotropy ratio, object of an upcoming computational parametric analysis.

In (6.1), $\mathbf{R}$ represents the rotation matrix, based on the local fiber reference system:

$$\mathbf{R} = \begin{bmatrix} \cos\theta & -\sin\theta & 0 \\ \sin\theta & \cos\theta & 0 \\ 0 & 0 & 1 \end{bmatrix} \tag{6.3}$$

Following Molinari et al. [133], we considered a rotational anisotropy in the ventricular myocardium. This involves a 120° counterclockwise rotation of the fibers from the outermost (epicardium) to the innermost layer (endocardium) [155]. The myocardial fibers rotate across the ventricular wall, creating a sheet-like transversely isotropic material that alters the conductivity properties throughout the depth. Thus, the material is characterized by both directional dependence (anisotropy) and non-uniformity (heterogeneity). The fibers' rotational anisotropy is mathematically described as:

$$\theta(\mathrm{z}) = \theta_{\mathrm{epi}} + \frac{\mathrm{z} - \mathrm{z_{epi}}}{\mathrm{z_{endo}} - \mathrm{z_{epi}}}(\theta_{\mathrm{endo}} - \theta_{\mathrm{epi}}) \tag{6.4}$$

where z is the thickness direction.

In addition, a linear decreasing relation was considered for the heat capacity in (5.4), (5.5), (5.6):

$$\mathrm{c}(\mathrm{T}) = \mathrm{c}_0(1 + \mathrm{c}_1(\mathrm{T} - \mathrm{T}_{\mathrm{myo}})) \tag{6.5}$$

where, c_0 is the reference value at body temperature, c_1 is a nondimensional constant gain and $\mathrm{T}_{\mathrm{myo}} = 37\,^{\circ}\mathrm{C}$ is the reference myocardium temperature.

The overall thermal model coefficients considered in this study are reported in Table 6.1.

6.1.1 Weak Formulation

The nonlinear models illustrated in the previous sections are discretized in time using an implicit Euler scheme, ensuring numerical stability during the simulation of rapid thermal transients. Each equation is linearized around the previous time step and solved through a custom finite element implementation developed within the FEniCSx environment. This approach allows an efficient and accurate solution of the coupled, nonlinear bioheat equations while accounting for temperature-dependent and anisotropic material properties.

In detail, the three bioheat formulations, (5.4), (5.5), and (5.6), describe a transient heat conduction problem in the temperature field T, defined over a spatial domain $\Omega \subset \mathbb{R}^3$. The boundary of the computational domain is decomposed as $\partial\Omega = \Gamma_{\mathrm{R}} + \Gamma_{\mathrm{D}} + \Gamma_{\mathrm{N}}$, where Γ_{R}, Γ_{D} and Γ_{N} denote the Robin, Dirichlet and Neumann boundaries, respectively (see Figure 6.2(b)). Accordingly, defining the trial function $\mathrm{T}^{n+1} \in H^1(\Omega_D)$, at the new time step n+1 and test function $\mathrm{v} \in H^1(\Omega_D)$, the weak formulation of the Fourier model reads:

$$\begin{aligned} &\int_\Omega \rho \mathrm{c}(\mathrm{T}^n)\frac{\mathrm{T}^{n+1} - \mathrm{T}^n}{\Delta \mathrm{t}}\mathrm{v}\, dV \;+\; \int_{\Gamma_{\mathrm{R}}} h_T(\mathrm{T}^{n+1} - \mathrm{T}_{\mathrm{myo}})\mathrm{v}\, dS \;+ \\ &\quad + \int_\Omega \mathbf{k}(\mathrm{T}^n)\nabla \mathrm{T}^{n+1}\nabla \mathrm{v}\, dV = \int_\Omega (\mathrm{Q}_{\mathrm{b}} + \mathrm{Q}_{\mathrm{m}} + \mathrm{Q}_{\mathrm{s}})\mathrm{v}\, dV \end{aligned} \tag{6.6}$$

The weak formulation of the GF model is:

$$\begin{aligned} &\int_\Omega \rho \mathrm{c}(\mathrm{T}^n)\frac{\mathrm{T}^{n+1} - \mathrm{T}^n}{\Delta \mathrm{t}}\mathrm{v}\, dV + \int_{\Gamma_{\mathrm{R}}} h_T(\mathrm{T}^{n+1} - \mathrm{T}_{\mathrm{myo}})\mathrm{v}\, dS \;+ \\ &\qquad + \int_\Omega \mathbf{k}(\mathrm{T}^n)\nabla \mathrm{T}^{n+1}\nabla \mathrm{v}\, dV \;+ \\ &\quad + \tau_t \int_{\Gamma_R} \frac{h_T\left(\mathrm{T}^{n+1} - \mathrm{T}_{\mathrm{myo}}\right) - h_T\left(\mathrm{T}^n - \mathrm{T}_{\mathrm{myo}}\right)}{\Delta \mathrm{t}}\mathrm{v}\, dS \;+ \\ &\qquad + \tau_t k_0 k_1 \int_{\partial\Omega} \mathrm{v}\frac{\mathrm{T}^{n+1} - \mathrm{T}^n}{\Delta \mathrm{t}}\nabla \mathrm{T}^{n+1}\cdot \hat{\mathbf{n}}\, dS \;+ \\ &+ \tau_t \int_\Omega \nabla \mathrm{v}\mathbf{k}(\mathrm{T}^n)\frac{\nabla \mathrm{T}^{n+1} - \nabla \mathrm{T}^n}{\Delta \mathrm{t}}\, dV = \int_\Omega (\mathrm{Q}_{\mathrm{b}} + \mathrm{Q}_{\mathrm{m}} + \mathrm{Q}_{\mathrm{s}})\mathrm{v}\, dV \end{aligned} \tag{6.7}$$

The weak formulation of the DPL model is:

$$\tau_q \int_\Omega \rho \mathrm{c}(\mathrm{T}^n) \frac{\mathrm{T}^{n+1} - 2\mathrm{T}^n + \mathrm{T}^{n-1}}{\Delta \mathrm{t}^2} \mathrm{v}\, dV + \int_\Omega \rho \mathrm{c}(\mathrm{T}^n) \frac{\mathrm{T}^{n+1} - \mathrm{T}^n}{\Delta \mathrm{t}} \mathrm{v}\, dV + \\ + \int_{\Gamma_\mathrm{R}} h_T (\mathrm{T}^{n+1} - \mathrm{T}_\mathrm{myo}) \mathrm{v}\, dS + \int_\Omega \mathbf{k}(\mathrm{T}^n) \nabla \mathrm{T}^{n+1} \nabla \mathrm{v}\, dV + \\ + \tau_t \int_{\Gamma_\mathrm{R}} \frac{h_T \left(\mathrm{T}^{n+1} - \mathrm{T}_\mathrm{myo}\right) - h_T \left(\mathrm{T}^n - \mathrm{T}_\mathrm{myo}\right)}{\Delta \mathrm{t}} \mathrm{v}\, dS + \\ \tau_t k_0 k_1 \int_{\partial\Omega} \mathrm{v} \frac{\mathrm{T}^{n+1} - \mathrm{T}^n}{\Delta \mathrm{t}} \nabla \mathrm{T}^{n+1} \cdot \hat{\mathbf{n}}\, dS + \tau_t \int_\Omega \nabla \mathrm{v} \mathbf{k}(\mathrm{T}^n) \frac{\nabla \mathrm{T}^{n+1} - \nabla \mathrm{T}^n}{\Delta \mathrm{t}}\, dV = \\ \int_\Omega (\mathrm{Q_b} + \mathrm{Q_m} + \mathrm{Q_s}) \mathrm{v}\, dV \tag{6.8}$$

6.1.2 Thermal Damage

In the context of cardiac laser ablation, the assessment of irreversible thermal injury requires a biologically consistent representation of cellular response to temperature exposure. Among the several models proposed in literature (refer to Section 5.3), the present work adopts a three-state cell death model, which offers a more physiologically accurate description of the progressive transition from viable to irreversibly damaged cardiomyocytes.

As aforementioned above, the model distinguishes three cellular populations: the N state representing healthy cells, the U state associated with reversible injury, and the D state corresponding to irreversible cell death. The temporal evolution of these states is governed by a coupled system of temperature, dependent rate equations that capture both the onset and recovery of thermal damage (5.11). This approach is particularly relevant in cardiac tissue, where partial recovery mechanisms, such as the activation of heat shock proteins (e.g., HSP70), can mitigate sublethal stress effects, phenomena that simpler Arrhenius-based models fail to reproduce [138, 146].

Since this model is not specific for the cardiomyocites, the implementation follows the calibration procedure proposed by Petras et. al. [132], specifically adapted to cardiomyocytes. The model parameters, frequency factors and activation energies, were tuned to reproduce the experimental behavior of myocardial cells under controlled hyperthermic exposure [156]. In particular, the model ensures: absence of damage at physiological temperature of 37 °C, reversible injury below 48 °C for exposure times up to 60 s and irreversible necrosis occurring between 50 °C and 56 °C after 60 s of heating, in agreement with in vitro findings [156, 157].

To account for the experimentally observed variability in energy absorption, the transition rate between the native and unfolded states (α_1) is modeled as a piecewise Arrhenius function with a slope discontinuity at 55 °C, reflecting the temperature-dependent reduction in cellular heat absorption [158, 159] (Figure 6.1). The overall frequency factor and activation energy are given as $\mathrm{A} = \mathrm{A}_1\mathrm{A}_2/\mathrm{A}_3$ and $\Delta\mathrm{E} = \Delta\mathrm{E}_1 + \Delta\mathrm{E}_2 - \Delta\mathrm{E}_3$, respectively. For $\mathrm{T} \leq 55\,^\circ\mathrm{C}$, $\mathrm{A} = 2.97 \cdot 10^{70}\,\mathrm{s}^{-1}$ and $\Delta\mathrm{E} = 4.484 \cdot 10^5\,\mathrm{J\,mol}^{-1}$. In the case $\mathrm{T} > 55\,^\circ\mathrm{C}$, the overall frequency factor

and activation energy become $A = 1.19 \cdot 10^{19}\,s^{-1}$ and $\Delta E = 1.255 \cdot 10^{5}\,J\,mol^{-1}$, respectively. The three-state cell death model coefficients considered in this study are reported in Table 6.1. Finally, considering the several intrinsic mechanisms contributing to the slow death of a damaged cell, we use a threshold value for the cells in the native state N, below which cell death is expected to occur. Since no specific data is available for cardiomyocytes, we consider the irreversible damage threshold to be $N \leq 0.8$ following Petras et al. [146, 160].

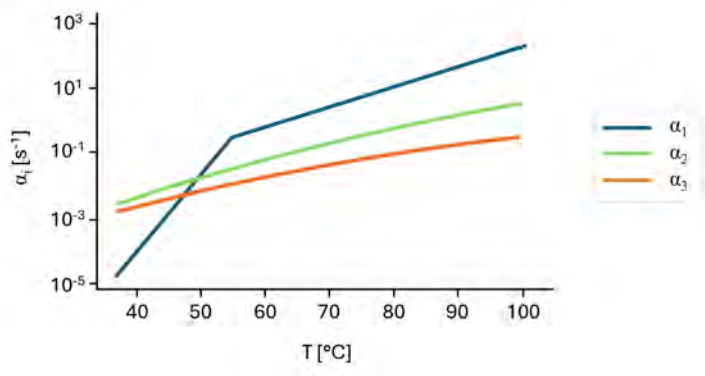

Figure 6.1: Temperature-dependet transition rates α_i, with i=1, 2,3 of the three-state cell death model for cardiomyocites. The curves represent the rate constants governing the transitions between N, U and D states. A discontinuity in α_1 at 55 °C reflects the experimentally observed change in cellular energy absorption, distinguishing the sublethal and necrotic thermal regimes [132].

This formulation represents a robust foundation for modeling laser-induced cardiac ablation, where temperature transients are rapid and highly localized. By coupling the three-state kinetics with the anisotropic heat transfer framework described earlier, the model enables computational prediction of damage patterns in myocardial tissue, providing a physiologically grounded tool for the study of lesion formation and optimization of laser ablation protocols.

6.1.3 Computational model implementation

Figure 6.2(a) illustrates the computational domain generated using the open-source platform *SALOME ®9.11.0* [161], which was employed to construct the finite element mesh and define the boundary regions for the subsequent simulations. The model geometry was designed to reproduce a representative portion of cardiac tissue subjected to localized laser irradiation.

The laser applicator, with radius $r_f = 0.4\,mm$, is placed at the center of the domain. To optimize the computational efficiency without compromising the accuracy of the thermal field, the full geometric representation of the applicator tip was not explicitly modeled. Instead, an appropriate insulating boundary condition was imposed on the corresponding surface, effectively reproducing the thermal isolation between the optical fiber and the surrounding medium. This approach allows capturing the correct spatial energy distribution while maintaining a reduced mesh complexity, thereby facilitating stable and efficient numerical integration during the laser-on phase.

Table 6.1: Optical, thermal and cell-death model parameters.

Parameter		Value	[u]
Optical Model			
Myocardium absorption coefficient	μ_a	$3 \cdot 10^1$	m^{-1}
Myocardium scattering coefficient	μ_s	$1.775 \cdot 10^4$	m^{-1}
Myocardium anisotropy factor	g	0.964	
Thermal Model			
Myocardium density	ρ	1076	$\mathrm{kg\,m}^{-3}$
Reference thermal conductivity	k_0	0.518	$\mathrm{W\,m}^{-1}\,\mathrm{K}^{-1}$
Thermal conductivity constant	k_1	-0.0005	K^{-1}
Reference heat transfer coefficient	c_0	3017	$\mathrm{J\,kg}^{-1}\,\mathrm{K}^{-1}$
Heat transfer constant	c_1	-0.0042	K^{-1}
Blood density	ρ_b	1050	$\mathrm{kg\,m}^{-3}$
Blood perfusion rate	ω_b	0.0371	s^{-1}
Blood specific heat	c_b	3617	$\mathrm{J\,kg}^{-1}\,\mathrm{K}^{-1}$
Metabolic term	Q_m	33800	$\mathrm{W\,m}^{-3}$
Cell-death Model			
Frequency factor N $\longrightarrow$ U ($\mathrm{T} \leq 55\,^\circ\mathrm{C}$)	A_1	$8.87 \cdot 10^{73}$	s^{-1}
Frequency factor N $\longrightarrow$ U ($\mathrm{T} > 55\,^\circ\mathrm{C}$)	A_1	$3.56 \cdot 10^{22}$	s^{-1}
Frequency factor U $\longrightarrow$ D	A_2	$5.35 \cdot 10^{11}$	s^{-1}
Frequency factor U $\longrightarrow$ N	A_3	$1.6 \cdot 10^{15}$	s^{-1}
Activation energy N $\longrightarrow$ U ($\mathrm{T} \leq 55\,^\circ\mathrm{C}$)	$\Delta\mathrm{E}_1$	$4.676 \cdot 10^5$	$\mathrm{J\,mol}^{-1}$
Activation energy N $\longrightarrow$ U ($\mathrm{T} > 55\,^\circ\mathrm{C}$)	$\Delta\mathrm{E}_1$	$1.447 \cdot 10^5$	$\mathrm{J\,mol}^{-1}$
Activation energy U $\longrightarrow$ D	$\Delta\mathrm{E}_2$	$8.59 \cdot 10^4$	$\mathrm{J\,mol}^{-1}$
Activation energy U $\longrightarrow$ N	$\Delta\mathrm{E}_3$	$1.051 \cdot 10^5$	$\mathrm{J\,mol}^{-1}$

Figure 6.2(b) summarizes the thermal boundary conditions applied to the computational domain. A constant temperature $\mathrm{T}_0 = 37\,^{\circ}\mathrm{C}$ was prescribed on the outer boundaries of the cardiac tissue Γ_{D}, reproducing physiological basal conditions representative of normothermic myocardium. Along the catheter–tissue interface Γ_{N}, a homogeneous Neumann condition was enforced, expressed as $\mathbf{k}(\mathrm{T})\nabla\mathrm{T}\cdot\mathbf{n} = 0$ to model thermal insulation and prevent artificial heat flux through the applicator boundary. At the upper surface of the domain Γ_{R}, a Robin boundary condition was imposed to mimic the cooling effect of the circulating blood, which continuously removes heat from the endocardial surface: $\mathbf{k}(\mathrm{T})\nabla\mathrm{T}\cdot\mathbf{n} = h_T(\mathrm{T}-\mathrm{T}_{\mathrm{b}})$. This mixed condition balances conductive and convective heat transfer, thereby ensuring a realistic representation of the thermal exchange between the heated tissue and the blood pool. Such boundary treatment is particularly relevant in cardiac ablation modeling, as it captures the influence of perfusion-driven cooling on lesion formation and temperature distribution during and after energy delivery. To sum up:

$$\begin{cases} \mathrm{T} = \mathrm{T}_0 & \text{on } \Gamma_{\mathrm{D}} \\ \mathbf{k}(\mathrm{T})\nabla\mathrm{T}\cdot\mathbf{n} = 0 & \text{on } \Gamma_{\mathrm{N}} \\ \mathbf{k}(\mathrm{T})\nabla\mathrm{T}\cdot\mathbf{n} = h_T(\mathrm{T}-\mathrm{T}_{\mathrm{b}}) & \text{on } \Gamma_{\mathrm{R}} \end{cases} \tag{6.9}$$

The thermal convective coefficient h_T at the blood-tissue surface is calculated according to [162]:

$$w = \left(\frac{h_T}{h_{\mathrm{ref}}}\right)^{1.25} w_{\mathrm{ref}} \tag{6.10}$$

where w is the blood velocity in the cardiac chamber, $w_{\mathrm{ref}} = 24\,\mathrm{cm\,s^{-1}}$ is the reference blood velocity measured inside the cardiac chamber, and $h_{\mathrm{ref}} = 1417\,\mathrm{W\,m^{-2}\,K^{-1}}$ is the reference convective coefficient obtained from w_{ref}. We considered $h_T = 265\,\mathrm{W\,m^{-2}\,K^{-1}}$ for low blood flow where $w = 3\,\mathrm{cm\,s^{-1}}$.

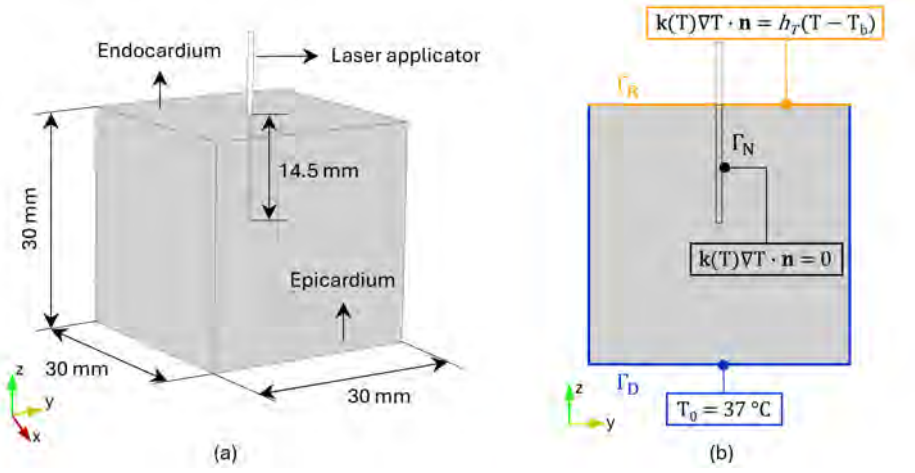

Figure 6.2: (a) Cardiac computational domain. The laser applicator is inserted for 14.5 mm within the domain. (b) Thermal boundary conditions. Thermal insulation is considered at the laser-catheter boundary. A Robin condition is imposed on the blood-endocardial surface. A Dirichlet condition is enforced to the surrounding boundaries.

6.1.4 Convergence Analysis

The idealized cardiac domain was discretized using tetrahedral finite elements, resulting in a computational grid composed of 180 737 elements and 30 111 nodes. The mesh was designed to ensure an optimal balance between numerical accuracy and computational efficiency, with a non-uniform spatial resolution tailored to the expected thermal and optical gradients.

As shown in Figure 6.3, a progressive mesh refinement strategy was implemented within a spherical region surrounding the laser applicator, where the most intense laser–tissue interactions and highest temperature variations occur. In this region, the element size ranged from a maximum of $1 \cdot 10^{-3}$ m in the outer domain to a minimum of $4.6 \cdot 10^{-4}$ m near the irradiated zone. This adaptive meshing approach enhances the resolution of the optical absorption and heat diffusion fields without incurring excessive computational costs across the entire domain.

To further capture the localized thermal phenomena near the laser tip, where the energy deposition is sharply peaked and temperature gradients are steepest, an additional layer of fine mesh refinement was introduced. In this subregion, element sizes were reduced to a maximum of $6.5 \cdot 10^{-5}$ m and a minimum of $1 \cdot 10^{-5}$ m, which approximately corresponds to the characteristic dimension of a cardiac cell. This high-resolution discretization ensures that microscale heat propagation and localized tissue heating are accurately represented, allowing a faithful reproduction of the sharp temperature fronts that define the ablation zone.

Such a multi-scale meshing strategy is particularly critical in laser ablation modeling, where the optical energy is highly localized, and the resulting temperature field exhibits exponential spatial decay. The adopted mesh refinement ensures both numerical stability of the implicit time-stepping scheme and convergence of the computed thermal fields, thus enabling reliable estimation of lesion size and shape under physiological boundary conditions.

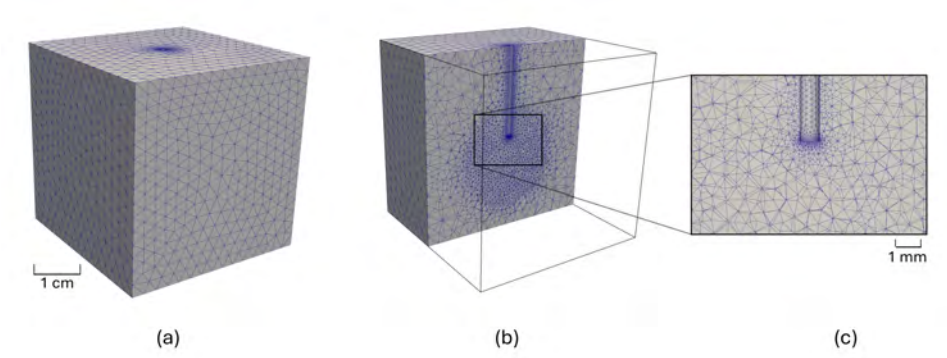

Figure 6.3: Computational mesh adopted for the cardiac laser ablation model. The idealized three-dimensional cardiac domain was discretized using unstructured tetrahedral finite elements generated in *SALOME ®9.11.0*. A progressive refinement strategy was applied, with finer elements surrounding the laser applicator to accurately resolve the steep thermal and optical gradients.

A numerical convergence analysis was performed for all three thermal formulations: Fourier, GF, and DPL, to ensure that the computational comparison remained independent of the underlying discretization and numerical approximation.

This validation step was crucial to confirm that the observed differences among the models arise from their intrinsic physical formulations rather than from mesh resolution or time-stepping effects. The convergence study focused primarily on two key observables, both at the end of the ablation process ($t = 30\,s$): the peak temperature evolution T_{max} at selected monitoring points within the ablation zone, and the thermal damage volume V_d, defined as the region exceeding the critical threshold of $T > 50\,°C$ for irreversible injury.

Subsequently, the polynomial interpolation degree of the finite element basis functions was systematically varied, from P1 (linear) to P2 (quadratic) and P3 (cubic), to evaluate the sensitivity of the numerical solution to the spatial approximation order. This analysis provides insight into the trade-off between solution accuracy and computational cost, since higher-order elements can more accurately capture steep temperature gradients near the laser applicator, albeit at the expense of increased degrees of freedom and longer assembly and solution times. Figure 6.4 displays the temporal evolution of the peak temperature predicted by the DPL formulation, along with the corresponding thermal damage volume at $t = 30\,s$ for each interpolation order. A similar convergence behavior was observed for the Fourier and GF models, with comparable trends in both peak temperature stabilization and lesion volume estimation across the tested polynomial degrees. For further details, please refer to [163].

When analyzing the thermal damage distribution obtained using P1 (linear) elements, it becomes apparent that the predicted temperature field exhibits an unrealistic spatial spread. The temperature rise is correctly centered below the laser applicator, yet the surrounding region near the applicator tip is also markedly affected, showing an extensive heating zone that does not correspond to the expected physical behavior. This artifact arises from the limited interpolation capability of linear elements, which are unable to accurately resolve the steep thermal gradients generated in the focal region. As will be demonstrated in Section 6.2.1, the radiance field, the principal source term driving tissue heating, is highly localized beneath the laser tip, with negligible lateral diffusion at optical scales. Therefore, the broad thermal footprint observed with the P1 discretization must be regarded as numerically induced rather than physically meaningful.

The outcomes of the convergence analysis are summarized in Table 6.2. For each thermal model and interpolation degree, the percentage deviation of both the peak temperature and the thermal damage volume was quantified with respect to the P3 (cubic) solution, which served as the reference. The analysis clearly indicates that increasing the polynomial degree from P1 to P2 and P3 yields substantial improvements in both the amplitude and spatial accuracy of the temperature field. The P1 approximation systematically overestimates the maximum temperature and the extent of thermal damage, highlighting its inadequacy in capturing the anisotropic and highly nonlinear nature of heat transfer in cardiac tissue. Conversely, the P2 discretization produces consistent results, with relative errors below 1 % for all evaluated indicators. On this basis, P2 elements were selected for all subsequent simulations, providing an optimal balance between computational efficiency and numerical accuracy. This choice ensures stable convergence of the thermal field while maintaining sufficient spatial resolution to resolve localized heating and temperature-dependent conductivity effects within the myocardium.

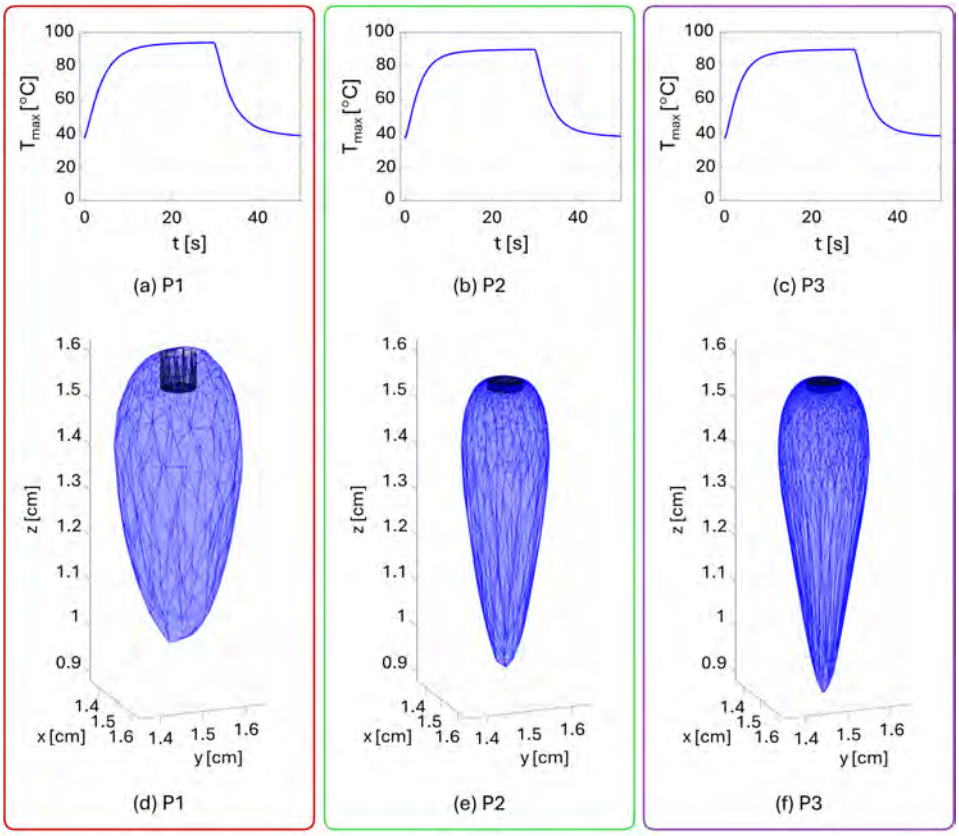

Figure 6.4: Convergence analysis on DPL model. The upper panels show the maximum temperature T_{max} evolution over time for P1 (a), P2 (b) and P3 (c) elements. In the bottom panels the thermal volume damage at t = 30 s for P1 (d), P2 (e) and P3 (f) elements are displayed.

Table 6.2: Convergence analysis indicators: maximum temperature T_{max} and thermal damage volume V_d (T > 50 °C) at the end of the ablation procedure at t = 30 s. The percentage error is evaluated by comparing the P1-P3 and P2-P3 values.

		Fourier	e%	**GF**	e%	**DPL**	e%
T_{max} [°C]	P1	93.307	4.319	93.134	4.250	93.754	4.452
	P2	89.476	0.036	89.374	0.041	89.746	0.013
	P3	89.444		89.337		89.758	
V_d [mm^3]	P1	22.492	116.8	21.975	116.05	23.991	115.44
	P2	10.289	0.8	10.106	0.6	10.829	0.8
	P3	10.372		10.171		10.914	

6.2 Results

The post-processing and visualization of the numerical results were carried out using *Paraview ®5.11.1* in combination with MATLAB, enabling both volumetric rendering of the simulated fields and quantitative analysis of spatial and temporal data. The outputs of the optical and thermal solvers were exported from FEniCSx and subsequently processed to compute derived quantities such as fluence rate distributions, temperature evolution curves, and local cell viability metrics. All simulations were performed according to a standardized cardiac ablation protocol, consisting of an energy delivery phase of 30 s at a laser power of 3 W, followed by a thermal relaxation phase of 270 s in which no active energy source is applied. During the ablation phase, the absorbed laser power acts as the source term in the bioheat equation, inducing a progressive temperature rise within the tissue volume directly beneath the laser applicator. In the subsequent cooling phase, heat diffusion and convective exchange with the surrounding environment drive the system toward equilibrium, leading to a steady-state configuration for both the temperature field and the state variables of the three-state cell death model.

6.2.1 Radiance

The radiance field, computed through the ODA model, serves as the foundation for understanding the spatial distribution of absorbed energy within the myocardial tissue. In cardiac ablation, radiance directly determines the pattern of optical power deposition, which in turn governs the thermal source term $\mathrm{Q_s} = \mu_a \varphi$ in the heat transfer equations. The spatial distribution of the radiance field is illustrated in Figure 6.5. Panel (a) displays the entire computational domain, while panel (b) provides a magnified view of the region surrounding the laser applicator tip, where the optical power deposition is concentrated.

The results reveal a highly localized fluence rate distribution, with energy predominantly confined to the volume directly beneath the laser tip. The fluence rate reaches a maximum value of approximately $2.7 \cdot 10^7\,\mathrm{W\,m^{-2}}$, decaying exponentially with increasing depth into the cardiac tissue. This attenuation pattern reflects the strong scattering and weak absorption characteristics of myocardial tissue in the near-infrared spectral range employed, consistent with previously reported optical parameters for cardiac muscle [154]. As shown in Figure 6.5(b), the light fluence decreases by nearly two orders of magnitude within a few millimeters from the source, generating a narrow and axially elongated energy deposition region. This behavior is in line with the theoretical predictions of the Beer–Lambert law under diffusive conditions, confirming the validity of the ODA approximation in capturing the essential features of laser–tissue interaction.

The optical energy distribution defines the primary heat source in the coupled optical–thermal model, directly influencing the subsequent temperature and damage fields. Specifically, the volumetric heat source term $\mathrm{Q_s} = \mu_a \varphi$ mirrors the shape of the radiance pattern, resulting in a localized heating zone with a steep axial temperature gradient and a radially confined thermal footprint. This spatial confinement of energy absorption is a key factor in achieving controlled ablation, minimizing collateral damage to the surrounding myocardium while ensuring effective lesion formation in the targeted area. Overall, the computed radiance field provides a clear quantitative representation of how laser energy is absorbed and diffused within anisotropic cardiac tissue. It serves as the starting point for the

subsequent analysis of temperature evolution and thermal damage, establishing the link between the optical properties of the myocardium and the resulting biothermal response during laser ablation.

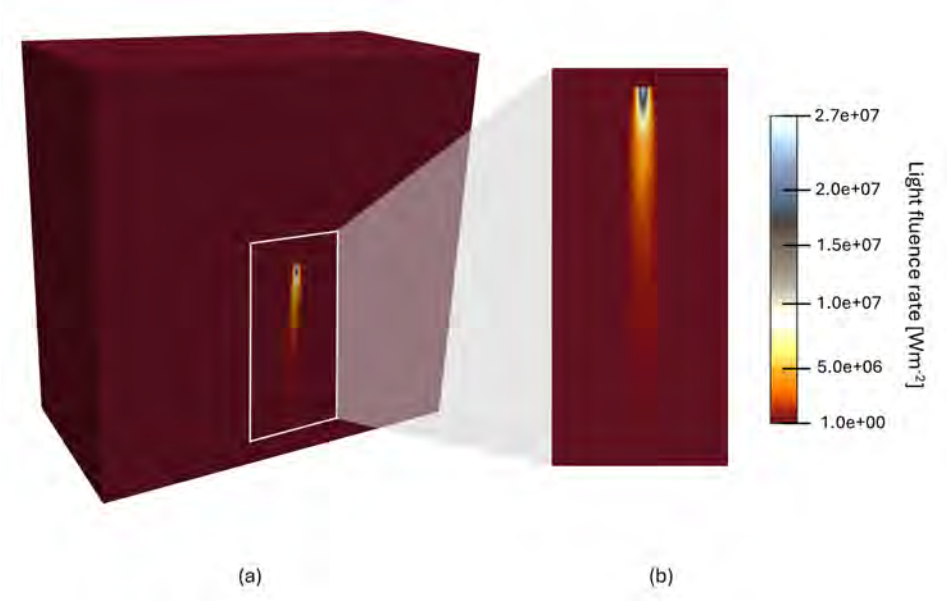

Figure 6.5: (a) Three-dimensional view of the computational domain showing the simulated light fluence rate distribution. (b) Magnified section around the laser applicator tip, highlighting the highly localized energy deposition region. The color bar represents the fluence rate (in $\mathrm{W\,m^{-2}}$), with the peak intensity concentrated immediately below the applicator.

6.2.2 Time Constant Analysis

A parametric analysis was performed to investigate the influence of the relaxation time constants on the temperature evolution predicted by the three thermal formulations. In particular, the thermal relaxation time τ_t and the heat flux time lag τ_q were treated as key parameters governing the transient response in the GF and DPL models, respectively. The results of this analysis are reported in Figure 6.6.

Panel (a) identifies three monitoring points (A, B, and C) selected within the cardiac domain. Point A is positioned 1 mm below the laser tip, corresponding to the region of maximum energy deposition; point B lies along the same vertical (z-axis) direction, 3 mm beneath the laser surface; and point C is located laterally, 1 mm away from point B in the y-direction. These locations were chosen to capture both the axial decay of the temperature field and the radial diffusion away from the irradiated zone. Panels (b–f) display the temporal evolution of temperature at these three locations for the Fourier, GF, and DPL formulations, respectively. In all models, a consistent trend is observed: the temperature rises during the laser-on phase (0 – 30 s) and reaches its peak value at the end of irradiation, followed by a cooling phase lasting approximately 20 s until the system returns to equilibrium. However, notable differences emerge among the models regarding both the transient dynamics and the post-ablation relaxation behavior. The Fourier model, Figure

6.6(b) exhibits the classical behavior associated with instantaneous heat propagation, characterized by a rapid temperature rise and an equally abrupt decay after the energy source is removed. This results in high peak temperatures at all monitored points, particularly near the applicator (point A), but fails to reproduce the finite propagation speed of heat waves observed in real tissue. In contrast, the GF model, Figure 6.6(c) introduces a single time constant τ_t to account for finite thermal response effects. Three representative cases were analyzed, corresponding to $\tau_t = 0.05$, 2 and 5 s [164, 165]. As τ_t increases, the temperature curves display a smoother transition toward the steady-state plateau at the end of the ablation phase, with the initial overshoot or hump progressively diminishing. Conversely, for smaller τ_t values, this hump becomes more pronounced, reflecting a sharper and more localized transient response that approximates the classical Fourier limit as $\tau_t \to 0$. The DPL model, Figure 6.6(d-f) further extends this framework by introducing two distinct lag times, τ_t and τ_q, which independently control the temperature response delay and the heat flux relaxation. This dual-lag formulation captures more complex heat transfer mechanisms, such as phase-lagged flux propagation and delayed diffusion, which are particularly relevant at short timescales or under rapid energy deposition. Nine computational experiments were conducted by combining the three previously used values of $\tau_t = 0.05$, 2 and 5 s with three different τ_q values, namely $\tau_q = 2$, 4 and 8 s [166].

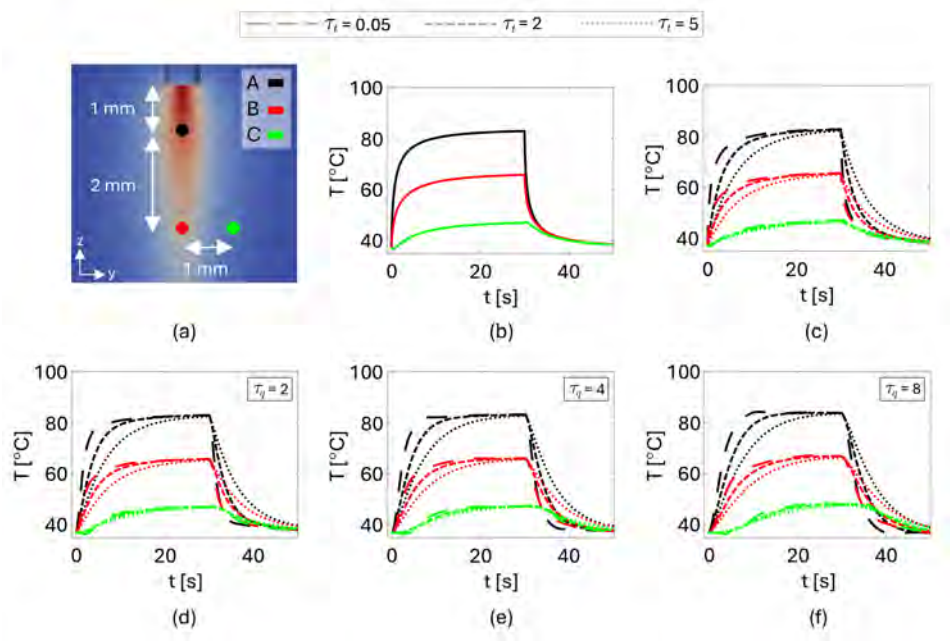

Figure 6.6: (a) Schematic representation of the selected monitoring points A, B, and C within the computational domain. (b) Temperature evolution for the Fourier model. (c) Temperature evolution for the GF model with $\tau_t = 0.05$, 2 and 5. (d–f) Temperature evolution for the DPL model for different combinations of $\tau_t = 0.05$, 2 and 5 s and $\tau_q = 2$, 4 and 8 s. Points closer to the laser tip exhibit higher peak temperatures, while larger lag times lead to prolonged cooling phases and smoother transient behavior, consistent with delayed heat diffusion mechanisms.

Overall, this parametric investigation confirms that while the Fourier model provides a baseline prediction characterized by idealized instantaneous diffusion, the GF and DPL models offer a more realistic representation of thermal inertia in biological tissues. In particular, the DPL formulation, through the combined effect of τ_t and τ_q, successfully captures the finite-speed propagation and temporal lag of thermal flux, phenomena that are essential for accurately modeling laser ablation in anisotropic cardiac tissue.

6.2.3 Anisotropy analysis

The following analysis investigates the effect of tissue anisotropy on the optical–thermal response of the myocardium. Cardiac tissue exhibits a highly organized microstructure, characterized by fiber bundles with preferential orientations that govern the directionality of both electrical and thermal conduction. This structural anisotropy plays a crucial role in the spatial distribution of heat during laser ablation, potentially altering the shape and extent of the lesion compared to isotropic assumptions. To assess the model sensitivities to the degree of anisotropy, three numerical simulations, for each model, were performed by varying the thermal conductivity ratio $k_{ratio} = k_f/k_f$ where k_f and k_t denote the conductivity along and across the myocardial fibers, respectively. The selected ratios, k_{ratio}= 1, 2, and 5, represent increasing levels of anisotropy, consistent with experimental and computational data reported for cardiac tissue [133].

Figure 6.7 illustrates the DPL resulting temperature fields and the thermal damage volumes, defined as regions exceeding the 50 °C isotherm, for the three anisotropy configurations. The top panels provide 3D isothermal surfaces, while the bottom panels show longitudinal cross-sections of the ablated volume. Under isotropic conditions, k_{ratio}= 1, Figure 6.7(a), the thermal lesion assumes a symmetric, axially elongated shape centered along the laser propagation axis, consistent with a uniform diffusion of heat in all directions. As the anisotropy ratio increases, k_{ratio}= 2 and 5, Figure 6.7(b-c), a distinct spatial distortion of the lesion becomes evident. The thermal field develops an elliptical curling pattern, with a noticeable reduction of the temperature penetration depth along the z-axis and a concomitant lateral widening in the transverse plane. This phenomenon results from the higher thermal conductivity along the myocardial fibers, which promotes preferential heat spreading parallel to the fiber orientation while reducing vertical diffusion beneath the applicator. Consequently, less heat is dissipated in depth, leading to a localized accumulation of energy near the laser tip and a shallower lesion morphology. These findings are in strong agreement with both experimental measurements and multiphysics modeling of cardiac ablation [133], confirming that anisotropy can significantly affect lesion geometry and treatment selectivity. In physiological terms, this effect implies that the thermal footprint of the ablation may follow the myocardial fiber orientation, thereby influencing the effective targeting of arrhythmogenic substrates. It is worth noting that this analysis revealed no significant discrepancies among the three thermal formulations (Fourier, GF, and DPL) in terms of overall temperature distribution or ablated volume. Instead, the anisotropy ratio k_{ratio} emerged as the dominant parameter influencing the spatial characteristics of heat diffusion and lesion morphology. For illustrative purposes, only the results obtained with the DPL model are presented here, as they are representative of the trends observed across all formulations. For further details and extended comparative results, refer to [163].

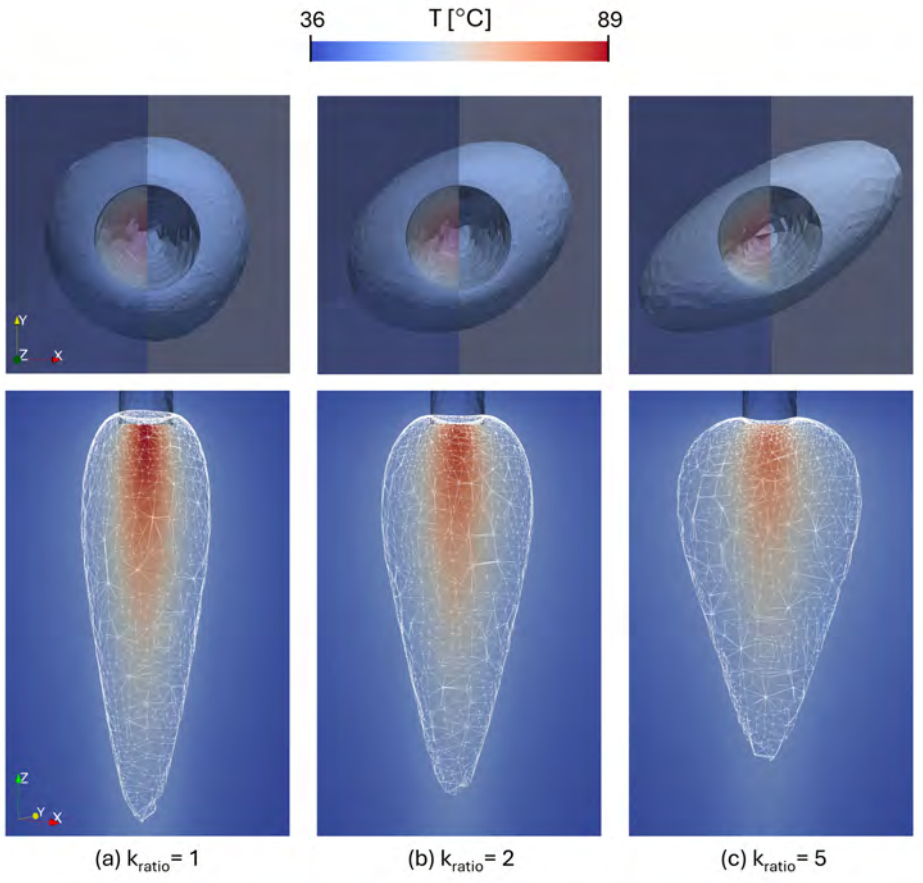

Figure 6.7: Temperature distributions and corresponding ablated volumes ($T > 50\,^{\circ}C$) obtained with the DPL model for different anisotropy ratios. (a) Isotropic case ($k_{ratio} = 1$); (b) moderate anisotropy ($k_{ratio} = 2$); (c) strong anisotropy ($k_{ratio} = 5$). Increasing anisotropy produces a visible lateral widening and a reduction in lesion depth, with a curling effect of the isothermal surfaces due to preferential heat conduction along myocardial fibers.

6.2.4 Thermal Damage

A deeper investigation of the ablation-induced lesion dynamics was carried out to quantify the extent and temporal evolution of tissue damage predicted by the different heat transfer models. The analysis integrates both classical temperature-based criteria and the three-state cellular death model, providing a more comprehensive interpretation of irreversible injury development in cardiac tissue.

Within the three-state framework, the native cellular state (N) serves as a reference variable, where the threshold condition $N \leq 0.8$ identifies irreversible thermal damage and delineates the lesion boundary. This criterion is compared to the conventional thermal approach based on the $50\,^{\circ}C$ isotherm, widely adopted as a surrogate indicator of necrosis in hyperthermic therapies [132, 157].

Figure 6.8 presents the temporal evolution of the damage volume computed

over five minutes of simulation for the Fourier, GF, and DPL models. Two sets of curves are reported: those based on the temperature isotherm criterion (T = 50 °C) and those derived from the cell viability threshold (N = 0.8). All simulations follow the same energy delivery protocol: 30 °C of laser heating at 3 W followed by a 270 s relaxation phase, allowing direct comparison of thermal and biological responses under identical conditions.

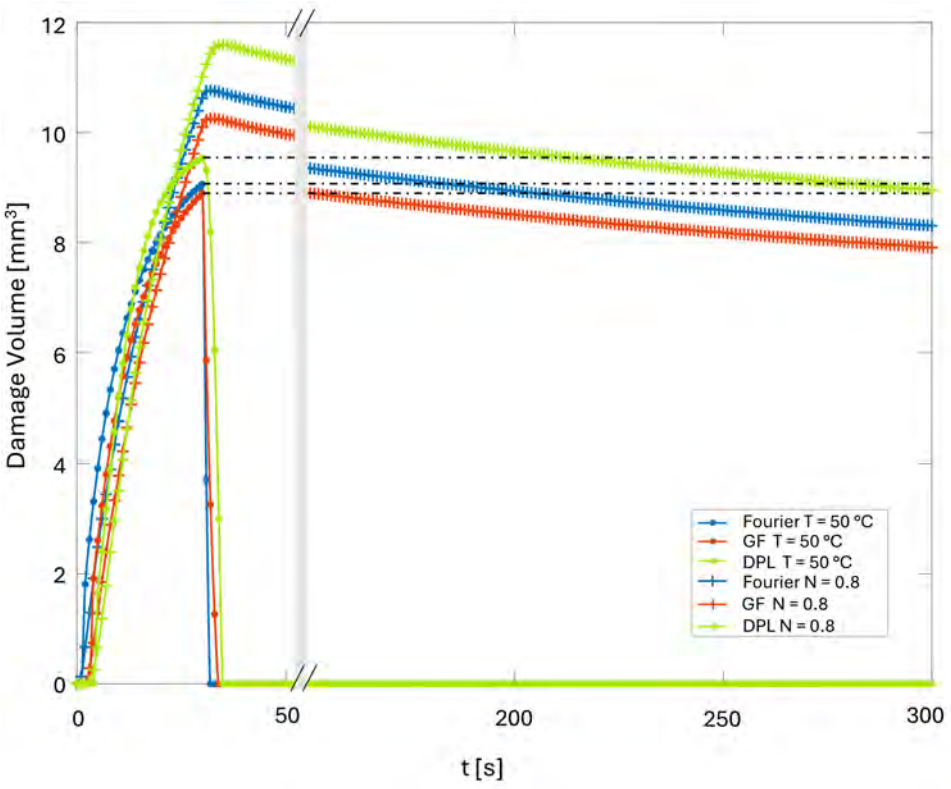

Figure 6.8: Temporal evolution of the thermal damage volume predicted by the Fourier, GF, and DPL models during laser ablation and post-ablation relaxation. Comparison between the isothermal criterion (T = 50 °C) and the three-state cell death threshold (N = 0.8). The curves show an initial rapid increase during energy delivery followed by a relaxation phase in which the cellular-based damage gradually converges to the isothermal value.

During the ablation phase, the lesion volume increases rapidly, mirroring the evolution of the temperature field. Following the T = 50 °C criterion, at t = 30 s, corresponding to the end of energy delivery, the maximum damage volumes are approximately 9.1 mm^3, 8.9 mm^3 and 9.5 mm^3 for the Fourier, GF, and DPL formulations, respectively. These minor discrepancies confirm that the three heat transfer models produce comparable predictions under quasi-steady heating conditions.

The subsequent cooling and relaxation period reveals a more complex dynamic behavior. The damage volume estimated through the cellular state variable (N = 0.8) initially exceeds the corresponding isothermal damage at the end of ablation, indicating that cell death continues even after the energy source is deactivated,

a phenomenon consistent with thermal latency and delayed protein denaturation processes [138]. However, as the tissue gradually cools, partial recovery of the reversible fraction (U) occurs, leading to a slow reduction in the damage volume until convergence with the 50 °C isothermal estimate.

This volume relaxation occurs at different times depending on the thermal model: specifically, at 184.5 s for the Fourier, 151.4 s for GF, and 214.3 s for DPL models. The delayed equilibration observed in the DPL formulation reflects its intrinsic ability to capture finite-speed heat propagation and thermal memory effects, resulting in a prolonged redistribution of residual heat within the tissue.

To quantify the variation between the two damage estimators, the percentage change in thermal damage volume ($V_{\%}$) was computed by comparing the isothermal damage at t = 30 s with the reference volume V_{ref}, defined as the final stabilized value of the cellular-based damage (N = 0.8) at t = 300 s. These results, summarized in Table 6.3, highlight a consistent overestimation of damage when relying solely on the 50 °C isotherm, especially during the early post-ablation stage.

In particular, the DPL model exhibits a clear trend inversion (as further detailed in Figure 6.9): immediately after the ablation phase (t = 30 s), the lesion volume predicted by the cellular criterion ($V_{N=0.8}$) exceeds the 50 °C-based estimate ($V_{T=50°C}$); conversely, by the end of the relaxation period (t = 300 s), the situation reverses, with $V_{T=50°C}$ becoming slightly larger than $V_{N=0.8}$. This crossover highlights the dynamic interplay between thermal exposure and biological recovery, illustrating that tissue necrosis cannot be fully captured by a static temperature threshold.

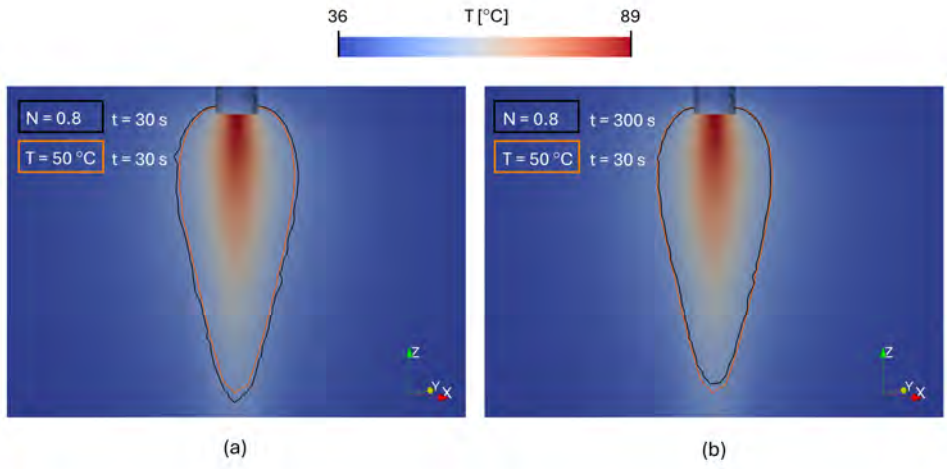

Figure 6.9: Comparison between the damage volumes estimated through the three-state cell death model (N = 0.8) and the 50 °C isothermal criterion for the DPL formulation. In the DPL we set k_{ratio} = 2, τ_q= 4 s and τ_t= 2 s. Panel (a) shows the ablated region at the end of the laser-on phase (t = 30 s), where the cellular-based damage volume exceeds the isothermal estimate, indicating ongoing cell death beyond the thermal front. Panel (b) illustrates the same comparison after the relaxation phase (t = 300 s): as the tissue cools, the three-state model predicts a reduction of the damaged region due to the partial recovery of reversibly injured cells, while the 50 °C isothermal contour remains unchanged. This illustrates the ability of the cellular model to capture post-ablation recovery phenomena and delayed thermal response in myocardial tissue.

Table 6.3: Thermal damage volume change. V_{ref} is the volume damage considering the three-state threshold N = 0.8 at t = 30 s. The volume percentage change $V_{\%}$ is calculated considering the damage volume of T = 50°C isotherm at t = 30 s with respect to V_{ref}.

	Fourier	**GF**	**DPL**
V_{ref} [mm^3] (N = 0.8)	8.3077	7.91474	8.9575
$V_{\%}$ ($V_{T=50°C}$ vs V_{ref})	+9.1 %	+12.4 %	+6.5 %

We conclude by analyzing the temporal evolution of the native N, unfolded U, and denatured D fractions predicted by the three-state model of thermal injury. Figure 6.10 reports the time courses at the three monitoring locations defined in Figure 6.6(a), for the Fourier (a), GF (b), and DPL (c) heat-transfer formulations. Simulations start from the common physiological initial condition N = 1, U = 0, D = 0, and are followed for five minutes, long enough to observe asymptotic behavior.

At the point closest to the applicator (A), all models exhibit the canonical sequence: a rapid fall of N, a transient rise of U, and a monotonic increase of D until saturation, consistent with strong local heating during the 30 s laser-on phase and subsequent stabilization during relaxation. Moving axially away from the source (B), the same qualitative pattern is preserved but with attenuated amplitudes and delayed extrema, reflecting the reduced optical source term and slower local thermal buildup. At the lateral location (C), the temperature exposure remains below the critical injury threshold, and the dynamics are correspondingly muted: N stays near unity, U shows only a small transient shoulder, and D remains minimal.

A systematic temporal shift is apparent when comparing the three thermal models, particularly at A and B: the GF and DPL curves are displaced relative to the Fourier ones. This phase shift arises from the lag parameters embedded in the GF (τ_t) and DPL (τ_t and τ_q) formulations, which endow the system with finite-speed thermal response and flux relaxation. As a result, peak U and the inflection of N and D occur later than in the instantaneous-diffusion Fourier case, and the post-ablation approach to steady state is more gradual. Despite these timing differences, the three formulations converge to comparable end-states at each location, consistent with the similar damage volumes reported in the previous section.

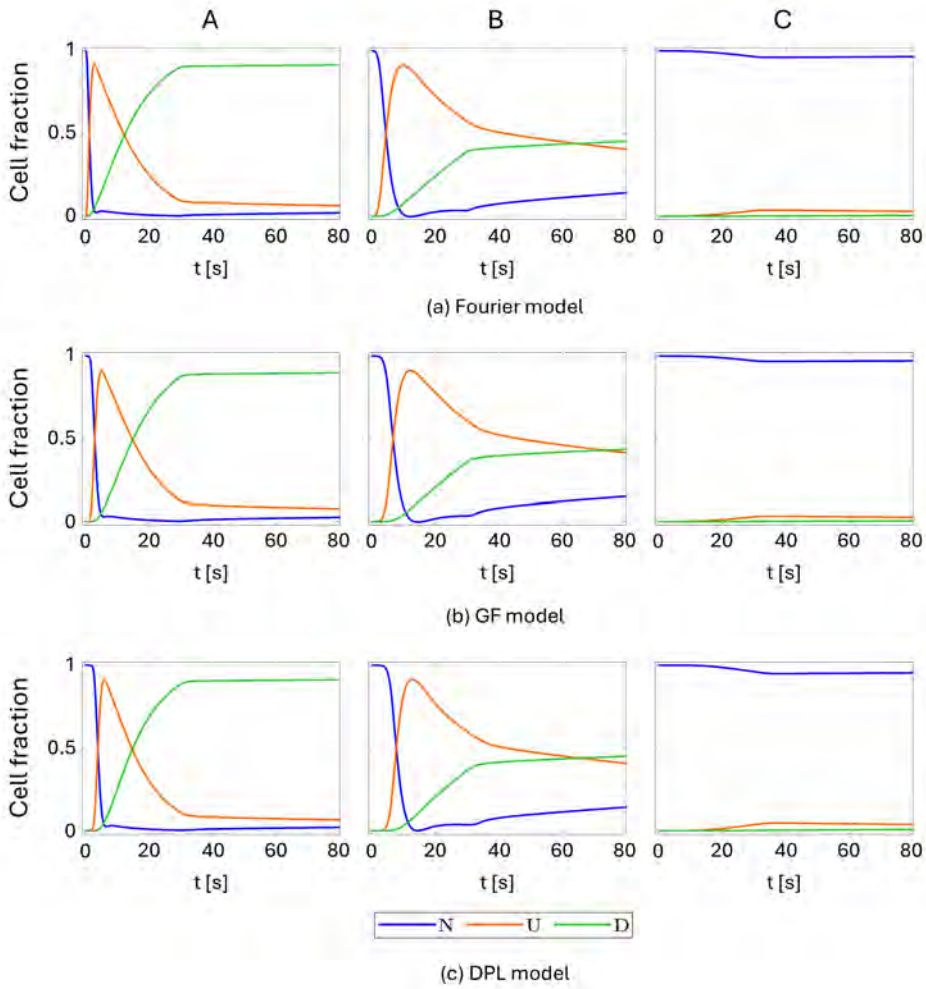

Figure 6.10: Temporal evolution of the three-state cell death model variables: native N, unfolded U, and denatured D, during a 30 s laser ablation followed by a relaxation phase, evaluated at three representative locations (A, B, and C) within the cardiac domain (see Figure 6.6(a)). Panels (a), (b), and (c) correspond to the Fourier, GF, and DPL thermal formulations, respectively. Closer to the laser applicator (points A and B), a rapid decrease in N and a corresponding increase in D are observed, while farther regions (point C) remain largely unaffected due to lower temperature exposure. The GF and DPL models exhibit a temporal delay in the evolution of the state variables compared to the Fourier model, reflecting the influence of their intrinsic relaxation times on the heat propagation and cellular response dynamics.

7

Nanoparticle-mediated Laser Ablation Modeling

After establishing the theoretical framework for light propagation and heat transfer in biological tissues in Chapter 5, and following the computational development of cardiac laser ablation presented in Chapter 6, the focus now shifts toward modeling nanoparticle-laser ablation. In this context, the computational approach serves as a bridge between theory and experimentation, enabling a deeper understanding of the physical mechanisms observed in the Experimental Activities.

As explained in Section 2.2, gold nanostructures exhibit LSPR when irradiated in NIR, which markedly amplifies optical absorption and heat generation within their surrounding medium. Incorporating these plasmonic effects into a coupled optical–thermal model allows quantifying how nanoparticle concentration, geometry, and distribution influence the spatiotemporal temperature field and the resulting thermal damage.

The following sections present the development of this nanoparticle-mediated ablation model, formulated to reproduce the experimental conditions and to investigate the underlying dynamics of energy deposition, heat diffusion, and tissue response. Through this computational framework, the study provides predictive insight into the mechanisms governing plasmonic-assisted heating and supports the optimization of selective, localized laser ablation strategies.

7.1 NPs-mediated LA computational modeling

The computational framework developed for the nanoparticle-mediated ablation relies on the ODA model (5.2). In the present case, the ODA model is adapted to account for the additional optical contribution of gold nanoparticles, which act as localized absorbers embedded within the tissue matrix. Their presence modifies the effective absorption coefficient of the medium, leading to a locally enhanced volumetric heat generation term. The total absorption coefficient, therefore, becomes the sum of two components: the intrinsic tissue absorption, dependent on the optical properties of the native medium, and the plasmonic absorption associated with the nanoparticles. This modification enables the model to capture the localized enhancement of electromagnetic energy deposition arising from the exci-

tation of the nanoparticles' surface plasmon resonance. Accordingly, in (5.2), the diffusion, absorption and scattering coefficients, D, μ_a and μ_s are redefined as total coefficients, incorporating both the native tissue contribution and the additional effect induced by the presence of nanoparticles. Hence, they can be expressed as:

$$D_{\text{tot}} = \frac{1}{3}\left(\mu_{a,\text{tot}} + \mu'_{s,\text{tot}}\right) \tag{7.1}$$

$$\mu_{a,\text{tot}} = \mu_{a,m} + \mu_{a,\text{NP}} \tag{7.2}$$

$$\mu'_{s,\text{tot}} = (1-g)\,\mu_{s,\text{tot}} \tag{7.3}$$

$$\mu_{s,\text{tot}} = \mu_{s,m} + \mu_{s,\text{NP}} \tag{7.4}$$

where $\mu_{a,m}$ e $\mu_{s,m}$ are the absorption and scattering coefficients of the medium, respectively. For biological tissues within the NIR region, $\mu_{s,m} \sim 10^2 - 10^3 \mu_{a,m}$. This condition is similarly applicable to agarose-based phantoms, which are predominantly water-based. Following the medium used in our experiments (see Section 4.1), although specific absorption and scattering coefficients for 4 % agarose-phantoms in the NIR region are not readily available, it is reasonable to assume optical properties similar to water. Based on Kruger et al. [167], an initial scattering coefficient of was adopted, while an optimal absorption coefficient of $\mu_{a,m} = 20\,\text{m}^{-1}$ was identified through parametric fitting against experimental temperature profiles in the agarose-phantom. $\mu_{a,\text{NP}}$ and $\mu_{s,\text{NP}}$ are the absorption and scattering coefficients of the NPs volume considered, respectively.

Generalizing, gold nanostructures exhibit a strong absorption cross-section in NIR, associated with the excitation of LSPR, which enhances electromagnetic energy confinement in their vicinity. As a result, even relatively low nanoparticle concentrations can lead to a measurable increase in both absorption and scattering within the composite medium. Quantitatively, the nanoparticle contribution to the absorption and scattering coefficients can be expressed as [168]:

$$\mu_{a,\text{NP}} = 0.75 f_v \frac{Q_a}{r_{\text{eff}}} \tag{7.5}$$

$$\mu_{s,\text{NP}} = 0.75 f_v \frac{Q_s}{r_{\text{eff}}} \tag{7.6}$$

here, f_v is the NPs volume fraction (considering the experimental NPs concentration of $3 \cdot 10^{10}\,\text{NP/mL}$), $Q_a = C_a/a$ and $Q_s = C_s/a$, are the absorption and scattering efficiency factors for a single NP; C_a and C_s are the absorption and scatterng cross-section, respectively, and a the cross-sectional area of the NP. The effective radius r_{eff} corresponds to the radius of a sphere with a volume equivalent to that of the particle with volume V [169]. Therefore, r_{eff} characterizes the volume of the NP and is given by:

$$r_{\text{eff}} = \sqrt[3]{\frac{3V}{4\pi}} \tag{7.7}$$

To sum up, (5.2) becomes:

$$-D_{\text{tot}} \frac{\partial^2 \varphi(z)}{\partial z^2} + \mu_{a,\text{tot}} \varphi(z) = s(z) \tag{7.8}$$

To describe heat transfer during nanoparticle-mediated laser ablation, the DPL model was adopted as the governing thermal formulation. This choice builds upon

the comparative analysis of heat transfer models presented in Chapter 6, where the classical Fourier, GF, and DPL approaches were systematically evaluated under identical boundary and source conditions. The previous investigation demonstrated that, while the Fourier model provides a simple diffusive description, it fails to accurately capture transient thermal responses under rapid heating regimes typical of laser-based ablation. In contrast, the DPL model, by introducing finite propagation effects through two distinct relaxation times, one associated with the heat flux and the other with the temperature gradient, offers a more physically consistent representation of non-Fourier heat transport in biological tissues.

In the present context, the use of the DPL formulation is particularly suitable since the nanoparticle-induced photothermal conversion produces highly localized and short-duration heat sources, where deviations from the classical instantaneous conduction assumption become non-negligible. The model thus enables a more realistic prediction of the spatiotemporal temperature evolution and the extent of thermal damage, aligning with the experimental observations of localized heating around nanoparticle-enriched regions.

In this computational framework, the DPL equation (5.6) that describes the NPs-mediated laser ablation in agarose phantom is mathematically expressed as follows:

$$\tau_{\mathrm{q}}\rho\mathrm{c}\frac{\partial^2\mathrm{T}}{\partial t^2}+\rho\mathrm{c}\frac{\partial\mathrm{T}}{\partial t}=\nabla\cdot(\mathrm{k(T)}\nabla\mathrm{T})+\tau_t\nabla\cdot\left(\mathrm{k(T)}\frac{\partial\nabla\mathrm{T}}{\partial t}\right)+\mathrm{Q_s} \tag{7.9}$$

Specifically, a linear decreasing relation is considered for the thermal conductivity k(T):

$$\mathrm{k(T)}=\mathrm{k_0}(1+\mathrm{k_1}(\mathrm{T}-\mathrm{T_{ext}})) \tag{7.10}$$

with $\mathrm{k_0}$ the thermal conductivity at reference temperature, $\mathrm{k_1}$ a non-dimensional constant gain and $\mathrm{T_{ext}}$ is the environmental temperature.

Compared to (5.6), the $\mathrm{Q_b}$ and $\mathrm{Q_m}$ terms are omitted, as the present model refers to laser ablation in an agarose-based phantom, a synthetic medium that does not exhibit either blood perfusion or metabolic heat generation. Conversely, the source term $\mathrm{Q_s}=\mu_{a,\mathrm{tot}}\varphi$ accounts for the volumetric heat generation induced by the nanoparticles, representing the plasmonic contribution associated with their optical absorption under laser irradiation.
All parameters considered in the models are summarized in Table 7.1.

It is crucial to highlight that the following parameters were subjected to a parametric analysis to refine the computational model using experimental data: absorption C_a and scattering C_s cross-sectional area for the NPs, as well as the time lags τ_q and τ_t.

7.1.1 Computational model implementation

The computational domain was constructed in *SALOME ®9.11.0* [161] to faithfully reproduce the geometry of the experimental setup while omitting the explicit representation of the laser applicator, with a radius of $r_f = 0.4\,\mathrm{mm}$, in order to optimize computational efficiency. The thermal influence of the applicator was instead modeled through appropriate boundary conditions, ensuring accurate heat confinement near the irradiation region without the need for additional meshing complexity.

Table 7.1: Optical and thermal parameters for the NPs-mediated laser ablation computational modeling in NPs-agarose phantom.

Parameter		**Value**	**[u]**
Optical Model			
Agarose absorption coefficient	$\mu_{a,m}$	20	m^{-1}
Agarose scattering coefficient	$\mu_{s,m}$	$10 \cdot 10^{4}$	m^{-1}
Agarose anisotropy factor	g	0.9	
Absorption cross section (NC_1)	C_a	$8 \cdot 10^{-16}$	m^2
Scattering cross section (NC_1)	C_s	$1 \cdot 10^{-16}$	m^2
Absorption cross section (NC_2)	C_a	$2 \cdot 10^{-15}$	m^2
Scattering cross section (NC_2)	C_s	$6.04 \cdot 10^{-16}$	m^2
Absorption cross section (NC_3)	C_a	$1.25 \cdot 10^{-15}$	m^2
Scattering cross section (NC_3)	C_s	$4 \cdot 10^{-16}$	m^2
Absorption cross section (NR)	C_a	$1.8 \cdot 10^{-14}$	m^2
Scattering cross section (NR)	C_s	$1 \cdot 10^{-14}$	m^2
Nanocage lenght	l	40	nm
Thermal Model			
Density	ρ	1000	$\mathrm{kg\,m}^{-3}$
Reference thermal conductivity	k_0	0.587	$\mathrm{W\,m}^{-1}\,\mathrm{K}^{-1}$
Thermal conductivity constant	k_1	0.0028	K^{-1}
Heat transfer constant	c	3900	$\mathrm{J\,kg}^{-1}\,\mathrm{K}^{-1}$
Thermal convective coefficient	h	3	$\mathrm{W\,m}^{-2}\,\mathrm{K}^{-1}$
Time lag heat flux	τ_q	2	s
Time lag temperature gradient	τ_t	8	s

The numerical implementation was carried out using the weak formulation of the coupled optical–thermal problem, following the same discretization scheme and computational strategy previously adopted for the cardiac laser ablation model (Section 6.1.1). The computational domain Ω is defined as the agarose phantom, while its boundary $\partial\Omega$ is decomposed as $\partial\Omega = \Gamma_D + \Gamma_N + \Gamma_R$, where Γ_D, Γ_N and Γ_R denote, respectively, the Dirichlet, Neumann and Robin boundary portions. Specifically, Figure 7.1 illustrates the boundary conditions applied to both the optical (a) and thermal (b) problems. A zero-reflection condition ($\varphi = 0$) was imposed on the external boundaries of the agarose phantom, while a Gaussian laser intensity profile, as described in (5.3), was applied to the laser tip surface to represent the incident optical flux. For the thermal field, a constant temperature boundary condition ($T_{ext} = 20\,°C$ was prescribed on the outer surfaces of the phantom Γ_D, replicating the experimental configuration in which the agarose block was enclosed within a PLA custom holder. The laser applicator surface Γ_N was treated as thermally insulated ($k(T)\nabla T \cdot \mathbf{n} = 0$), while a convective boundary condition $k(T)\nabla T \cdot \mathbf{n} = h_T(T - T_{ext})$ was assigned to the upper surface of the phantom, Γ_R, to account for natural convection between the phantom and the surrounding air:

$$\begin{cases} T = T_{ext} & \text{on } \Gamma_D \\ k(T)\nabla T \cdot \mathbf{n} = 0 & \text{on } \Gamma_N \\ k(T)\nabla T \cdot \mathbf{n} = h(T - T_{ext}) & \text{on } \Gamma_R \end{cases} \tag{7.11}$$

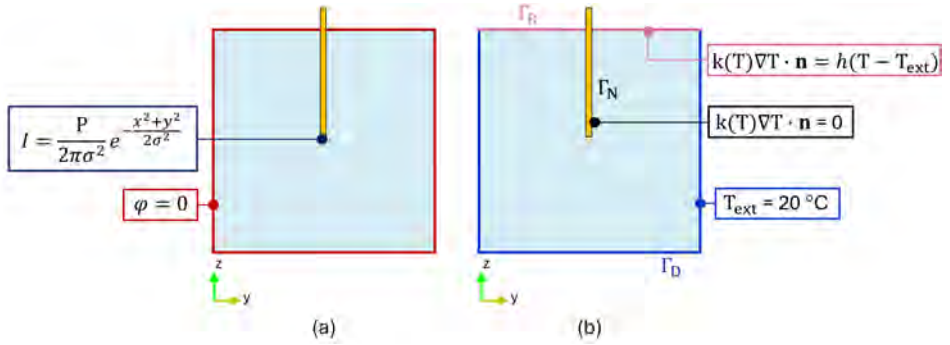

Figure 7.1: Schematic representation of the computational domain and applied boundary conditins for the NPs-mediated laser ablation model. (a) Optical boundary conditions, including the imposed laser intensity distribution and the zero-reflection condition at the phantom boundaries. (b) Thermal boundary conditions showing the decomposition of the domain into Dirichlet, Neumann and Robin regions, reproducing the experimental configuration of the agarose phantom within the PLA custom holder.

The computational mesh consisted of approximately 180,000 tetrahedral finite elements and 30,000 nodes. A progressive mesh refinement strategy was adopted, with denser discretization in the central spherical region expected to experience the most significant laser–tissue interactions. Additional refinement was introduced around the laser tip to ensure high numerical accuracy in regions of steep thermal and optical gradients (Figure 7.2).

The numerical simulations were implemented through a custom Python workflow based on the open-source FEniCSx library [151–153], enabling the coupled

solution of optical and thermal fields. The simulation protocol replicated the experimental conditions, with a laser power of 3 W applied for 120 s, followed by a cooling phase to capture the post-irradiation thermal relaxation dynamics.

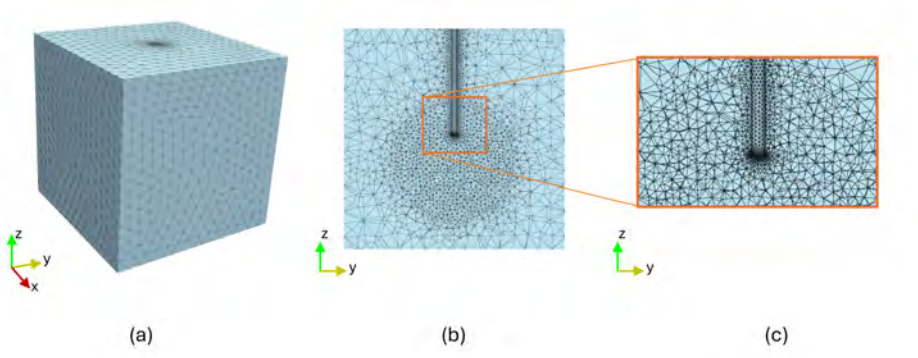

Figure 7.2: Finite element mesh of the computational domain used for the nanoparticle-mediated laser ablation simulations. (a) Overall view of the tetrahedral mesh representing the agarose phantom. (b) Cross-sectional view highlighting the refined central region where the highest energy deposition is expected. (c) Close-up of the mesh refinement around the laser tip, ensuring accurate resolution of optical and thermal gradients.

7.1.2 Results

Before presenting the comparison between experimental measurements and numerical predictions, Figure 7.3 illustrates the spatial arrangement of the four Fiber Bragg Grating sensors selected for the analysis. Although the experimental setup included a larger number of sensing points, the sensors FBG_{A5}, FBG_{B5}, FBG_{C4}, and FBG_{D4} were chosen due to their representative thermal responses and their strategic location with respect to the laser applicator (see the zoom-in in the right panel). A consistent color code is adopted throughout this chapter to identify these sensors in both the experimental temperature curves and the corresponding numerical predictions. In the computational model, the numerical probe points were positioned at the exact spatial coordinates of the FBG sensors in the experimental setup, ensuring full consistency between the measured and simulated datasets. This selection enables a clearer interpretation of the temperature evolution and facilitates a focused comparison between the thermal models.

To assess the accuracy of the proposed thermal modeling framework in the context of nanoparticle-mediated laser ablation, an initial computational–experimental comparison was carried out. All temperature profiles used in this analysis correspond to the mean trends obtained across the experimental campaigns conducted under identical conditions, ensuring robust and representative comparisons between measurements and simulations. Figure 7.4 reports the comparison between the experimental temperature profiles acquired via FBG sensors and the numerical predictions obtained with the Fourier and DPL heat transfer models. Overall, the numerical simulations capture the qualitative evolution observed experimentally: an initial rapid temperature increase during laser irradiation, followed by a quasi-steady plateau, and a subsequent temperature drop once the laser is switched off at $t = 120$ s.

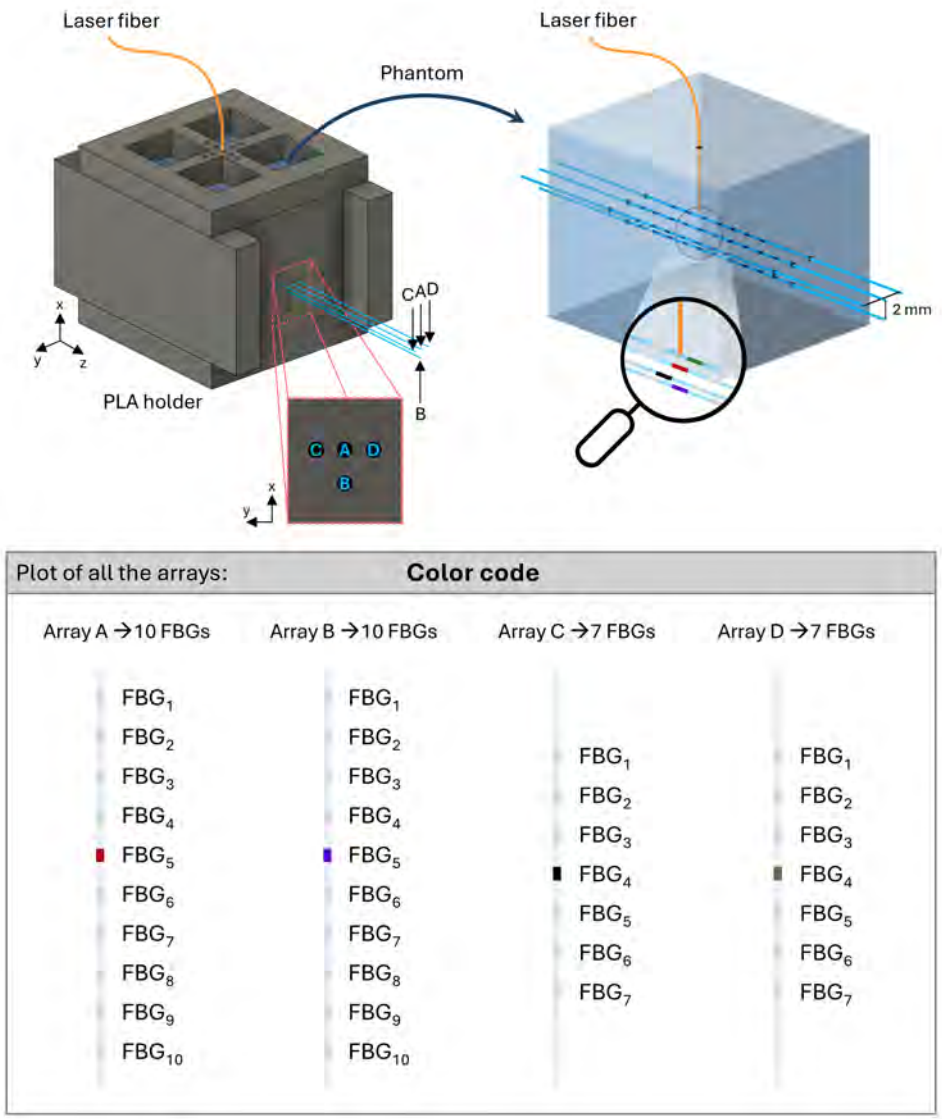

Figure 7.3: Experimental configuration and spatial arrangement of the Fiber Bragg Grating sensors used for temperature monitoring during nanoparticle-mediated laser ablation. The left panel shows the PLA holder and the positioning of the laser fiber with respect to the tissue sample, while the right panel provides a zoomed-in view of the sensing region, highlighting the locations of the selected FBGs selected for the numerical–experimental comparison. Among the full arrays, the sensors $\mathrm{FBG_{A5}}, \mathrm{FBG_{B5}}, \mathrm{FBG_{C4}}, \mathrm{FBG_{D4}}$ were identified as the most significant due to their proximity and orientation with respect to the laser applicator. In particular, $\mathrm{FBG_{A5}}$ lies on the same axial direction of the applicator at a distance of 2 mm, representing the location experiencing the strongest thermal perturbation. The bottom panel reports the color code adopted consistently throughout the chapter to identify each sensor in both the experimental temperature curves and the corresponding numerical predictions. Numerical probe points in the computational model were placed at the exact spatial coordinates of these selected FBGs, ensuring full comparability between simulations and measurements.

This agreement confirms that the computational framework correctly reproduces the main thermal phases characterizing nanoparticle-mediated laser ablation. The results in Figure 7.4 highlight that the classical Fourier formulation does not correctly reproduce the early transient behavior of the recorded temperatures. In particular, Fourier predicts an almost instantaneous and overly linear temperature rise, lacking the initial curvature and thermal inertia clearly visible in the experimental data. This discrepancy is most evident in the first seconds of laser irradiation (yellow arrows), where the FBG measurements show a gradual bending of the curve that Fourier fails to capture. In contrast, the DPL model provides a much closer match to the experimental dynamics. By incorporating finite-speed thermal propagation effects, the DPL formulation accurately reproduces both the shape and timing of the initial temperature evolution and the subsequent transition toward the plateau region. This improved agreement confirms that the DPL model is better suited to describe the fast and localized heating phenomena characteristic of nanoparticle-mediated laser ablation. This agreement demonstrates the capability of the DPL formulation to reproduce the finite-speed thermal dynamics characteristic of nanoparticle-enhanced heating, thereby justifying its selection as the reference model for the results presented throughout this section.

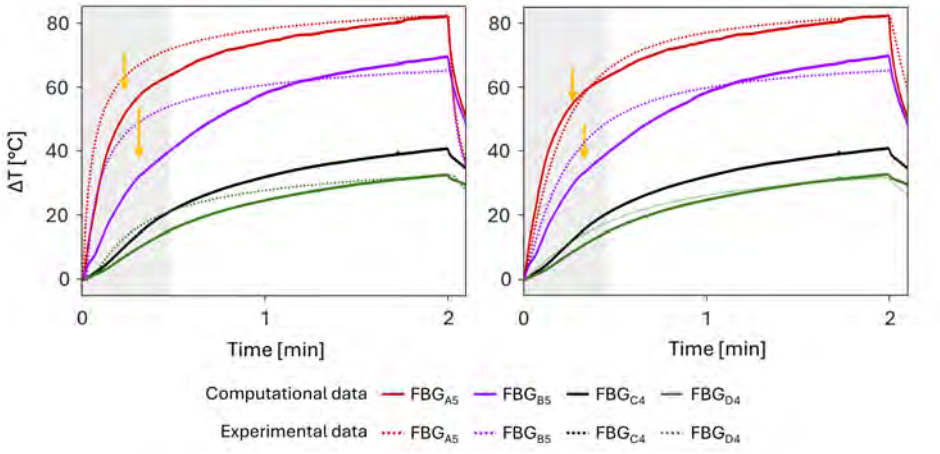

Figure 7.4: Comparison between experimental temperature profiles measured via FBG sensors $\mathrm{FBG_{A5}}, \mathrm{FBG_{B5}}, \mathrm{FBG_{C4}}, \mathrm{FBG_{D4}}$ (solid lines) and numerical predictions obtained with the Fourier and DPL heat transfer models (dashed lines) during nanoparticle-mediated laser ablation. The yellow arrows highlight the early-stage transient region, where the discrepancies between the computational models become most evident: the Fourier model exhibits an overly abrupt and linear rise, whereas the DPL formulation more accurately reproduces the gradual curvature observed experimentally.

Figure 7.5 presents the comparison between the experimental temperature measurements and the numerical predictions for the reference case without nanoparticles. The numerical model reproduces the overall thermal behavior observed experimentally, capturing the rapid temperature increase within the first seconds of irradiation, followed by a tendency toward stabilization. This agreement confirms that the computational framework captures the fundamental thermal dynamics of the system, and can therefore be confidently extended to describe more complex configurations, such as those involving nanoparticle-mediated heating.

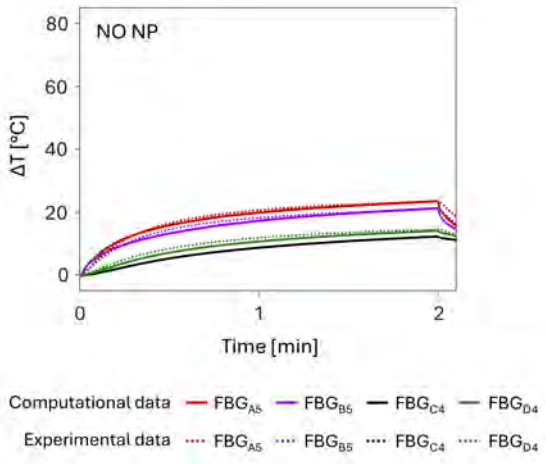

Figure 7.5: Comparison between experimental temperature profiles measured via FBG sensors (FBG_{A5}, FBG_{B5}, FBG_{C4}, FBG_{D4}) and numerical predictions for the reference phantom without nanoparticles. The computational model reproduces the main features of the thermal evolution observed experimentally, including the rapid initial temperature rise and the subsequent tendency toward stabilization during the laser-on phase.

Figure 7.6 extends this comparison to the four nanoparticle-mediated configurations: NC_1, NC_2, NC_3, and NR. In all cases, the simulated temperature curves (dashed lines) follow the same qualitative trend observed in the reference agarose phantom, with a strong initial rise that reflects the localized heat deposition induced by nanoparticle photothermal conversion.

It is important to emphasize that, due to the axial symmetry of the computational model with respect to the z-axis (the direction of laser beam propagation, see (7.8)), the numerical probe points corresponding to FBG_{C4} and FBG_{D4} produce perfectly overlapping temperature curves. This is expected, as these sensors are positioned at the same radial distance of 2 mm from the applicator along the y-direction. In the experimental data, however, FBG_{C4} and FBG_{D4} do not coincide perfectly. This discrepancy is attributable to small but unavoidable uncertainties in the manual positioning of the FBG arrays within the tissue sample, an inherent challenge when inserting fiber-optic sensors into soft media.

Regardless of the nanoparticle type, the numerical model exhibits a consistent spatial hierarchy in the predicted temperature rise: the highest temperature is always registered at the probe corresponding to FBG_{A5}, followed by FBG_{B5}, and finally by the pair FBG_{C4} and FBG_{D4}. This behavior reflects the shape of the thermal field induced by the laser source. As shown in Figure 7.7, the temperature distribution is not spherical but rather elongated along the laser propagation direction, with a pronounced axial gradient along the z-axis. Consequently, measurement points aligned with the beam (e.g., A5 and B5) experience substantially higher temperatures than those located laterally at the same radial distance. Overall, these results confirm that the computational model accurately reproduces the main features of the temperature field generated during nanoparticle-mediated laser ablation and provides a solid basis for interpreting the experimental measurements.

Figure 7.7 shows the temperature distributions obtained from the numerical simulations for the three coated nanoparticle configurations (NC_1, NC_2, and NC_3).

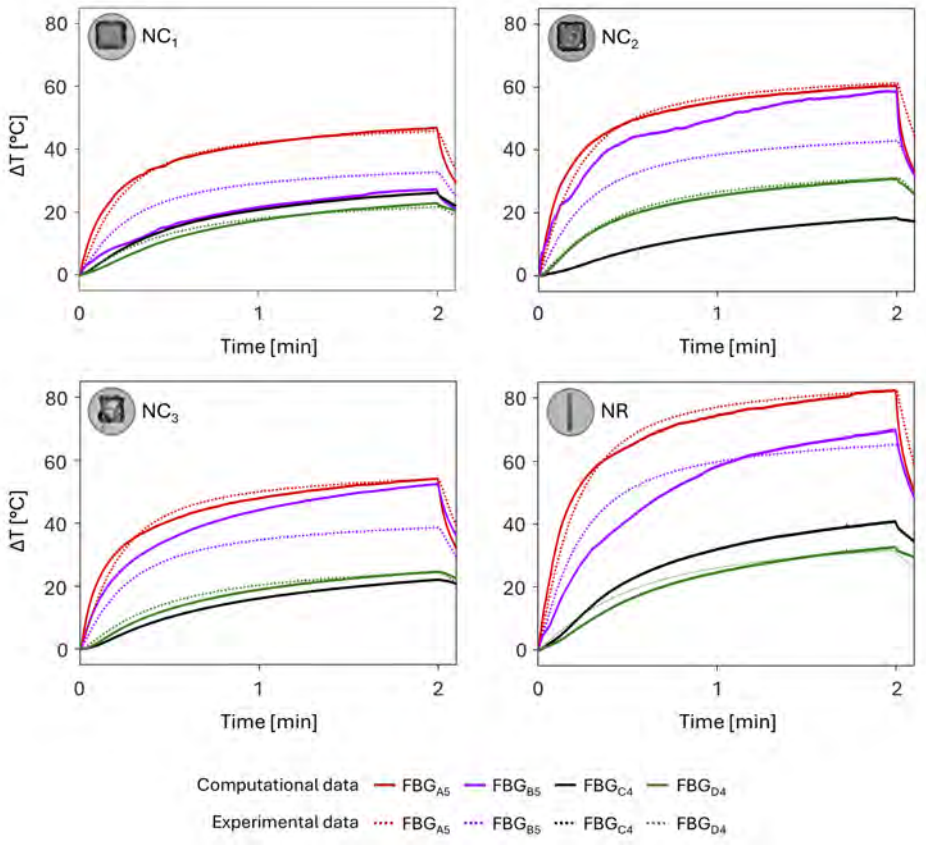

Figure 7.6: Experimental (solid lines) and numerical (dashed lines) temperature profiles for the four nanoparticle-mediated configurations (NC_1, NC_2, NC_3, and NR), recorded at the selected FBG locations (FBG_{A5}, FBG_{B5}, FBG_{C4}, FBG_{D4}).

For a consistent visual comparison, all fields were rescaled to the maximum temperature reached in the NC_2 case of 120 °C. Despite the different photothermal conversion efficiencies of the three nanoparticle types, the resulting temperature patterns exhibit a remarkably similar structure. In all cases, the thermal distribution develops as an elongated region along the z-axis, corresponding to the direction of laser propagation. This geometry reflects the dominance of axial heat transport following the localized energy deposition near the applicator tip.

Figure 7.8 reports the temperature field for the NR configuration. Although the NR configuration exhibits a slightly lower photothermal conversion efficiency compared to NC_2 (Table 4.2), the resulting temperature field reaches values up to approximately 180 °C at the applicator surface. This behavior is explained by the markedly higher absorption cross section of NR, which is one order of magnitude larger than NC_2 due to their elongated morphology (Table 7.1). As discussed in Section 7.1, the absorption cross section is a key parameter in the optical model, directly governing the amount of laser energy absorbed by the nanoparticles. Consequently, despite a slightly lower conversion efficiency, NR induce a much stronger and more localized energy deposition in the tissue, which results in the markedly

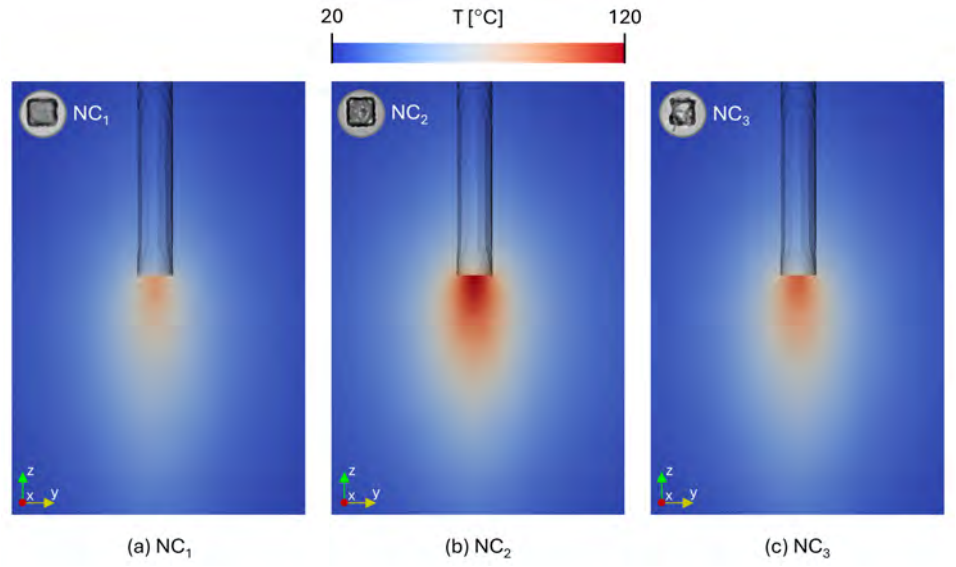

Figure 7.7: Numerical temperature distributions for the three coated nanoparticle configurations (NC_1, NC_2, and NC_3), rescaled to the maximum temperature of 120 °C obtained in the NC_2 case for visual comparison. This axial elongation reflects the dominance of directional heat transport induced by the localized near-field absorption around the fiber tip.

higher temperatures observed near the fiber tip. This enhanced local absorption also affects the shape of the thermal field. Unlike the NC cases, where the temperature remains elongated along the z-axis, the NR configuration produces a slightly more spherical distribution in the vicinity of the applicator. Here, the intense energy deposition near the fiber limits axial heat propagation and leads to a more compact and concentrated heating profile around the tip.

From the comparison in Figure 7.9, it is evident that the numerical temperature distribution obtained in the computational model (b) reproduces the same qualitative thermal shape observed experimentally in *ex vivo* liver tissue (a). In particular, the shape associated with nanoparticle-mediated heating exhibits the expected axial elongation along the laser direction, consistent with the spatial pattern measured in biological tissue. This match in the overall geometry of the thermal field supports the reliability of the computational model in describing the fundamental behavior of nanoparticle-enhanced laser heating. Nevertheless, a fully consistent validation would ultimately require a direct comparison with a computational model developed on liver-specific optical and thermal properties, enabling a more accurate reproduction of the *ex vivo* conditions.

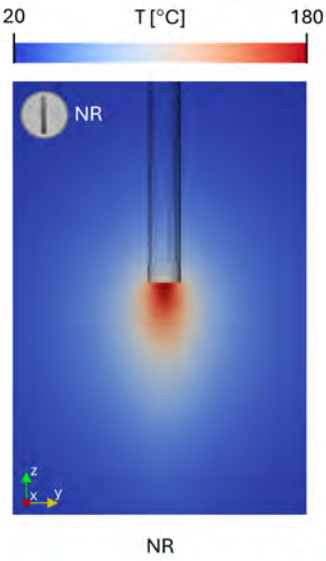

Figure 7.8: Numerical temperature distribution for the NR configuration. The visualization highlights a compact and highly localized heating region surrounding the laser applicator tip, with temperatures reaching approximately 180 °C at the fiber surface.

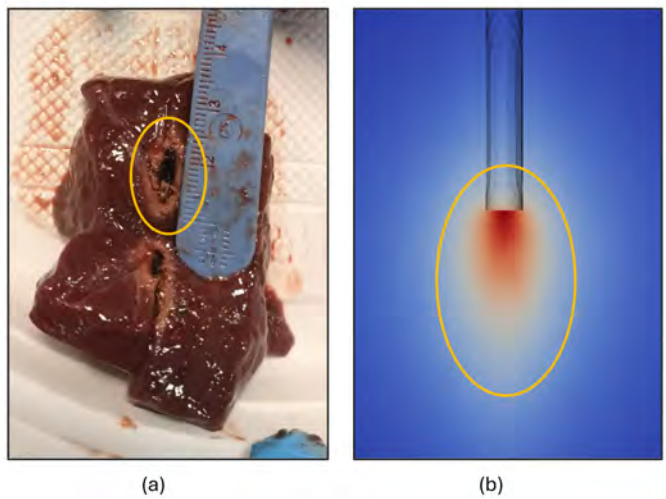

Figure 7.9: Comparison between the thermal lesion observed experimentally in *ex vivo* liver tissue (a) and the numerical temperature distribution obtained from the *in vitro* agarose model (b). In both cases, the heated region exhibits a similar elongated morphology along the direction of laser propagation, highlighted by the yellow contours

7.2 Ex-vivo LA computational modeling

To conclude this chapter, we introduce the first steps toward the development of a patient-specific computational model of the liver aimed at predicting the thermal effects of nanoparticle-mediated laser ablation. This activity represents the natural extension of the modeling framework presented in this thesis and is intended to bridge the gap between the *in vitro* simulations performed on agarose phantoms and the *ex vivo* experiments conducted on liver tissue.

The mathematical model adopted for this purpose is the same formulated in Chapter 7, and will require the integration of liver-specific optical, thermal, and structural properties, including absorption and scattering coefficients, perfusion rates, and anisotropic thermal conductivities. At the current stage, the focus has been placed on the geometric reconstruction of a real liver, representing the foundational step for future simulations.

Figure 7.10 shows the CT scans used to generate the patient-specific liver geometry. Panel displays an axial slice (a), coronal slice (b) and sagittal slice (c). These cross-sectional images constitute the anatomical basis from which the liver surface will be segmented.

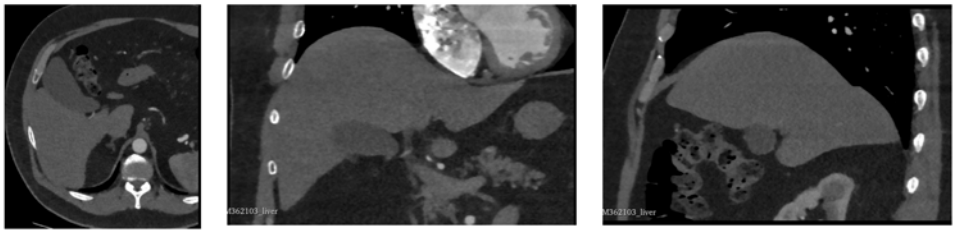

Figure 7.10: Liver CT scan: (a) axial slice, (b) coronal slice and (c) sagittal slice.

Following the complete segmentation workflow, Figure 7.11 shows the resulting three-dimensional, patient-specific reconstruction of the liver, generated within the 3D Slicer software environment.

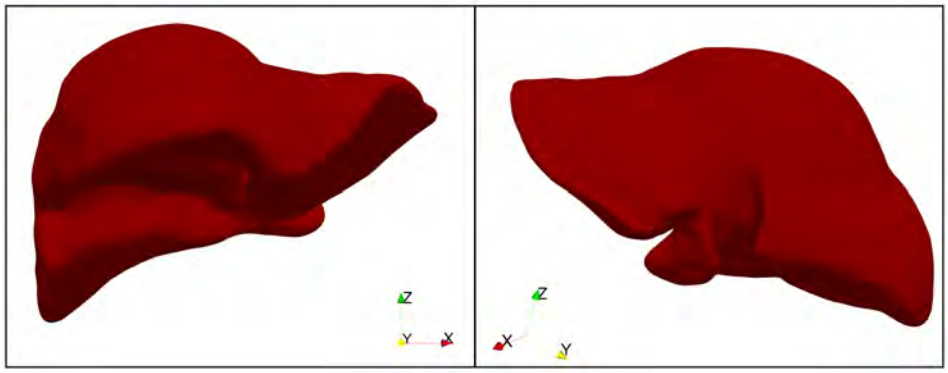

Figure 7.11: Liver geometry reconstruction.

After the patient-specific reconstruction of the liver geometry, an additional step consisted in integrating the laser applicator and a representative tumor subvolume within the anatomical model. These components were positioned in accordance with realistic clinical configurations, ensuring that the computational domain reflects the spatial relationships encountered during interstitial laser ablation procedures. Subsequently, the complete mesh was generated within the Salome software. A dedicated local refinement was applied within a rectangular subregion enclosing the tumor compartment to accurately resolve the steep thermal gradients expected during nanoparticle-mediated heating. The resulting high-resolution mesh thus provides the spatial discretization required for the numerical solution of the optical–thermal model introduced in Chapter 7. Figure 7.12 illustrates the patient-specific liver geometry, the embedded laser applicator, the tumor region, and the refined mesh block surrounding the target zone. This configuration constitutes the foundation upon which the forthcoming simulations of nanoparticle-enhanced laser ablation in real anatomical domains will be developed.

The work presented in this section represents the first foundational step toward the development of a fully patient-specific computational framework for predicting the effects of nanoparticle-mediated laser ablation in real liver anatomy. While the current stage has focused on the geometric reconstruction and preliminary setup of the computational domain, future efforts will integrate the complete optical-thermal model, incorporating liver-specific physical parameters, heterogeneous tissue properties, and realistic boundary conditions. Ongoing developments aim to couple the patient-specific geometry with a detailed representation of tumoral subregion and spatially varying nanoparticle distributions, enabling a more physiologically accurate simulation of heat deposition and thermal damage. Further advancements will include model validation against new sets of *ex vivo* measurements, as well as the exploration of computational strategies for treatment planning, sensitivity analysis, and optimization of nanoparticle-enhanced laser therapies. This research work will contribute to the establishment of a robust predictive tool capable of supporting personalized therapeutic strategies and improving the precision and safety of minimally invasive ablation procedures.

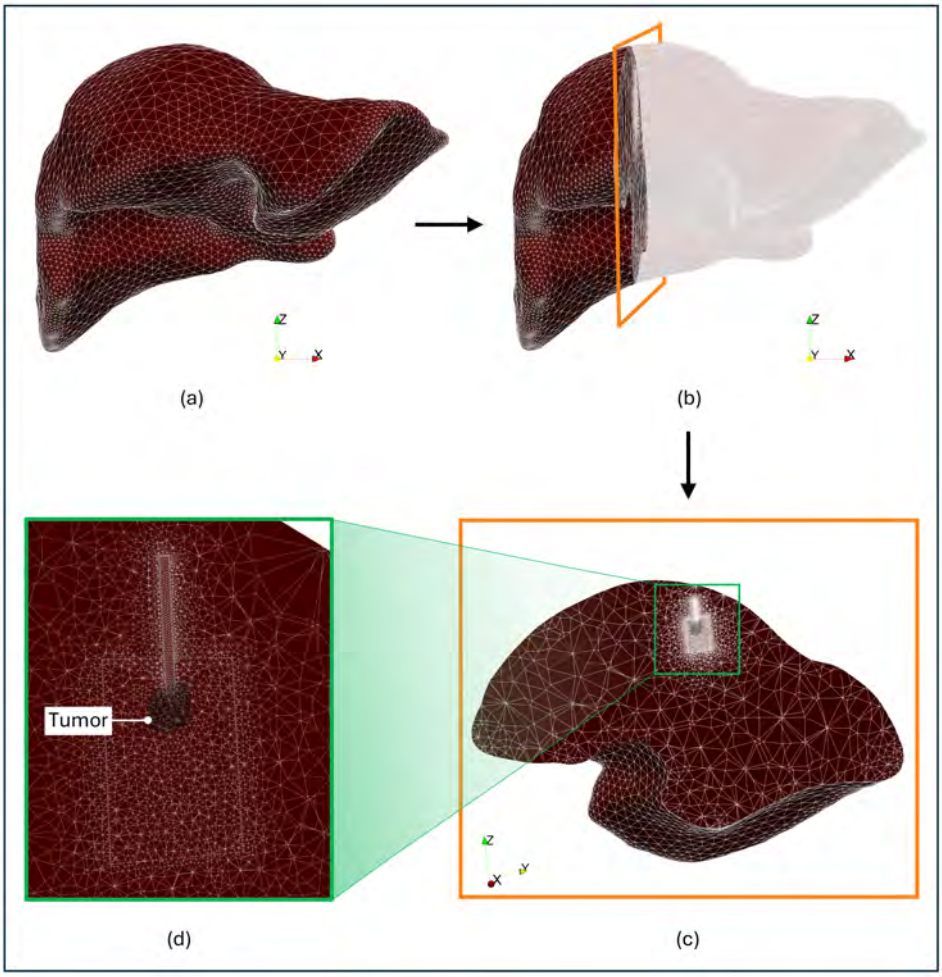

Figure 7.12: Finite element mesh generation for the patient-specific liver model. (a) Initial volumetric mesh of the reconstructed liver geometry. (b) The orange cutting plane highlights the position and orientation of the laser applicator within the liver volume. (c) View of the mesh on the zy-plane, showing the refined region around the treatment site. (d) Zoom-in of the high-resolution refined block, illustrating the embedded laser applicator, the rectangular refinement subregion, and the tumor volume.

Conclusion

8

Conclusion

This thesis investigated thermal ablation from a dual and complementary perspective: theoretical-computational modeling of laser-tissue interactions and experimental validation of laser ablation strategies *in vitro* and *ex vivo* liver tissue, including nanoparticle-mediated enhancement and high-resolution thermal monitoring. Although applied to distinct clinical scenarios, cardiac arrhythmia management through selective myocardial ablation and tumor destruction in hepatic tissue, both research directions converge toward the same overarching objective: improving the accuracy, selectivity, and predictability of minimally invasive ablation therapies across different biological and clinical contexts. By integrating computational rigor with quantitative experimental evidence, this work advances the development of thermal treatments capable of delivering controlled, localized, and patient-tailored therapeutic effects.

From the computational standpoint, the thesis extended the classical thermal models typically used in laser ablation by integrating higher-order heat transfer formulations, optical-thermal coupling, and multi-state cell damage dynamics, as highlighted in current literature on thermal therapies. These enhancements proved fundamental for capturing the fast temperature rise, the finite-speed heat propagation, and the anisotropic behavior of highly structured tissues such as myocardium. The resulting simulations demonstrated improved fidelity in predicting temperature fields and lesion morphologies, offering mechanistic insights that are crucial for the future development of patient-specific ablation planning tools.

A substantial part of this thesis involved using computational models to support, interpret, and guide the experimental activities, initially in controlled *in vitro* conditions and later in *ex vivo* liver tissue. The *in vitro* modeling, based on homogeneous phantom geometries, provided a stable reference scenario to understand the expected heat dynamics, optimize the energy delivery protocol, and anticipate the thermal regimes measured by the FBG sensors. These simulations served as a baseline for identifying deviations introduced by real tissue, such as heterogeneous water content, and optical irregularities, which became evident in the *ex vivo* measurements. In this sense, computational modeling acted as a bridge between idealized laboratory conditions and the complexity inherent to biological tissues, reducing uncertainty and strengthening the interpretation of the experimental results.

The experimental work demonstrated the feasibility and potential of

nanoparticle-mediated laser ablation for improving treatment selectivity. Gold nanorods and nanocages with tunable optical properties were tested in both synthetic phantoms and liver tissue, showing that nanoparticle-enhanced absorption can locally increase heat deposition while preserving the surrounding environment, an emerging strategy consistent with recent advances in nanomedicine [95]. The integration of Fiber Bragg Gratings, aligned with state of art sensing approaches, allowed real-time thermal monitoring with high spatial resolution. Although *ex vivo* traces exhibited the typical irregularities associated with biological heterogeneity, the sensing system proved reliable and essential for evaluating treatment dynamics, including transient signal losses during rapid temperature changes.

By combining advanced numerical models with quantitative experimental characterization, this thesis demonstrates that progress in thermal ablation requires an iterative and synergistic approach. Modeling provides explanatory power and predictive capability, while experiments expose real-world constraints and guide model refinement. This cross-disciplinary methodology enables a deeper understanding of the physical processes driving tissue damage and supports the design of more controlled and selective ablation strategies.

Looking ahead, the outcomes of this work lay a solid foundation for future developments. The integration of patient-specific geometries, vascular perfusion models, and real-time parameter identification will further improve the predictive robustness of the computational framework. Experimentally, expanding the *ex vivo* liver cohort, both in the number of samples and in their physiological variability, will be essential to strengthen the robustness and generalizability of the experimental setup. These directions are fully aligned with the objectives of the ongoing project, which is progressively advancing toward a comprehensive, clinically oriented platform for precision thermal therapies. Although significant progress has been achieved, important challenges remain, providing substantial opportunities for further research and technological innovation in this evolving field.

Appendix

9

Appendix

This appendix provides a detailed description of the synthetic protocols, physicochemical characterization, and biocompatibility assessment of the gold-based nanostructures employed for the nanoparticle-mediated laser ablation (NPs-LA) experiments presented in Chapter 4. All nanoparticles were synthesized and characterized by the NanoBioLab unit of the University of Milano-Bicocca (Italy), within the framework of "MORE CARE" PRIN 2020 project.

Four different gold-based nanostructures were developed and characterized: NC_1, NC_2, NC_3 and NR, specifically designed to exhibit tunable optical properties in the NIR region, which corresponds to the therapeutic optical window (650 – 1300 nm) commonly used for biomedical laser applications.

9.1 Materials and Synthetic Procedures

Reagents All chemical reagents were purchased from Sigma-Aldrich unless otherwise stated, and used without further purification. The following materials were employed: ethylene glycol (EG, 99.8 %), polyvinylpyrrolidone (PVP, MW 55 kDa), silver trifluoroacetate (CF_3COOAg, 98%), hydrochloric acid (HCl, 37%), sodium hydrosulfide hydrate (NaHS), gold (III) chloride trihydrate ($HAuCl_4$, 99.995 %), ammonium hydroxide (NH_4OH, 25 %), sodium borohydride ($NaBH_4$, ≥96 %), cetyltrimethylammonium bromide (CTAB, ≥ 99%), silver nitrate ($AgNO_3$, ≥99 %), and hydroquinone (HQ, ≥ 99 %).

Synthesis and Formation Silver nanocubes (AgNCs) were synthesized following the polyol reduction route described by Zhang et al. [170]. Ethylene glycol served as both solvent and reducing agent, while PVP acted as a stabilizing surfactant. The reaction was carried out at 157 °C under argon flow, and upon formation of the characteristic plasmonic peak at 440 – 442 nm (Figure 9.1(a)), the reaction was quenched in an ice bath. The obtained nanocubes had a mean edge length of 35.4 ± 5.9 nm (Figure 9.1(b)). Gold nanocages were prepared via galvanic replacement between AgNCs synthesized and $HAuCl_4$. Increasing the gold precursor concentration progressively replaced Ag with Au, forming hollow nanocages with tunable wall thickness (Figure 9.1(c)). This process induced a shift in the LSPR peak, controlled by the extent of replacement and porosity of the shell.

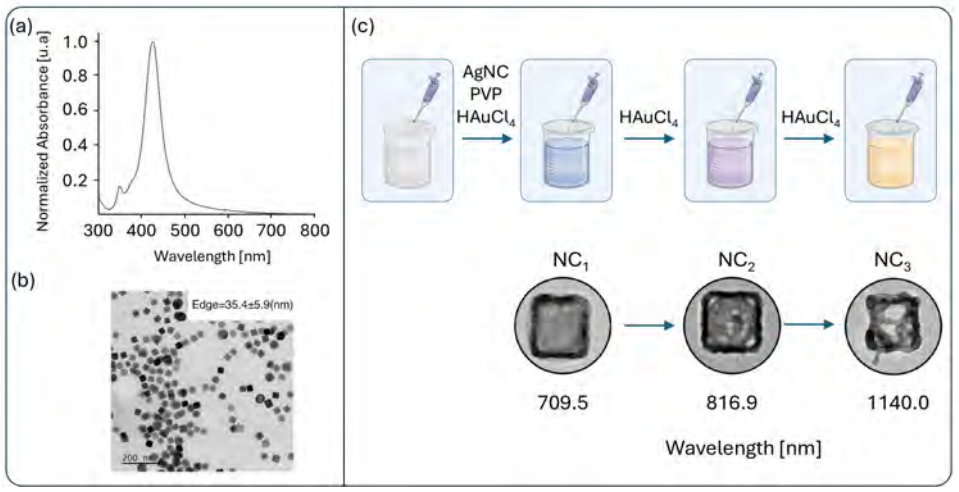

Figure 9.1: Synthesis and optical evolution of silver nanocubes and their transformation into gold nanocages NC_1, NC_2, NC_3. (a) Normalized UV–Vis absorption spectrum of AgNCs, showing the characteristic plasmonic peak in the 440 – 442 nm range. (b) AgNCs TEM picture, displaying their uniform cubic morphology and average edge length of approximately 35 nm. (c) Schematic representation of the galvanic replacement process, where increasing additions of $HAuCl_4$ progressively convert AgNCs into hollow Au-based nanocages, accompanied by a systematic red-shift of the localized surface plasmon resonance from 709.5 nm (NC_1) to 816.9 nm (NC_2) and 1140 nm (NC_3).

Three types of AuNCs were synthesized, each with a distinct LSPR:

- NC_1: $\Delta T_{max} = 709.5\,nm$
- NC_2: $\Delta T_{max} = 816.9\,nm$
- NC_3: $\Delta T_{max} = 1140\,nm$

Gold nanorods NR were obtained using a seed-mediated growth method [113]. The nanorods exhibited an average length of 63.3 ± 8.5 nm, width of 9.9 ± 0.8 nm, and an aspect ratio of 6.4 ± 0.7, resulting in a longitudinal plasmon resonance at 1105 nm.

Polymer Coating and Biocompatibility All nanoparticles were functionalized with a multidentate polymeric ligand (PCP), i.e., pyridylthiocysteamine–methoxypolyoxyethyleneamine–grafted poly (isobutylene-alt-maleic anhydride), synthesized according to Rotem et al. [171]. The PCP coating replaced traditional surfactants (PVP or CTAB), improving colloidal stability, dispersibility in aqueous media, and biocompatibility.

9.2 Physicochemical Characterization

Morphology and Size Transmission Electron Microscopy (TEM) was performed using a Jeol 2100Plus (200 kV) microscope. Representative images of all nanoparticle types are reported in Figure 4.3, showing uniform cubic and rod-like

geometries. The hydrodynamic diameters, determined via Nanoparticle Tracking Analysis (NTA, Malvern NanoSight NS300), were consistent with TEM data:

- NC_1: $85.3 \pm 1.0\,nm$
- NC_2: $77.2 \pm 0.7\,nm$
- NC_3: $72.9 \pm 2.9\,nm$
- NR: $62.2 \pm 5.5\,nm$

Optical Characterization Optical properties were analyzed by UV–Vis–NIR spectroscopy (Perkin Elmer Lambda 950 and Cary 60). The spectra in Figure 4.4 show clear plasmonic peaks corresponding to the designed LSPR positions. The measured molar extinction coefficients ε at 1064 nm were:

- NC_1: $1.9 \cdot 10^9\,mol^{-1}\,cm^{-1}$
- NC_2: $2.26 \cdot 10^9\,mol^{-1}\,cm^{-1}$
- NC_3: $3.24 \cdot 10^9\,mol^{-1}\,cm^{-1}$
- NR: $4.09 \cdot 10^9\,mol^{-1}\,cm^{-1}$

The red-shift trend confirms the effect of progressive galvanic replacement, yielding increasing absorption in the NIR region.

Elemental Composition - EDX Analysis Elemental composition was carried out via EDX (Energy-Dispersive X-ray[1]) analysis (Figure 9.2), averaged over three independent regions per sample.

These results clearly demonstrate that while silver is present in the early stages of nanocube formation (NC_1 and NC_2), its relative content significantly decreases in NC_3. This trend is consistent with the galvanic replacement mechanism: the Au:Ag ratios progressively increased with the degree of replacement (Figure 9.3). Moreover, as expected, in NR the amount of silver is negligible, since Ag mainly acts as a capping agent and remains adsorbed only in small amounts on the gold crystal surface.

9.3 Photothermal Performance

The photothermal conversion efficiency - η, was quantified under 1064 nm laser irradiation using the equation:

$$\eta = \frac{hS(\Delta T_{max,NPs} - Q_s)}{P(1 - 10^{-A_\lambda})} \tag{9.1}$$

where h is the heat transfer coefficient, S is the surface area of the sensing volume, P is the incident laser power, A_λ is the optical absorbance of the nanoparticle

[1] EDX is a technique used to determine the elemental composition of a material by bombarding it with high-energy particles (like an electron beam) and analyzing the characteristic X-rays that are emitted. The energy of the emitted X-rays is unique to each element, creating a spectrum that allows for both qualitative identification and quantitative measurement of the elements present in a sample [172].

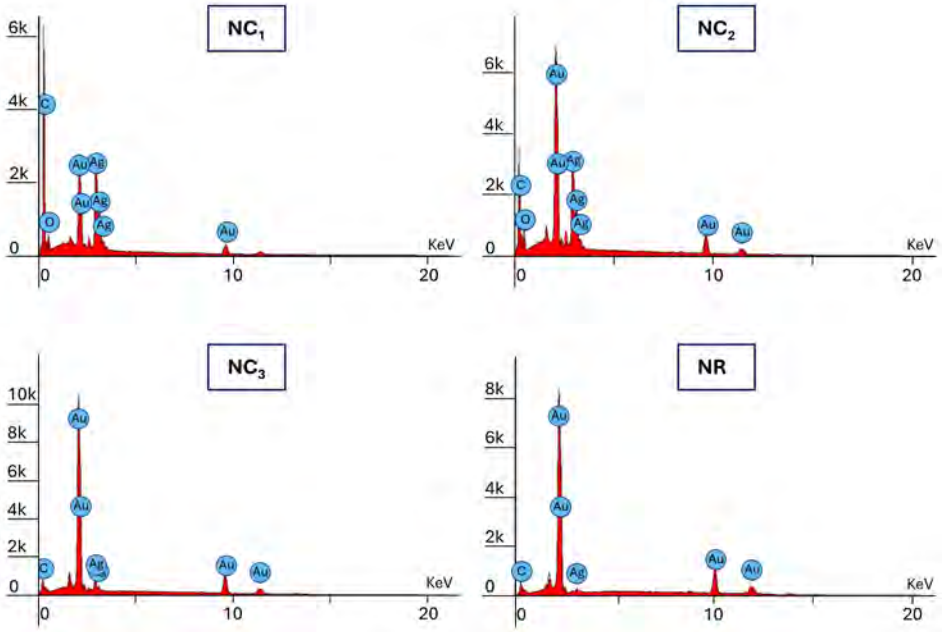

Figure 9.2: Representative EDX spectra of the synthesized nanoparticles. Each spectrum corresponds to one nanostructure type (NC_1 – NR) and shows the characteristic emission peaks of gold (Au) and silver (Ag). The progressive decrease of the Ag signal intensity and the concomitant increase of the Au peaks confirm the gradual substitution of silver by gold during the galvanic replacement process, leading to the formation of hollow nanocages with tunable composition and plasmonic properties.

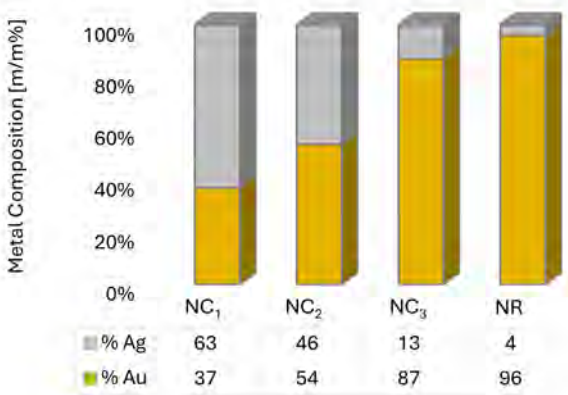

Figure 9.3: Graphical representation of the elemental composition of the synthesized nanoparticles obtained from EDX measurements. The stacked bars display the relative percentages of gold (Au) and silver (Ag) for each nanostructure type. The progressive increase in Au content from NC_1 to NC_3 confirms the gradual substitution of silver by gold during the galvanic replacement process, resulting in nanocages with tunable composition and optical response. NR exhibit an almost pure gold composition, consistent with their seed-mediated synthesis route.

colloid at the laser wavelength λ, Q_s is the heat dissipated by the agarose medium, and $\Delta T_{max,NPs}$ is the maximum temperature rise measured by the FBG sensor during irradiation.

The product hS was determined according to (9.2), where the heat transfer term was derived from the cooling dynamics of the medium:

$$hS = \frac{m_d \cdot C_d}{\tau_s} \tag{9.2}$$

Here, m_d represents the mass of the sensing volume, C_d is the specific heat capacity of the agarose gel, and τ_s is the thermal time constant extracted from the exponential decay of the cooling curve.

To evaluate these parameters, the sensing volume surrounding the FBG was approximated as a sphere with a radius of 2 mm, centered on the position of the central sensor (the one recording the maximum temperature rise). The mass of this spherical region was estimated using a gel density of $1.04\,\mathrm{g\,cm^{-3}}$, corresponding to a 4 % agarose gel, while the specific heat capacity C_d was approximated to that of water ($4.2\,\mathrm{J\,g^{-1}\,°C^{-1}}$).

The thermal time constant (τ_s) was determined from the slope of the linear relationship between $-\ln(\theta)$ and time t in the post-irradiation cooling phase:

$$\tau_s = -\frac{t}{ln(\theta)} \tag{9.3}$$

where $\theta = \frac{\Delta T}{\Delta T_{max}}$ represents the dimensionless temperature parameter.

The absorptance term $(1 - 10^{-A_\lambda})$ accounts for the fraction of laser energy absorbed by the nanoparticle suspension, where A_λ was calculated for the tested concentration of $3.0 \cdot 10^{10}$ NPs/mL. The value of Q_s, corresponding to the heat contribution of the agarose medium without nanoparticles, was independently determined as 102.2 mW. Finally, the PCE η was computed using the central FBG sensor, positioned closest to the laser applicator, as it records the highest thermal variation $\Delta T_{max,NPs}$. This approach ensures that the calculated efficiency reflects the local photothermal behavior of the nanoparticles rather than bulk thermal diffusion within the phantom. The described methodology allows the estimation of nanoparticle heating efficiency under controlled laser irradiation, providing a quantitative parameter to compare the thermal performance of the different Au-based nanostructures synthesized and tested in this work. All the quantities are summarize in Table 9.1.

9.4 Thermal Stability

Thermal stability was verified by three consecutive irradiation cycles on the same NPs-loaded phantom for NC_1, NC_2, NC_3, NR. As shown in Figure 9.4, the temperature profiles remained consistent across all repetitions, confirming the structural and optical stability of the nanoparticles during laser exposure.

9.5 Biocompatibility and Cell Viability

The nanoparticles were functionalized with the multidentate polymer PCP, whose biocompatibility was evaluated and benchmarked against common surfactants such as PMDA and PEG-SH [171].

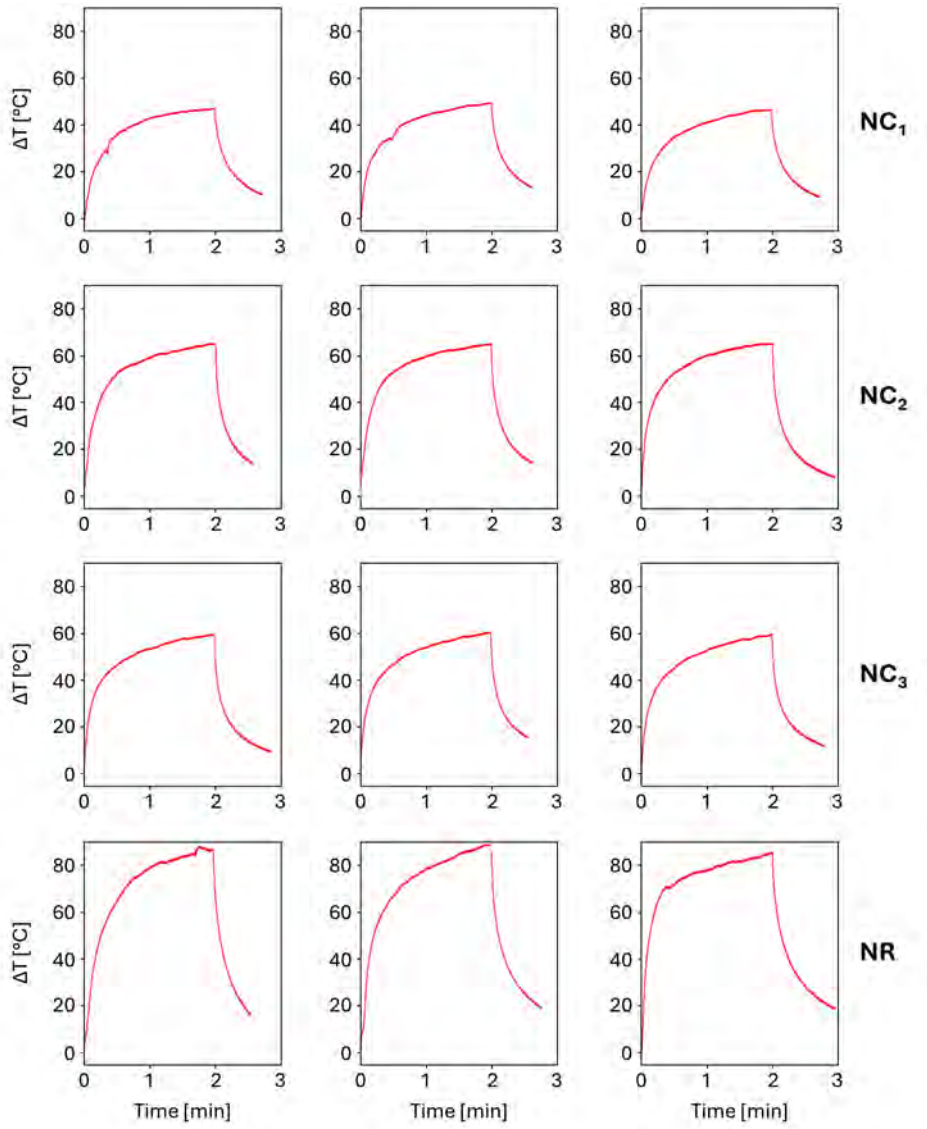

Figure 9.4: Results of thermal stability for NC_1, NC_2, NC_3, NR.

NPs	λ_{max}[nm]	ΔT_{max} [°C]	τ_s [s]	A_λ	hS [W °C^{-1}]	η [%]
NC_1	709.5	46.8	29.1	0.0960	$5.02 \cdot 10^{-3}$	22.4
NC_2	816.9	60.4	26.7	0.107	$5.48 \cdot 10^{-3}$	35.0
NC_3	1140	54.4	29.2	0.157	$5.00 \cdot 10^{-3}$	18.7
NR	1105	82.6	30.0	0.166	$4.88 \cdot 10^{-3}$	31.5

Table 9.1: Comprehensive summary of the parameters involved in the photothermal conversion efficiency PCE η analysis for the four NPs. For each sample, the table reports: the wavelength of maximum optical absorption λ_{max}, the maximum temperature increase observed during irradiation ΔT_{max}, the thermal time constant obtained from the cooling curve τ_s, the absorbance at the laser wavelength A_λ, with $\lambda = 1064$ nm, the product of the heat transfer coefficient and the sensing surface hS, and the resulting η. Together, these quantities describe the optical absorption characteristics, heat-transfer behavior, and overall photothermal performance of each nanoparticle type under 1064 nm excitation, enabling direct comparison of their heating efficiency.

In addition, cytotoxicity tests were performed using the MTT viability assay on HeLa cells exposed to increasing NP concentrations. By way of example, as illustrated in Figure 9.5, both NC_2 and NR exhibited cell viability above 90 % after 24, 48, and 72 hours, demonstrating excellent biocompatibility of the PCP-coated nanostructures.

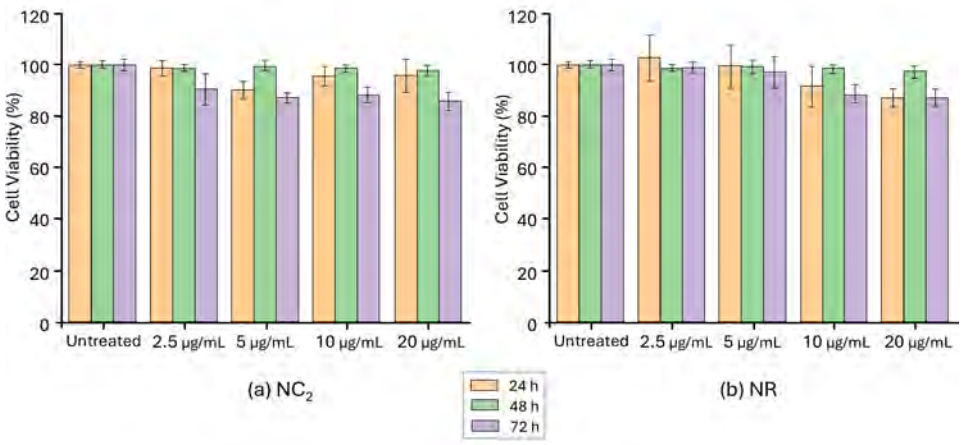

Figure 9.5: MTT cell viability assay for PCP-coated nanoparticles. Panels (a) and (b) show the viability of HeLa cells after exposure to increasing concentrations (2.5 – $20\,\mu g\,mL^{-1}$) of NC_2 and NR nanoparticles, respectively, measured after 24, 48, and 72 hours of incubation. In all conditions, cell viability remained above 90 %, confirming the excellent biocompatibility and non-cytotoxic behavior of the polymer-coated nanostructures.

Bibliography

[1] Katrina F Chu and Damian E Dupuy. Thermal ablation of tumours: biological mechanisms and advances in therapy. *Nature Reviews Cancer* (2014).

[2] Elena De Vita et al. A review on radiofrequency, laser, and microwave ablations and their thermal monitoring through fiber Bragg gratings. *IScience* (2023).

[3] Shaojie Chen. Pulsed field ablation versus thermal energy ablation for atrial fibrillation: the pulse era is arriving. *Journal of Interventional Cardiac Electrophysiology* (2024).

[4] Sundeep Singh and Roderick Melnik. Thermal ablation of biological tissues in disease treatment: A review of computational models and future directions. *Electromagnetic biology and medicine* (2020).

[5] Chris Brace. Thermal tumor ablation in clinical use. *IEEE pulse* (2011).

[6] Mehrdad Nikfarjam, Caterina Malcontenti-Wilson, and Christopher Christophi. Focal hyperthermia produces progressive tumor necrosis independent of the initial thermal effects. *Journal of Gastrointestinal Surgery* (2005).

[7] Sylvain Bodard et al. Percutaneous cryoablation in soft tissue tumor management: an educational review. *Insights into Imaging* (2024).

[8] Mehrdad Nikfarjam, Vijayaragavan Muralidharan, and Christopher Christophi. Mechanisms of focal heat destruction of liver tumors. *Journal of Surgical Research* (2005).

[9] Matthias Andres. Improving thermal ablation of liver tumors: Modeling and parameter identification of laser-induced interstitial thermotherapy. Technische Universität Kaiserslautern, 2021.

[10] John P McGahan et al. Hepatic ablation using radiofrequency electrocautery. *Investigative radiology* (1990).

[11] Yicheng Ni et al. A review of the general aspects of radiofrequency ablation. *Abdominal Imaging* (2005).

[12] Kelvin Hong and Christos Georgiades. Radiofrequency ablation: mechanism of action and devices. *Journal of Vascular and Interventional Radiology* (2010).

[13] Sundeep Singh, Ramjee Repaka, and Ahmed Al-Jumaily. Sensitivity analysis of critical parameters affecting the efficacy of microwave ablation using Taguchi method. *International Journal of RF and Microwave Computer-Aided Engineering* (2019).

[14] Neil Bhardwaj et al. Liver ablation techniques: a review. *Surgical endoscopy* (2010).

[15] Bing Zhang et al. A review of radiofrequency ablation: Large target tissue necrosis and mathematical modelling. *Physica Medica* (2016).

[16] John P McGahan and Gerald D Dodd III. Radiofrequency ablation of the liver: current status. *American Journal of Roentgenology* (2001).

[17] Thomas F Wood et al. Radiofrequency ablation of 231 unresectable hepatic tumors: indications, limitations, and complications. *Annals of Surgical Oncology* (2000).

[18] Tze M Wah et al. Radiofrequency ablation (RFA) of renal cell carcinoma (RCC): experience in 200 tumours. *BJU International* (2014).

[19] Andreas H Mahnken, Rolf W Günther, and Josef Tacke. Radiofrequency ablation of renal tumors. *European Radiology* (2004).

[20] Caroline J Simon et al. Pulmonary radiofrequency ablation: long-term safety and efficacy in 153 patients. *Radiology* (2007).

[21] Fernando Ruiz Santiago et al. Percutaneous treatment of bone tumors by radiofrequency thermal ablation. *European Journal of Radiology* (2011).

[22] Christopher L Brace. Microwave tissue ablation: biophysics, technology, and applications. *Critical Reviews™ in Biomedical Engineering* (2010).

[23] Caroline J Simon, Damian E Dupuy, and William W Mayo-Smith. Microwave ablation: principles and applications. *Radiographics* (2005).

[24] Paola Tombesi, Francesca Di Vece, and Sergio Sartori. Radiofrequency, microwave, and laser ablation of liver tumors: time to move toward a tailored ablation technique? *Hepatoma Research* (2015).

[25] Thomas J Vogl et al. Thermal ablation of lung tumors: focus on microwave ablation. *RöFo-Fortschritte auf dem Gebiet der Röntgenstrahlen und der bildgebenden Verfahren*. Georg Thieme Verlag KG. (2017).

[26] FH Cornelis, C Marcelin, and J-C Bernhard. Microwave ablation of renal tumors: a narrative review of technical considerations and clinical results. *Diagnostic and Interventional Imaging* (2017).

[27] Adrian Kastler et al. Microwave thermal ablation of spinal metastatic bone tumors. *Journal of Vascular and Interventional Radiology* (2014).

[28] Yu-Jiang Liu et al. Ultrasound-guided microwave ablation in the treatment of benign thyroid nodules in 435 patients. *Experimental Biology and Medicine* (2017).

[29] Wenjun Wu et al. US-guided percutaneous microwave ablation for the treatment of benign thyroid nodules. *Endocrine Journal* (2017).

[30] Tingting Cui et al. Safety and efficacy of microwave ablation for benign thyroid nodules and papillary thyroid microcarcinomas: A systematic review and meta-analysis. *European Journal of Radiology* (2019).

[31] James C Lin. Catheter microwave ablation therapy for cardiac arrhythmias. *Bioelectromagnetics* (1999).

[32] Jos G Maessen et al. Beating-heart surgical treatment of atrial fibrillation with microwave ablation. *The Annals of Thoracic Surgery* (2002).

[33] Carey Rappaport. Cardiac tissue ablation with catheter-based microwave heating. *International Journal of Hyperthermia* (2004).

[34] Mathew R Williams et al. Application of microwave energy in cardiac tissue ablation: from in vitro analyses to clinical use. *The Annals of Thoracic Surgery* (2002).

[35] James E Kennedy. High-intensity focused ultrasound in the treatment of solid tumours. *Nature Reviews Cancer* (2005).

[36] Arjan S Sehmbi et al. Systematic review of the role of high intensity focused ultrasound (HIFU) in treating malignant lesions of the hepatobiliary system. *HPB* (2021).

[37] Gail Ter Haar. HIFU tissue ablation: concept and devices. *Therapeutic Ultrasound* (2016).

[38] Yu-Feng Zhou. High intensity focused ultrasound in clinical tumor ablation. *World Journal of Clinical Oncology* (2011).

[39] Hyun Joo Jang et al. Current and future clinical applications of high-intensity focused ultrasound (HIFU) for pancreatic cancer. *Gut and Liver* (2010).

[40] Pavel B Rosnitskiy et al. Design of HIFU transducers for generating specified nonlinear ultrasound fields. *IEEE Transactions on Ultrasonics, Ferroelectrics, and Frequency Control* (2016).

[41] Ray H Hashemi, William G Bradley, and Christopher J Lisanti. MRI: the basics. Lippincott Williams & Wilkins, (2010).

[42] Charles Mougenot et al. Three-dimensional spatial and temporal temperature control with MR thermometry-guided focused ultrasound (MRgHIFU). *Magnetic Resonance in Medicine* (2009).

[43] Yu Xiong et al. Ultrasound-guided high-intensity focused ultrasound (USgHIFU) ablation for the treatment of patients with adenomyosis and prior abdominal surgical scars: a retrospective study. *International Journal of Hyperthermia* (2015).

[44] Zahra Izadifar et al. An introduction to high intensity focused ultrasound: systematic review on principles, devices, and clinical applications. *Journal of Clinical Medicine* (2020).

[45] Yongshuo Ji et al. High-intensity focused ultrasound (HIFU) treatment for uterine fibroids: a meta-analysis. *Archives of Gynecology and Obstetrics* (2017).

[46] Anne-Sophie Bertrand et al. Focused ultrasound for the treatment of bone metastases: effectiveness and feasibility. *Journal of Therapeutic Ultrasound* (2018).

[47] Gunnar Aus. Current status of HIFU and cryotherapy in prostate cancer–a review. *European Urology* (2006).

[48] Kevin D Evans, Brandon Weiss, and Michael Knopp. High-intensity focused ultrasound (HIFU) for specific therapeutic treatments: a literature review. *Journal of Diagnostic Medical Sonography* (2007).

[49] Joseph P Erinjeri and Timothy WI Clark. Cryoablation: mechanism of action and devices. *Journal of Vascular and Interventional Radiology* (2010).

[50] Servet Tatli et al. Percutaneous cryoablation techniques and clinical applications. *Diagnostic and Interventional Radiology* (2010).

[51] Leila Seidabadi et al. Role of Computational Modelling in Enhancing Thermal Safety During Cardiac Ablation. *Interdisciplinary CardioVascular and Thoracic Surgery* (2025).

[52] Bailey Surtees et al. Validation of a low-cost, carbon dioxide-based cryoablation system for percutaneous tumor ablation. *PLoS One* (2019).

[53] Christos S Georgiades and Jonathan K Marx. Cryoablation: Mechanism of action and devices. *Percutaneous Tumor Ablation Strategies and Techniques* (2011).

[54] Thorsten M Buzug. Computed tomography. *Springer Handbook of Medical Technology*. Springer, 2011.

[55] Shali Jiang et al. Pulsed field ablation for atrial fibrillation: mechanisms, advantages, and limitations. *Reviews in Cardiovascular Medicine* (2024).

[56] Vivek Y Reddy et al. Pulsed field ablation in patients with persistent atrial fibrillation. *Journal of the American College of Cardiology* (2020).

[57] Vivek Y Reddy et al. Pulsed field ablation of paroxysmal atrial fibrillation: 1-year outcomes of IMPULSE, PEFCAT, and PEFCAT II. *Clinical Electrophysiology* (2021).

[58] Zixi Zhang et al. Pulsed field ablation: a promising approach for ventricular tachycardia ablation. *International Journal of Cardiology* (2024).

[59] Gust H Bardy et al. Catheter-mediated electrical ablation: the relation between current and pulse width on voltage breakdown and shock-wave generation. *Circulation Research* (1988).

[60] René van Es et al. In vitro analysis of the origin and characteristics of gaseous microemboli during catheter electroporation ablation. *Journal of Cardiovascular Electrophysiology* (2019).

[61] R Jason Stafford et al. Laser-induced thermal therapy for tumor ablation. *Critical Reviews™ in Biomedical Engineering* (2010).

[62] Antony Lawrence Gough-Palmer and Wladyslaw Michal Witold Gedroyc. Laser ablation of hepatocellular carcinoma-A review. *World Journal of Gastroenterology* (2008).

[63] Carsten M Philipp and H-Peter Berlien. Laser-induced thermotherapy (LITT), Basics. *Applied Laser Medicine*. Springer, 2003.

[64] Omar Ashraf et al. Laser-induced thermal therapy in neuro-oncology: a review. *World Neurosurgery* (2018).

[65] Emiliano Schena, Paola Saccomandi, and Yuman Fong. Laser ablation for cancer: past, present and future. *Journal of Functional Biomaterials* (2017).

[66] V Muralidharan, C Malcontenti-Wilson, and Chris Christophi. Interstitial laser hyperthermia for colorectal liver metastases: the effect of thermal sensitization and the use of a cylindrical diffuser tip on tumor necrosis. *Journal of Clinical Laser Medicine & Surgery* (2002).

[67] Hoon Chung et al. The nuts and bolts of low-level laser (light) therapy. *Annals of Biomedical Engineering* (2012).

[68] Viravuth Prapavat et al. In vitro studies and computer simulations to assess the use of a diode laser (850 nm) for laser-induced thermotherapy (LITT). *Lasers in Surgery and Medicine* (1996).

[69] DR Wyman, WM Whelan, and BC Wilson. Interstitial laser photocoagulation: Nd: YAG 1064 nm optical fiber source compared to point heat source. *Lasers in Surgery and Medicine* (1992).

[70] Giovanni Mauri et al. Laser and radiofrequency ablations for benign and malignant thyroid tumors. *International Journal of Hyperthermia* (2019).

[71] Katrin Hegenscheid et al. Assessing early vascular changes and treatment response after laser-induced thermotherapy of pulmonary metastases with perfusion CT: initial experience. *American Journal of Roentgenology* (2010).

[72] Dennis Krist. Novel laser energy applications for the treatment of cardiac arrhythmias. PhD thesis. Maastricht University, 2022.

[73] Li Poa et al. Laser ablation of atrial fibrillation: mid-term clinical experience. *Journal of Atrial Fibrillation* (2009).

[74] Ramanathan Parameswaran, Ahmed M Al-Kaisey, and Jonathan M Kalman. Catheter ablation for atrial fibrillation: current indications and evolving technologies. *Nature Reviews Cardiology* (2021).

[75] Rohan S Wijesurendra and Barbara Casadei. Mechanisms of atrial fibrillation. *Heart* (2019).

[76] Mark E Josephson et al. Recurrent sustained ventricular tachycardia. 1. Mechanisms. *Circulation* (1978).

[77] Karl-Heinz Kuck et al. Cryoballoon or radiofrequency ablation for paroxysmal atrial fibrillation. *New England Journal of Medicine* (2016).

[78] Jason G Andrade et al. Cryoablation or drug therapy for initial treatment of atrial fibrillation. *New England Journal of Medicine* (2021).

[79] Boaz Avitall et al. Physics and engineering of transcatheter cardiac tissue ablation. *Journal of the American College of Cardiology* (1993).

[80] Massimiliano Leoni et al. Impact of Catheter Orientation on Cardiac Radiofrequency Ablation. *International Workshop on Statistical Atlases and Computational Models of the Heart*. Springer. 2023.

[81] Robert Splinter. Laser Catheter Ablation of Cardiac Arrhythmias: Experimental and Basic Research and Clinical Results. *Lasers in Cardiovascular Interventions*. Springer, 2015.

[82] Dennis Krist. Novel laser energy applications for the treatment of cardiac arrhythmias. PhD thesis. Maastricht University, 2022.

[83] Rachel S Riley and Emily S Day. Gold nanoparticle-mediated photothermal therapy: applications and opportunities for multimodal cancer treatment. *Wiley Interdisciplinary Reviews: Nanomedicine and Nanobiotechnology* (2017).

[84] Wenjie Yang et al. Gold nanoparticle based photothermal therapy: Development and application for effective cancer treatment. *Sustainable Materials and Technologies* (2019).

[85] Hyung Shik Kim and Dong Yun Lee. Near-infrared-responsive cancer photothermal and photodynamic therapy using gold nanoparticles. *Polymers* (2018).

[86] Seongman Lee et al. Recent advances in the design of organic photothermal agents for cancer treatment: A review. *Coordination Chemistry Reviews* (2024).

[87] Seyma Nur Turkmen Koc et al. Gold nanoparticles-mediated photothermal and photodynamic therapies for cancer. *International Journal of Pharmaceutics* (2024).

[88] Hwa Seung Han and Ki Young Choi. Advances in nanomaterial-mediated photothermal cancer therapies: toward clinical applications. *Biomedicines* (2021).

[89] Tomy Muringayil Joseph et al. Nanoparticles: taking a unique position in medicine. *Nanomaterials* (2023).

[90] Cumali Keskin et al. Green synthesis and characterization of silver nanoparticles using anchusa officinalis: antimicrobial and cytotoxic potential. *International Journal of Nanomedicine* (2025).

[91] Mariana Amaral et al. How can biomolecules improve mucoadhesion of oral insulin? A comprehensive insight using ex-vivo, in silico, and in vivo models. *Biomolecules* (2020).

[92] Kıvılcım Öztürk, Meryem Kaplan, and Sema Çalış. Effects of nanoparticle size, shape, and zeta potential on drug delivery. *International Journal of Pharmaceutics* (2024).

[93] Lucian Mocan et al. Advances in cancer research using gold nanoparticles mediated photothermal ablation. *Clujul Medical* (2016).

[94] Somayeh Asadi et al. Laser-induced optothermal response of gold nanoparticles: From a physical viewpoint to cancer treatment application. *Journal of Biophotonics* (2021).

[95] Mariana Neves Amaral et al. Gold nanoparticle-mediated photothermal therapy: Expanding the frontiers of cancer treatment and theragnostics. *Biomedicine & Pharmacotherapy* (2025).

[96] H Yockell-Lelièvre, F Lussier, and J-F Masson. Influence of the particle shape and density of self-assembled gold nanoparticle sensors on LSPR and SERS. *The Journal of Physical Chemistry C* (2015).

[97] Julien Gardan. Additive manufacturing technologies: state of the art and trends. *Additive Manufacturing Handbook* (2017).

[98] Ferry PW Melchels, Jan Feijen, and Dirk W Grijpma. A review on stereolithography and its applications in biomedical engineering. *Biomaterials* (2010).

[99] Fabrizio Fina et al. Selective laser sintering (SLS) 3D printing of medicines. *International Journal of Pharmaceutics* (2017).

[100] Omar A Mohamed, Syed H Masood, and Jahar L Bhowmik. Optimization of fused deposition modeling process parameters: a review of current research and future prospects. *Advances in Manufacturing* (2015).

[101] Vincent DeStefano, Salaar Khan, and Alonzo Tabada. Applications of PLA in modern medicine. *Engineered Regeneration* (2020).

[102] *Ender 3 V2 3D Printer Meanwell Power User Manual*.

[103] Paola Saccomandi, Emiliano Schena, and Sergio Silvestri. Techniques for temperature monitoring during laser-induced thermotherapy: An overview. *International Journal of Hyperthermia* (2013).

[104] Sanzhar Korganbayev et al. Closed-loop temperature control based on fiber bragg grating sensors for laser ablation of hepatic tissue. *Sensors* (2020).

[105] Bashir Ahmed Tahir, Jalil Ali, and Rosly Abdul Rahman. Fabrication of fiber grating by phase mask and its sensing application. *Journal of Optoelectronics and Advanced Materials* (2006).

[106] Wei He et al. Point-by-point femtosecond-laser inscription of 2-μm-wavelength-band FBG through fiber coating. *IEEE Photonics Journal* (2018).

[107] Francesca De Tommasi et al. Fiber Bragg grating sensors for temperature monitoring during thermal ablation procedure: Experimental assessment of artefact caused by respiratory movements. *IEEE Sensors Journal* (2021).

[108] Anees Mohammed and Siniša Djurović. A study of distributed embedded thermal monitoring in electric coils based on FBG sensor multiplexing. *Microprocessors and Microsystems* (2018).

[109] Gautam Hegde, S Asokan, and Gopalkrishna Hegde. Fiber Bragg grating sensors for aerospace applications: A review. *ISSS Journal of Micro and Smart Systems* (2022).

[110] Federica Bianconi et al. Investigating fbg sensor arrangements and computational modeling in photothermal laser treatment. *2023 International Workshop on Biomedical Applications, Technologies and Sensors (BATS)*. IEEE. 2023.

[111] Jichuan Qiu et al. Gold nanocages for effective photothermal conversion and related applications. *Chemical Science* (2020).

[112] Haoyan Cheng et al. Galvanic replacement synthesis of metal nanostructures: bridging the gap between chemical and electrochemical approaches. *Accounts of Chemical Research* (2023).

[113] Huei-Huei Chang and Catherine J Murphy. Mini gold nanorods with tunable plasmonic peaks beyond 1000 nm. *Chemistry of Materials* (2018).

[114] CY Tang and Z Yang. Transmission electron microscopy (TEM). *Membrane Characterization*. Elsevier, 2017.

[115] Vasco Filipe, Andrea Hawe, and Wim Jiskoot. Critical evaluation of Nanoparticle Tracking Analysis (NTA) by NanoSight for the measurement of nanoparticles and protein aggregates. *Pharmaceutical Research* (2010).

[116] Marcello Picollo, Maurizio Aceto, and Tatiana Vitorino. UV-Vis spectroscopy. *Physical Sciences Reviews* (2019).

[117] Xijian Liu et al. Facile synthesis of biocompatible cysteine-coated CuS nanoparticles with high photothermal conversion efficiency for cancer therapy. *Dalton Transactions* (2014).

[118] Federica Bianconi et al. Nanoparticle-mediated laser ablation: an integrated phantom experimental-computational framework for selective cancer therapy. *IEEE Journal of Selected Topics in Quantum Electronics* (2025).

[119] Assunta Andreozzi et al. Modeling heat transfer in tumors: a review of thermal therapies. *Annals of biomedical engineering* (2019).

[120] Enrique J Berjano. Theoretical modeling for radiofrequency ablation: state-of-the-art and challenges for the future. *Biomedical engineering online* (2006).

[121] Jason Chiang, Peng Wang, and Christopher L Brace. Computational modelling of microwave tumour ablations. *International Journal of Hyperthermia* (2013).

[122] Punit Prakash. Theoretical modeling for hepatic microwave ablation. *The open biomedical engineering journal* (2010).

[123] Ugo Tricoli et al. Optimized diffusion approximation. *JOSA A* (2018).

[124] Francisco J Reynoso et al. Implementation of a multisource model for gold nanoparticle-mediated plasmonic heating with near-infrared laser by the finite element method. *Medical Physics* (2013).

[125] Lihong V Wang and Hsin-i Wu. Biomedical Optics: Principles and Imaging. John Wiley & Sons, 2007.

[126] Mengyu Jia et al. Coupling between radiative transport and diffusion approximation for enhanced near-field photon-migration modeling based on transient photon kinetics. *Journal of Biomedical Optics* (2016).

[127] David A Boas, Constantinos Pitris, and Nimmi Ramanujam. Handbook of biomedical optics. CRC Press, 2016.

[128] Juan A Lopez Molina, Maria J Rivera, and Enrique Berjano. Fourier, hyperbolic and relativistic heat transfer equations: a comparative analytical study. *Proceedings of the Royal Society A: Mathematical, Physical and Engineering Sciences* (2014).

[129] Harry H Pennes. Analysis of tissue and arterial blood temperatures in the resting human forearm. *Journal of Applied Physiology* (1948).

[130] JC Chato. Heat transfer to blood vessels. *Journal of Biomechanical Engineering* (1980).

[131] Kuo-Chi Liu and Yuen-Shin Chen. Analysis of heat transfer and burn damage in a laser irradiated living tissue with the generalized dual-phase-lag model. *International Journal of Thermal Sciences* (2016).

[132] Argyrios Petras et al. Calibration of a three-state cell death model for cardiomyocytes and its application in radiofrequency ablation. *Physiological Measurement* (2023).

[133] Leonardo Molinari et al. Multiscale and multiphysics modeling of anisotropic cardiac RFCA: experimental-based model calibration via multi-point temperature measurements. *Frontiers in Physiology* (2022).

[134] Da Yu Tzou. The generalized lagging response in small-scale and high-rate heating. *International Journal of Heat and Mass Transfer* (1995).

[135] Nazia Afrin et al. Numerical simulation of thermal damage to living biological tissues induced by laser irradiation based on a generalized dual phase lag model. *Numerical Heat Transfer, Part A: Applications* (2012).

[136] Sundeep Singh and Roderick Melnik. Coupled thermo-electro-mechanical models for thermal ablation of biological tissues and heat relaxation time effects. *Physics in Medicine & Biology* (2019).

[137] Ying Hu, Xue-Yang Zhang, and Xian-Fang Li. Thermoelastic response of skin using time-fractional dual-phase-lag bioheat heat transfer equation. *Journal of Thermal Stresses* (2022).

[138] John A Pearce. Comparative analysis of mathematical models of cell death and thermal damage processes. *International Journal of Hyperthermia* (2013).

[139] Abdul M Qadri, Nicholas JY Chia, and Ean H Ooi. Effects of saline volume on lesion formation during saline-infused radiofrequency ablation. *Applied Mathematical Modelling* (2017).

[140] S Singh. Thermal analysis of temperature-controlled radiofrequency ablation of cancerous tissue. PhD thesis. 2018.

[141] Sundeep Singh, Arka Bhowmik, and Ramjee Repaka. Thermal analysis of induced damage to the healthy cell during RFA of breast tumor. *Journal of thermal biology* (2016).

[142] Stephen A Sapareto and William C Dewey. Thermal dose determination in cancer therapy. *International Journal of Radiation Oncology* Biology* Physics* (1984).

[143] Gerard C Van Rhoon et al. CEM43° C thermal dose thresholds: a potential guide for magnetic resonance radiofrequency exposure levels? *European Radiology* (2013).

[144] Gerard C van Rhoon. Is CEM43 still a relevant thermal dose parameter for hyperthermia treatment monitoring? *International Journal of Hyperthermia* (2016).

[145] Macarena Trujillo and Enrique Berjano. Review of the mathematical functions used to model the temperature dependence of electrical and thermal conductivities of biological tissue in radiofrequency ablation. *International Journal of Hyperthermia* (2013).

[146] David P O'Neill et al. A three-state mathematical model of hyperthermic cell death. *Annals of biomedical engineering* (2011).

[147] Neil T Wright. Mathematical Models of Cell Response Following Heating. *Molecular, Cellular, and Tissue Engineering of the Vascular System* (2018).

[148] Lingjuan He and Bin Zhou. Cardiomyocyte proliferation: remove brakes and push accelerators. *Cell Research* (2017).

[149] Chang Sub Park et al. A model of tissue contraction during thermal ablation. *Physiological measurement* (2016).

[150] Chang Sub Park et al. A thermoelastic deformation model of tissue contraction during thermal ablation. *International Journal of Hyperthermia* (2018).

[151] Igor A. Baratta et al. *DOLFINx: The next generation FEniCS problem solving environment*. en. 2023.

[152] Matthew W. Scroggs et al. Construction of arbitrary order finite element degree-of-freedom maps on polygonal and polyhedral cell meshes. *ACM Transactions on Mathematical Software* (2022).

[153] Martin S Alnæs et al. Unified form language: A domain-specific language for weak formulations of partial differential equations. *ACM Transactions on Mathematical Software (TOMS)* (2014).

[154] Robert Splinter et al. Optical properties of normal, diseased, and laser photocoagulated myocardium at the Nd: YAG wavelength. *Lasers in Surgery and Medicine* (1991).

[155] Herve Lombaert et al. Human atlas of the cardiac fiber architecture: study on a healthy population. *IEEE Transactions on Medical Imaging* (2012).

[156] Martina Zaltieri et al. Techniques for temperature monitoring of myocardial tissue undergoing radiofrequency ablation treatments: an overview. *Sensors* (2021).

[157] David E Haines. Direct measurement of the lethal isotherm for radiofrequency ablation of myocardial tissue. *Circulation: Arrhythmia and Electrophysiology* (2011).

[158] WC Dewey et al. Cellular responses to combinations of hyperthermia and radiation. *Radiology* (1977).

[159] Zhenpeng Qin et al. Correlated parameter fit of Arrhenius model for thermal denaturation of proteins and cells. *Annals of Biomedical Engineering* (2014).

[160] Argyrios Petras et al. A computational model of open-irrigated radiofrequency catheter ablation accounting for mechanical properties of the cardiac tissue. *International Journal for Numerical Methods in Biomedical Engineering* (2019).

[161] Andre Ribes and Christian Caremoli. Salome platform component model for numerical simulation. *31st Annual International Computer Software and Applications Conference (COMPSAC 2007)* (2007).

[162] Ana González-Suárez and Enrique Berjano. Comparative analysis of different methods of modeling the thermal effect of circulating blood flow during RF cardiac ablation. *IEEE Transactions on Biomedical Engineering* (2015).

[163] Federica Bianconi et al. Higher-order thermal modeling and computational analysis of laser ablation in anisotropic cardiac tissue. *Biomechanics and Modeling in Mechanobiology* (2025).

[164] Kuo-Chi Liu and Han-Taw Chen. Investigation for the dual phase lag behavior of bio-heat transfer. *International Journal of Thermal Sciences* (2010).

[165] Jianhua Zhou, JK Chen, and Yuwen Zhang. Dual-phase lag effects on thermal damage to biological tissues caused by laser irradiation. *Computers in Biology and Medicine* (2009).

[166] Nilamani Sahoo et al. Investigation of non-Fourier effects in bio-tissues during laser assisted photothermal therapy. *International Journal of Thermal Sciences* (2014).

[167] Robert A Kruger et al. Thermoacoustic computed tomography using a conventional linear transducer array. *Medical physics* (2003).

[168] Jakub Mesicek and Kamil Kuca. Summary of numerical analyses for therapeutic uses of laser-activated gold nanoparticles. *International Journal of Hyperthermia* (2018).

[169] Prashant K Jain et al. Calculated absorption and scattering properties of gold nanoparticles of different size, shape, and composition: applications in biological imaging and biomedicine. *The journal of physical chemistry B* (2006).

[170] Qiang Zhang et al. Facile synthesis of Ag nanocubes of 30 to 70 nm in edge length with CF3COOAg as a precursor. *Chemistry–A European Journal* (2010).

[171] Rany Rotem et al. Conjugation of gold nanoparticles with multidentate surfactants for enhanced stability and biological properties. *Journal of Materials Chemistry B* (2023).

[172] Manuel Scimeca et al. Energy Dispersive X-ray (EDX) microanalysis: A powerful tool in biomedical research and diagnosis. *European journal of histochemistry: EJH* (2018).